THE EFFECTS OF FRACTURE ORIENTATION AND ANISOTROPY ON

HYDRAULIC FRACTURE CONDUCTIVITY IN THE MARCELLUS SHALE

A Thesis

by

MARK JOHN MCGINLEY

Submitted to the Office of Graduate and Professional Studies of
Texas A&M University
in partial fulfillment of the requirements for the degree of

MASTER OF SCIENCE

Chair of Committee,	Ding Zhu
Committee Members,	A. Daniel Hill
	Judith S. Chester
Head of Department,	A. Daniel Hill

May 2015

Major Subject: Petroleum Engineering

ABSTRACT

Production of hydrocarbons from low-permeability shale reservoirs has become economically feasible thanks in part to advances in horizontal drilling and hydraulic fracturing. Together, these two techniques help to create a network of highly-permeable fractures, which act as fluid conduits from the reservoir to the wellbore. The efficacy of a fracturing treatment can best be determined through fracture conductivity analysis. Fracture conductivity is defined as the product of fracture permeability and fracture width, and describes both how much and how easily fluid can flow through fractures. It is therefore directly related to well performance.

The goal of this work is to explore fracture conductivity of Marcellus shale samples fractured in both horizontal and vertical orientations. The Marcellus shale, located primarily in Pennsylvania, Ohio, West Virginia, New York, and Maryland, is the largest gas-bearing shale formation in North America, and its development has significant implications on regional economies, the northeast United States' energy infrastructure, and the availability of petrochemical plant feedstock.

In this work, a series of experiments was conducted to determine the propped fracture conductivity of 23 different samples from Elimsport and Allenwood, Pennsylvania. Before conductivity measurements were taken, the pedigree of samples was verified through XRD analysis, elastic rock properties were measured and compared against literature values, and fracture surface contours were mapped and measured. Fracture conductivity of both horizontally and vertically-fracture samples was

determined by measuring the pressure drop of nitrogen gas through a modified API conductivity cell.

Results show that fracture conductivity varies as a function of fracture orientation only when anisotropy of the rock's mechanical properties is pronounced. It is hypothesized that the anisotropy of Young's Modulus and Poisson's Ratio play a significant role in fracture mechanics, and therefore in the width of hydraulically-induced fractures. Ultimately, the experiments conducted as part of this work show that fracture conductivity trends are strongly tied to both proppant concentration and the rock's mechanical properties.

DEDICATION

I would like to dedicate this work to my loving parents, Mark and Maggie, who have always stressed the importance of education and instilled in me all of my positive traits, and Desireé Johnson, who has unfalteringly supported me over the last two years. Joey Guillory, Matt Desrosiers, John White, and Clayton Madere also provided excellent mentorship and are exemplary for their support of my pursuit of education and their own teaching abilities.

Finally, I'd like to dedicate this work to Tony Loya and Monte King, who provided numerous and frequent examples of leadership that I will carry with me throughout my professional career.

ACKNOWLEDGEMENTS

I would like to express the sincerest gratitude to both Dr. Ding Zhu and Dr. A. Daniel Hill, who both played roles in bringing me to Texas A&M University and subsequently to their research group. From the first day, Dr. Zhu provided direction on potential research topics, approved funds for conducting important experiments that provide the basis for this thesis, permitted me to pursue external summer employment, and always had excellent insight during our weekly meetings and one-on-one discussions.

I would also like to thank Dr. Judith Chester for serving as a committee member and supporting my work. John Maldonado and the rest of the Petroleum Engineering staff also deserve high praise; the laboratories and the Richardson Building represent a safe and clean work environment, which is a lot to ask for, considering the circumstances. I'd also like to thank the Crisman Institute for Petroleum Research for providing XRD data for one of our Marcellus shale specimens.

Finally, I'd like to thank current and former Hydraulic Fracture Conductivity lab members Paola Perez, Ashley Knorr, Omar Enriquez Tenorio, Dante Guerra, Jesse Guerra, Zach Taylor, Kathryn Briggs, James Guzek, and Junjing Zhang, who have all either lent helping hands or acted as a sounding board for questions and issues encountered during my research.

NOMENCLATURE

A	Cross-sectional flow area, L^2, [ft^2]
BI	Brittleness Index, [-]
C'	Anisotropy ratio, [-]
C_a	Areal proppant concentration, ML^{-2}, [lb-m/ft^2]
c_f	Fracture conductivity, L^2L, [md-ft]
c_{f0}	Initial fracture conductivity, L^2L, [md-ft]
C_{fD}	Dimensionless fracture conductivity, [-]
d_p	Proppant diameter, L, [mm]
E	Young's Modulus, $ML^{-1}t^{-2}$, [MMpsi]
E^*	Plane Strain Modulus, $ML^{-1}t^{-2}$, [MMpsi]
G	Energy Release Rate, MLt^{-1}, [N/m]
g	Acceleration due to gravity, Lt^{-2}, [ft/s^2]
h_f	Sample width, L, [ft]
K	Stress intensity factor, $L^{1.5}M^{-1}t^{-2}$, [psi-ft$^{0.5}$]
K'	Consistency index, [-]
k	Permeability, L^2, [md]
k_f	Fracture permeability, L^2, [md]
k_m	Matrix permeability, L^2, [md]
L	Length of the sample, L, [ft]
M_g	Molecular mass, $MM^{-1}N^{-1}$, [kg/kg mol]

m_p	Proppant mass, M, [g]
n	Number of data points, [-]
n'	Flow behavior index, [-]
p_1	Inlet pressure, $ML^{-1}t^{-2}$, [psig]
p_2	Outlet pressure, $ML^{-1}t^{-2}$, [psig]
p_{cell}	Cell pressure, $ML^{-1}t^{-2}$, [psig]
q	Volumetric flow rate, L^3t^{-1}, [L/min]
R	Universal gas constant, $ML^2t^{-2}N^{-1}\varphi^{-1}$, [J/mol-K]
R_{RMS}	Root-Mean-Square roughness, L, [in.]
r	Crack tip radius, L, [ft]
T	Temperature, [K]
v_∞	Terminal settling velocity, L/t, [ft/s]
W	Mass flow rate, Mt^{-1}, [kg/min]
w_d	Dynamic fracture width, L, [ft]
w_f	Fracture width, L, [ft]
v	Fluid velocity in fracture, Lt^{-1}, [m/s]
x_f	Fracture half-width, L, [ft]
y	Fracture surface height, L, [in]
Z	Gas compressibility factor, [-]

Greek

γ_p	Proppant specific gravity, ML^{-3}, [g/cm^3]

Δp	Differential pressure, $ML^{-1}t^{-2}$, [psig]
λ	Decline rate constant, [-]
μ	Fluid viscosity, $ML^{-1}T^2T$, [Pa-s]
ν	Poisson's Ratio, [-]
θ	Fracture angle, [°]
ρ_f	Fluid density, ML^3, [kg/m^3]
ρ_p	Proppant density, ML^3, [kg/m^3]
$\sigma(r, \theta)$	Crack tip stress in polar coordinates, $LM^{-1}t^{-2}$, [psi]
σ_c	Closure stress, $LM^{-1}t^{-2}$, [psi]
ϕ	Porosity, L^3L^{-3}, [-]
φ_θ^N	Universal tensor function, [-]

Subscripts

h	Horizontal
i	Iteration number
N	Fracture mode designation
v	Vertical

TABLE OF CONTENTS

LIST OF FIGURES

xii

xiii

LIST OF TABLES

1   INTRODUCTION

1.1   Background

In low-permeability formations, such as the Marcellus shale, hydraulic fracturing is used to stimulate production from an otherwise unproductive reservoir. Matrix permeability in the Marcellus shale, estimated between 1×10^{-6} and 0.01 md, is insufficient for production of hydrocarbons via conventional means (Myers, 2008). To enhance production, a stimulation method known as hydraulic fracturing is utilized.

In hydraulic fracturing, a fluid carrying proppant is pumped into the formation at pressures sufficient to fracture the formation. Proppant, usually sand or spherical ceramic particles, is used to maintain a desirable fracture width in the absence of the high-pressure fracturing fluid. After the fractures' propagation has been arrested, fracturing fluid is withdrawn from the reservoir during the flowback period. As this occurs, the formation slowly returns to its equilibrium pressure. During this process, fractures close in on proppant, and the remaining proppant acts as a barrier to fracture closure, providing sufficient fracture width for production.

The most common parameter used to describe the effectiveness of a hydraulic fracturing job is fracture conductivity. This parameter is the product of fracture width and fracture permeability; it is expressed in units of md-ft, as shown below,

$$c_f = k_f w_f \quad \text{...(1-1)}$$

Conductivity can also be expressed in a dimensionless form, which compares the fracture conductivity to the formation conductivity,

$$C_{fD} = \frac{k_f w_f}{k_m x_f} \quad \text{..(1-2)}$$

Opinions vary on best practices for hydraulic fracturing, but in general, the fracturing fluid, proppant size, proppant type, or proppant concentration can be varied independently or in combination in order to optimize fracture conductivity. Due to various economic considerations in the Marcellus shale, including the high ratio of relatively low-value dry gas to high-value condensate or oil, fracturing design usually takes a low-cost route in the form of slickwater fluid and natural white sand proppant.

Typically, fracture conductivity of shale is measured in a laboratory setting using either outcrop or core samples from the desired formation. A rough fracture is initiated parallel to the bedding planes of the formation and then split in tension, simulating a horizontal fracture. By measuring the pressure drop of a fluid passing through the fracture face under sealed conditions, fracture conductivity can be estimated. However, this fracture conductivity measures the conductivity of a horizontal fracture, rather than that of a vertical fracture.

In the Marcellus shale, the productive interval is located between 4,000 and 8,500 feet of total vertical depth (TVD), where fractures most commonly propagate vertically due to the high overburden stress at these depths (Shelley et al., 2014). In formations exhibiting significant mechanical property anisotropy, it is conceivable that the horizontal and vertical fracture conductivities are significantly different (Chen et al., 1996). The goal of this research is to investigate the differences of horizontal and vertical fracture conductivity, particularly in the Marcellus shale, so that better estimates of field conditions can be made based on laboratory studies in order to avoid costly mistakes. A schematic of horizontal and vertical fractures is shown in Fig. 1.1. Previous

research has indicated a strong correlation between the absolute values of rock

mechanical properties and conductivity (Jansen, 2014); this will also be investigated as it

pertains to Marcellus shale specimens.
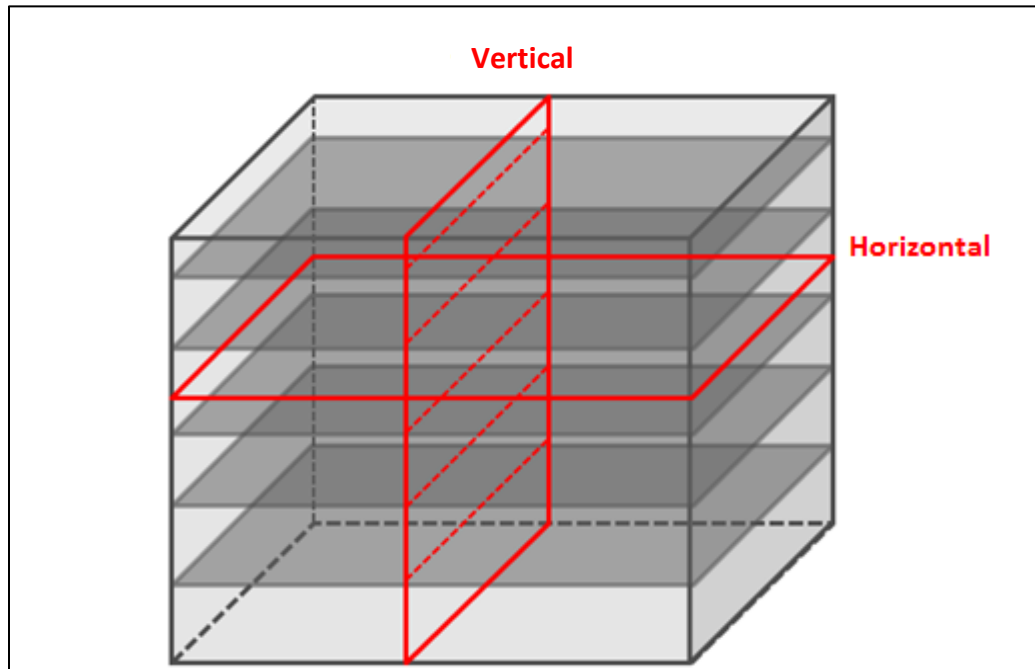
Fig. 1.1 – Diagram of Horizontal and Vertical Fracture Types

1.2   Literature Review

1.2.1   Marcellus Shale Overview

The Marcellus shale is a primarily gas-bearing organic black shale formation that

covers large swaths of Pennsylvania and extends into New York, Ohio, West Virginia,

Virginia, and Maryland. Bearing up to 410 trillion cubic feet of proven gas reserves, it is

posited to be the largest shale-gas formation in North America (Shelley et al., 2014).

3

Successfully extracting gas from the Marcellus shale has enormous implications on regional economies, the northeast United States' energy infrastructure, and the availability of petrochemical plant feedstock. Due to highly repeatable and efficient drilling and completions methods, the Marcellus shale also exhibits the lowest breakeven price when compared to other North American shale plays, at a natural gas price of $3.17 per thousand cubic feet (Schweitzer and Bilgesu, 2009).

As the isopach map in Fig. 1.2 shows, the thickest sections of the Marcellus are located in northeastern Pennsylvania and at the juncture of Pennsylvania, West Virginia, and Maryland. As shown in Fig. 1.3, gas production increased exponentially in the Marcellus region from 2007 to 2015.
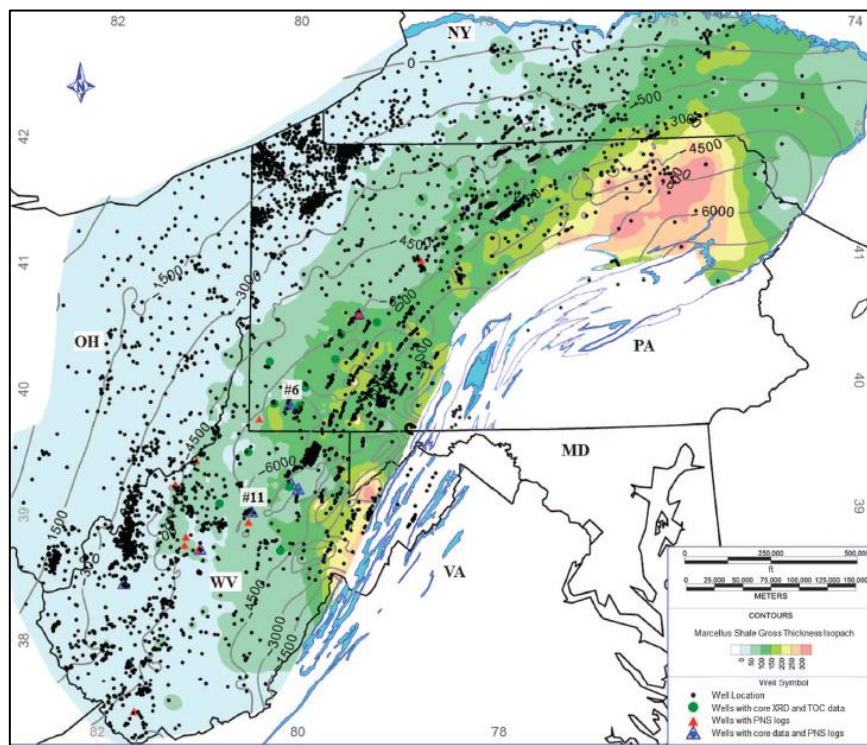
Fig. 1.2 – Marcellus Shale Isopach Map with Well Locations (Wang and Carr, 2013)
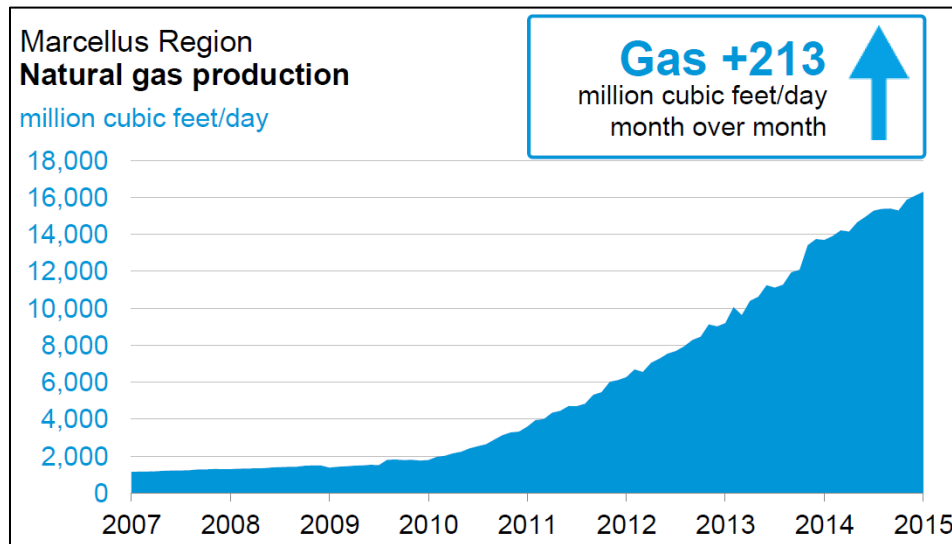
Fig. 1.3 – Natural Gas Production from the Marcellus Shale (U.S. Energy Information Administration, 2014)

Ongoing volatility of hydrocarbon commodity prices is added incentive to improve the evaluation of fracture conductivity prior to drilling, as it could significantly reduce drilling costs and improve the profitability of drilling in this region.

Two sets of natural joints trending northeast and southwest characterize the fissile, Devonian-age Marcellus shale. The so-called J1 and J2 joint sets, caused by the pressurization of organic matter during its thermal maturation and burial, can be exploited to enhance production in horizontal wells. Fig. 1.4 below shows the presence of these faults in the Marcellus shale. Most commonly, the plane of least principal stress is roughly perpendicular to the J1 joint set. Coincidentally, the J1 joints are also more closely spaced than the J2 joints, meaning that the combined matrix and fracture

permeability is greater in the J1 direction (Engelder et al., 2009). Drilling wells that

orthogonally intersect one of the joint sets is common practice, as it increases the well's

exposure to natural fractures and also ensures that the well is oriented perpendicular to

the plane of least principle stress (Engelder et al., 2009). When undergoing a hydraulic

fracture treatment, the rock fractures perpendicular to the plane of least principle stress,

resulting in fractures that propagate directly away from the wellbore.
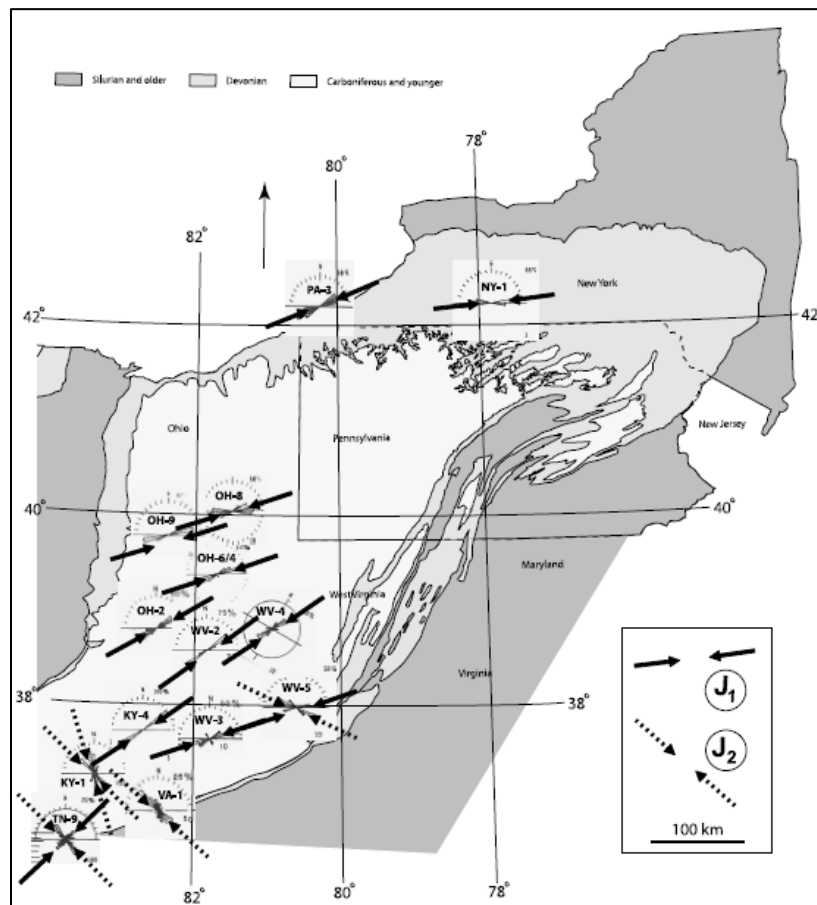
Fig. 1.4 – Rose Plot Showing J1 and J2 Joint Orientation (Engelder et al., 2009)

6

Like most black shales, the Marcellus has long been widely considered to be the source for an overlying conventional reservoir, but unlikely to be a productive interval in and of itself. A stratigraphic column of the Marcellus shale and surrounding formations is shown in Fig. 1.5. Wells drilled into the underlying conventional reservoir, the Oriskany sandstone, frequently experienced blowouts during its development in the mid-20th century. The natural faults of the Marcellus shale are now thought to have contributed to these gas blowouts. Both the faultless nature of the Oriskany sandstone and the low matrix permeability of the Marcellus support the idea that a network of natural fractures in the Marcellus shale contributed significantly to the presence of free, high-pressure gas in the Marcellus interval (Engelder et al., 2009).

The Middle Devonian Appalachian Basin sequence of shale and limestone represents, "the initiation of the Devonian-Mississippian anoxic event in the central Appalachian basin" (Boyce and Carr, 2009). During its deposition roughly 385 million years ago, the Appalachian Basin was a marine environment surrounded by the Cincinnati Arch to its west, the Rheic Ocean to the south, and the Acadian Mountains to the east. Fig. 1.6 shows the current Marcellus shale region outlined in red, as well as the paleogeographic features described above. Based on total organic content and gamma ray values, the Middle Devonian units appear to have been deposited in environments with varying availability of oxygen. The Marcellus and Harrell shales, for example, exhibit extremely high gamma ray values and are therefore likely to have been deposited in an anoxic environment, where bacteria that consume organic material could not survive. Units such as the Mahantango, which has a characteristic gamma ray signature

lower than that of the Marcellus, was likely deposited in a suboxic environment. Units such as the Tully and Onondaga limestone, which are devoid of significant gamma ray signatures, are thought to have been laid down in an environment with sufficient oxygen for decomposition of organic material by bacteria (Boyce and Carr, 2009).

Devonian	Upper	Gordon
		Alexander
		Huron
		Rhinestreet Shale
		Harrell Shale
	Middle	Tully Limestone
		Mahantango Shale
		Marcellus Shale
		Onondaga Limestone
		Huntersville Chert
		Needmore Shale
		Oriskany Sandstone

Fig. 1.5 – Stratigraphic Column of the Appalachian Basin, Including Marcellus Shale
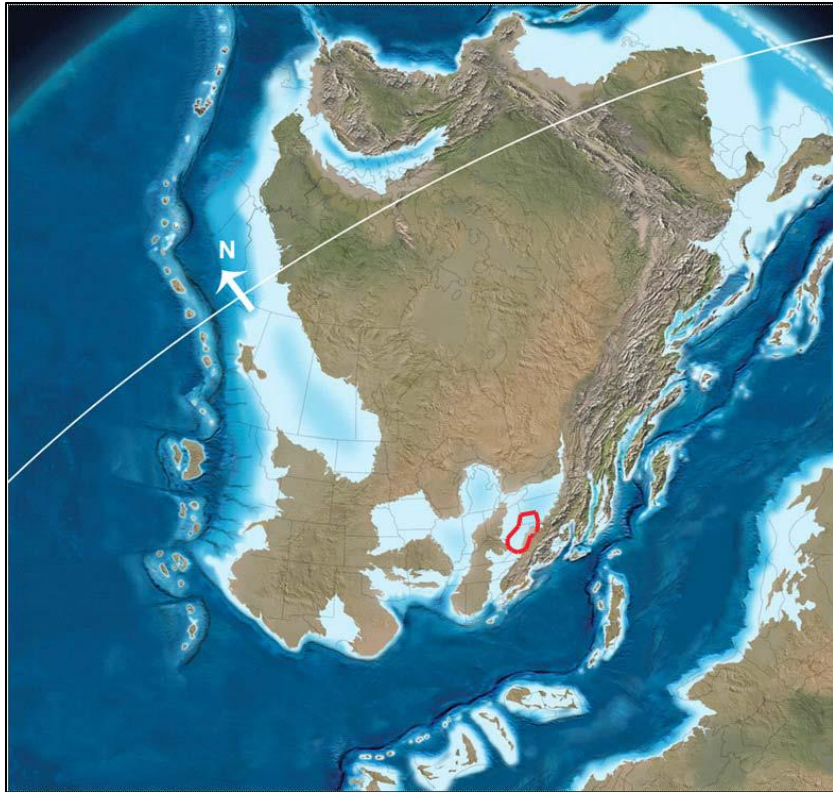
Fig. 1.6 – The Area of Interest at the Time of Deposition, 385 Million Years Ago (Boyce and Carr, 2009)

The Marcellus shale is identified in cores as possessing a volumetric concentration of quartz up to 70% and a clay content of roughly 25%. The total thickness of the Marcellus ranges from 50-200 feet and total organic content ranges from 3-12% (Shelley et al., 2008). For Boyce and Carr's study, 36 cores underwent x-ray diffraction (XRD) to determine mineralogy. Those results are summarized in Fig. 1.7.
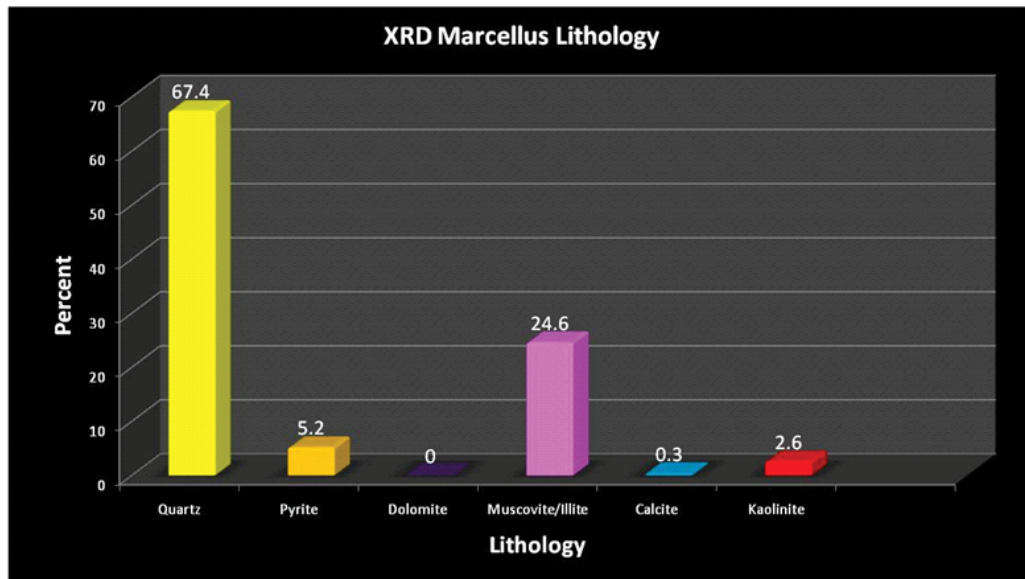
Fig. 1. 7 – Mineralogy of Marcellus Shale in Southwestern Pennsylvania (Boyce and Carr, 2009)

Total organic content is important because it is usually strongly correlated to the gas saturation in unconventional source rocks (Passey et al., 2010), as demonstrated in Fig. 1.8. The results in Fig. 1.8 show the correlation between total organic content and gas saturation values for dozens of shale-gas formations worldwide.
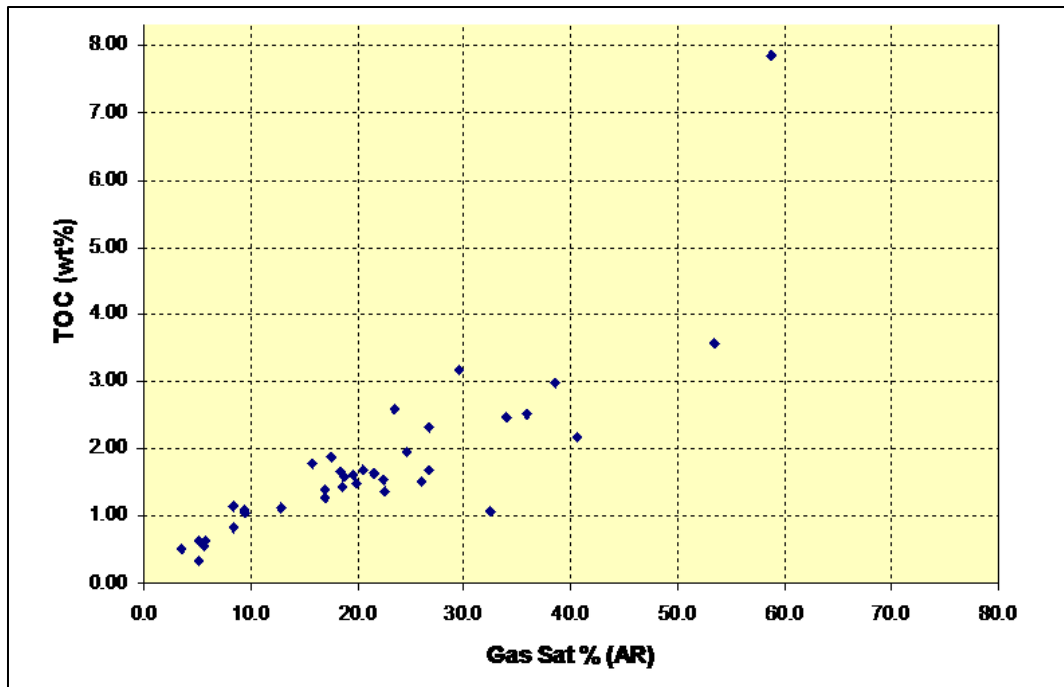
Fig. 1.8 – Total Organic Content vs. Gas Saturation (Passey et al., 2010)

1.2.2 Hydraulic Fracturing in North American Shale Formations

In 1947, the first successful hydraulic fracturing treatment was executed in the Hugoton gas field in Kansas by Stanolind Oil. In this first experiment, natural river sand was carried into the formation using napalm (in great surplus in the post-World War II environment) as the fracturing fluid. After injecting this mixture, the napalm gel was broken down using a gel-breaker solution and the well was put online. In this first study comprising several wells, returns were increased by up to 1,000% as compared to pre-fractured rates (Clark, 1949). In the years since this first well was "frac-ed", engineers and researchers have sought to improve the process in many ways including the use of foams, microseismic data, manufactured proppant, and boutique fracturing fluids.

11

There are a number of operators in the Marcellus shale, and the variety of operational philosophies and its 90,000 square mile expanse makes it difficult to typify one stereotypical wellbore and fracture treatment design (Mayerhofer et al., 2011). Wells in the Marcellus are commonly completed at a depth between 4,000-8,000 feet TVD, with laterals ranging from 2,000-7,000 feet in length. Due largely to environmental concerns, relatively few wells in the Marcellus are drilled using oil-based muds as compared to other unconventional plays such as the Haynesville shale. In 225 analyzed horizontal wells in the Marcellus, 36% used water-based muds, and the other 64% used synthetic-based mud (Guo et al., 2012).

Since the Marcellus produces almost exclusively dry gas and condensate, fracture conductivity is not as critical in this formation as in those bearing high-viscosity fluids. Low-cost drilling, completion, and production methods are popular in the Marcellus as a result of the prevalence of low-viscosity gas and its lower relative value. Natural white sand is the most common proppant utilized in fracture treatments, with 40/70 mesh sand being the most common variety. Fracture treatment designs are always changing, but approximately 40% of the sand used in horizontal Marcellus wells is 40/70 mesh sand, with the balance being 80/100 and 20/40 mesh sand (Houston et al., 2009; Mayerhofer et al., 2011; Shelley et al. 2014). Water with a small amount of friction reducer, known as slickwater, is the most common fracturing fluid (Shelley et al., 2014). In wells analyzed by Mayerhofer et al. (2011), seven fracture stages were used, and each fracture stage used five perforation clusters spaced two feet in length each over a span of 200 feet per

stage. Table 1.1 summarizes production information for the Marcellus and other prominent North American shale plays.

Table 1.1 – Summary of North American Shale Play Properties (Zhang, 2014)

Properties	Marcellus	Eagle Ford	Fayetteville	Barnett
True Vertical Depth (ft)	4,000-8,000	5,000-14,000	1,500-6,500	6,000-8,500
Closure stress gradient (psi/ft)	0.67-0.76	0.7-0.95	0.59-0.7	0.61-0.73
Effective closure stress (psi/ft)	2,500-6,000	2,000-8,000	1,000-5,000	3,000-5,500
Dominant hydrocarbon	Gas, condensate	Oil, condensate	Gas	Gas
Fracture Design	Water frac, foam	Gelled frac, hybrid, high-way	Water frac	Water frac
Proppant size (mesh)	100, 40/70, 30/50	40/70, 30/50, 20/40	100,30/70	100, 40/70, 30/50
Maximum proppant concentration (ppg)	2.5	4	2	3.5
Average concentration (ppg)	1.2	1.2	0.6	0.6

It is important to note here that fracture treatments are not static. Proppant sizes, fluid composition, and proppant concentration are all traditionally changed throughout the fracturing process. Initially, a small proppant size, such as 100 mesh, is used to prop

open the fracture tip, which exhibits the smallest fracture aperture. In addition to being able to reach the fracture tips, smaller proppant has several other benefits over large proppant. It is more readily suspended in a colloid as a result of its larger surface-area-to-volume ratio, and is therefore more likely to provide even coverage throughout the vertical extent of the fracture. Slickwater fluids are particularly susceptible to proppant settling, with Boyer et al. (2014) showing that at 5,000 psi, only 8.3% of 40/70 mesh natural white sand was suspended above the proppant settling line. Settling of 40/70 mesh proppant from this study is shown in Fig. 1.9. Terminal settling velocity, v_∞, derived by Brannon and Pearson (2007) is dependent on proppant diameter and given by,

$$v_\infty = \left[\frac{(\rho_p - \rho_f)g d_p^{n'+1}}{3^{n'-1}18K'}\right]^{1/n'} \dots\dots\dots\dots\dots\dots\dots\dots\dots\dots\dots\dots\dots\dots\dots\dots\dots(1\text{-}3)$$

Fig. 1.9 – Settling of 40/70 Mesh Sand in Slick Water (Boyer et al., 2014)

The distribution of proppant within the fracture is also dependent on fracture geometry and the composition of the fracturing fluid. A graphical representation of proppant settling within a fracture is shown in Fig. 1.10. In order for proppant to reach a particular region of the fracture, its entire flow path must have an aperture greater than the proppant diameter. As a result, a continuous fracture may exhibit regions with no proppant, or a partial monolayer, full monolayer, or multiple layers of proppant.
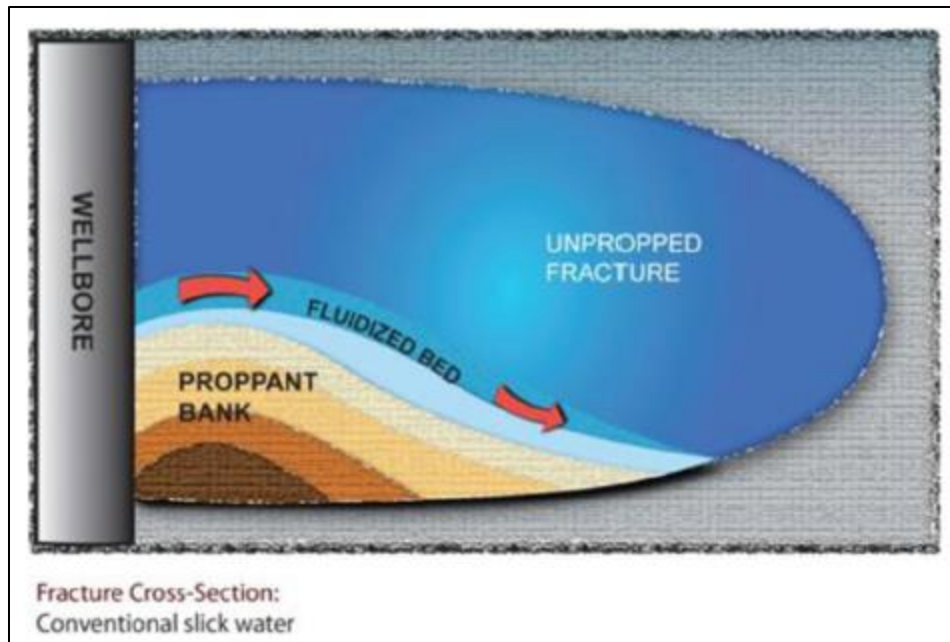
Fig. 1.10 – Representation of Proppant Settling in Hydraulic Fracture (Boyer et al., 2014)

The final advantage for small proppant is that it is less susceptible to screen-out. Screen-out refers to the condition wherein pumping pressure exceeds the pumping equipment's maximum allowable working pressure as a result of the proppant pack blocking the fracture flow path. This condition has three primary causes: large proppant that becomes wedged in the fracture, fracturing fluid leak-off, and high proppant concentration. Once screen-out has been detected, fracturing at that stage must cease, so delaying screen-out as long as possible is desirable. Operators and field service providers typically work together to determine an appropriate pumping pressure, as well as the schedule for increasing proppant size and proppant concentration so as to create

the most extensive fracture network and avoid premature screen-out. A simplified

fracture treatment for one stage in the Marcellus may look like that shown in Table 1.2.

Table 1.2 – Simplified Fracture Treatment Schedule for Marcellus Shale

Stage	Fluid Volume (gal)	Proppant Concentration (ppg)	Proppant Size
Pad	8,000	0	-
1	4,000	0.5	100% 100 mesh
2	4,000	1.0	50% 100 mesh, 50% 40/70 mesh
3	4,000	1.5	100% 40/70 mesh
4	3,000	2.0	50% 40/70 mesh, 50% 30/50 mesh
5	1,500	2.5	100% 30/50 mesh
Flush	6,000	0	-

Since the aperture of a fracture typically decreases as the distance to the wellbore

increases, larger proppant is typically called for in the final stages of a fracturing

treatment in order to maximize fracture width.

1.2.3 Fracture Conductivity Test Method and Calculation

The standard long-term conductivity test method for determining proppant pack conductivity is outlined by ISO 13503-5:2006. This method, traditionally used to evaluate the conductivity of proppant, calls for the use of smooth saw-cut Ohio sandstone and a 2% KCl solution. Conductivity is measured at various pressures, all of which must be maintained for 50 hours during conductivity measurement. These tests are extremely time-consuming and resource-intense. The test is designed to eliminate as many variables as possible in order to provide fair comparisons of proppant. The 2% KCl solution used as the stand-in for fracturing fluid also causes irreversible damage to the sample and proppant, rendering each sample usable only once. This test is essentially a modified version of the API's own short-term conductivity test, API RP-61. Fig. 1.11 shows that the ISO standard's test procedure can result in up to an 85% reduction in conductivity measurements from API RP-61.
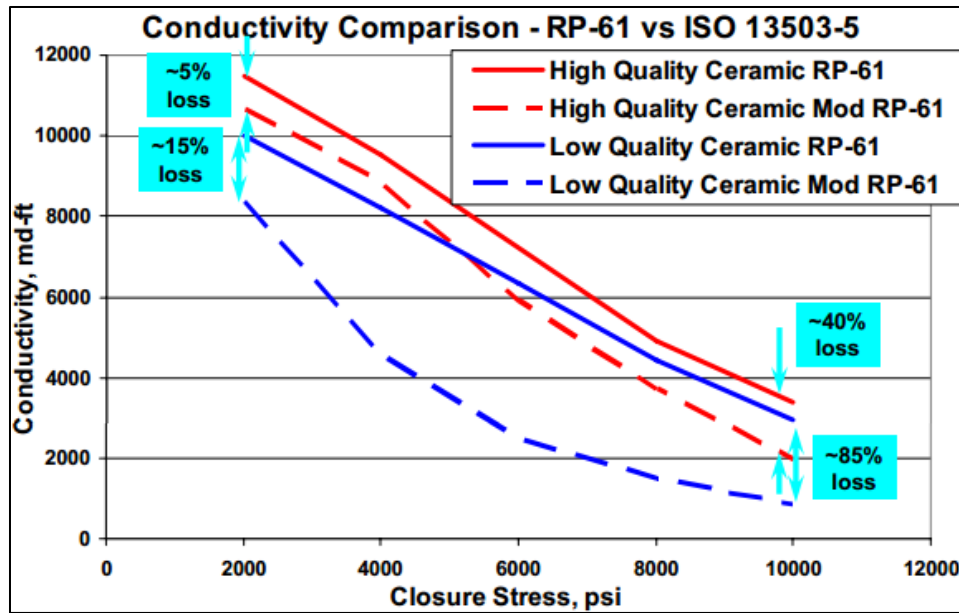
Fig. 1.11 – Comparison of API RP-61 and ISO 15303 (Mod RP-61) (Palisch et al., 2007)

Since these standards are not intended to provide an accurate representation of fracture conductivity and are both extremely time-consuming and expensive to run, determination of fracture conductivity for this work was executed via alternate means. First, in order to maintain sample integrity for multiple tests, the 2% KCl solution was replaced with dry nitrogen gas, which is inert in the testing environment (Zhang et al., 2014). Second, since the goal of these tests is to evaluate fracture conductivity, the Ohio sandstone was replaced with Marcellus shale samples, which were obtained from two different outcrop locations. The overall sample dimensions are consistent with API sample dimensions as shown in Fig. 1.12.
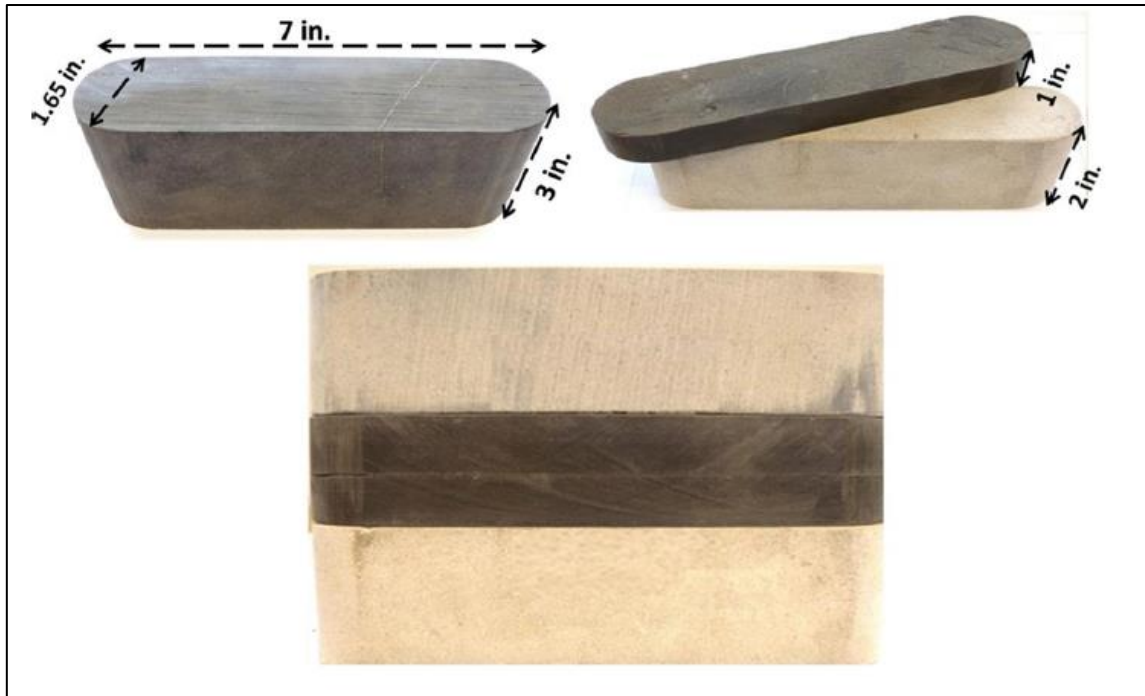
Fig. 1.12 – Sample Configuration and Dimensions (Kamenov, 2013)

To simplify the experimental procedure, proppant was manually placed on the fracture face and then inserted into the modified conductivity cell. Dynamic proppant placement has been implemented by others (Awoleke et al., 2012; Zhang et al., 2014) in order to more realistically simulate proppant transport from the wellbore to the fracture. In this setup, a proppant and fracturing fluid slurry is pumped into the fracture using positive displacement pumps. Once the pumps are shut down, the proppant remains in the fracture, and nitrogen gas is passed through the fracture to simulate the onset of production.

Several methods for calculation of propped fracture conductivity have been proposed. Darin and Huitt (1960) used laboratory measurements to demonstrate that a

modified version of the Kozeny-Carman relationship could be used to describe fluid flow through a proppant partial monolayer. They also showed that a proppant partial monolayer can exhibit higher conductivity (sometimes by an order of magnitude) than multiple layers of the same proppant. More recent proposals for calculation of propped fracture conductivity include those by Gao et al. (2012), who suggest that modeling the effects of proppant embedment, deformation, elasticity, and size can improve analysis of either monolayer or multilayer conductivity analysis.

1.2.4 Rock Fracture Mechanics

Of critical importance to this research is to understand how rocks fracture in realistic downhole scenarios. There are three modes of fracture opening. A Mode I fracture is an opening fracture induced by a tensile stress. A Mode II fracture is a sliding fracture, induced by a shear stress that acts in the direction parallel to the fracture. A Mode III fracture is a tearing fracture, which is induced by a shear stress perpendicular to the plane of the fracture. Fig. 1.13 is a schematic of all three fracture modes.

.
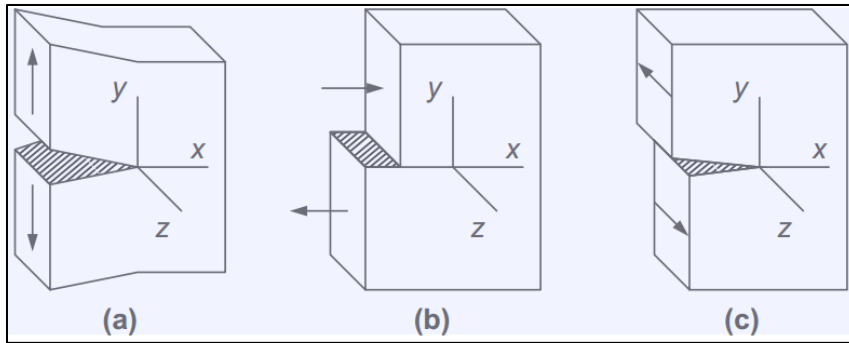
Fig. 1.13 – Schematic of Basic Fracture Modes: (a) Mode I, (b) Mode II, (c) Mode III
(Sun and Jin, 2012)

The stress at the tip of an ideal fracture can be described as,

$$\sigma(r,\theta) = \frac{K_N \Phi_\theta^N}{\sqrt{r}} \quad\text{..(1-4)}$$

where K_N is the stress intensity factor for one of the three fracture modes. The stress

intensity factor, K_N, is a term that can be determined numerically, analytically, or

experimentally. However, as demonstrated by Shylapobersky and Chudnovsky (1992),

hydraulic fractures rarely display the same net fracture pressure as would be predicted by

Equation 1-4.

The propagation of fractures is also of great interest for this work. Hydraulic

fractures are usually thought of as planar, bi-wing, and vertically-oriented, which can be

a gross oversimplification. Seminal work by Cinco-Ley and Samaniego (1981) that

assumed the predominance of simple, planar fractures also showed that dimensionless

fracture conductivity has an optimal value beyond which additional returns are minimal.

Diagnostic tools such as microseismic analysis show that multi-stranded fractures are

found in many different formation types, including shale (Dahi-Taleghani and Olson,

2009). Fisher et al. (2004) arrived at a similar conclusion via microseismic data from the

Barnett shale, and their findings are shown in Fig. 1.14.
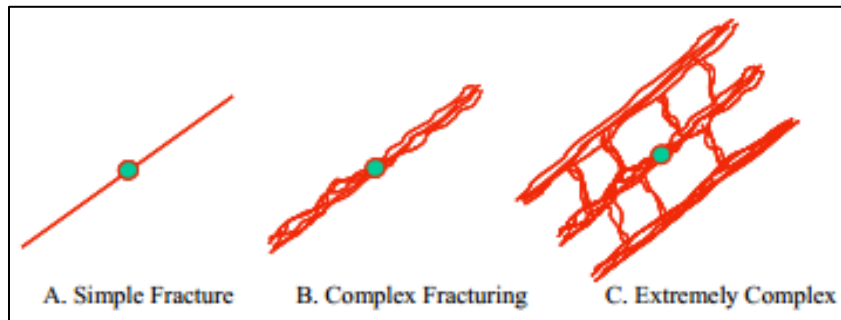
Fig. 1. 14 – Various Levels of Fracture Complexity (Fisher et al., 2004)

The presence of natural fractures can also lead to increased fracture complexity. As a

hydraulic fracture propagates through the formation, it can encounter existing natural

fractures, microcracks from previous hydraulic fracturing stages, or otherwise weakened

zones (thin beds of weaker rock, depositional discontinuities, etc.). When dealing with a

formation with natural fractures such as the Marcellus shale, there are three possible

scenarios for interaction of hydraulic and natural fractures, as depicted in Fig. 1.15. In

(a), the hydraulic fracture bypasses the natural fracture. In (b), the hydraulic fracture is

re-routed exclusively into the natural fracture, and in (c), the hydraulic fracture crosses

the natural fracture and crack tips propagate in both the natural fracture and the

hydraulic fracture.
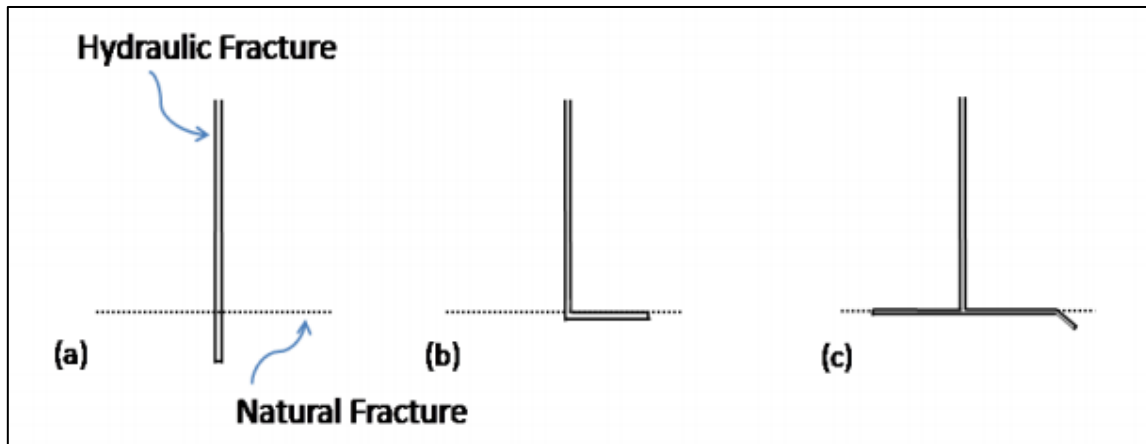
Fig. 1.15 – Interaction between Hydraulic and Natural Fractures (Dahi-Taleghani and Olson, 2009)

The idea that fractures frequently diverge from a linear path is also verifiable in the larger context of the whole formation. Frequently sandwiching faults are damage zones, which greatly add to the overall fracture network. Damage zones are highly fractured; these zones are the result of a highly-stressed fault leading to fractures outside of the original fault plane. Additionally, these damage zones often have much higher permeability than the fault core itself (Johri, 2012). The damage zones around a fault, typically the adjacent 60-100 meters to either side, are much greater in size than the fault core itself, which is usually less than 50 centimeters wide. A diagram of a fault and its associated damage zone is shown in Fig. 1.16.
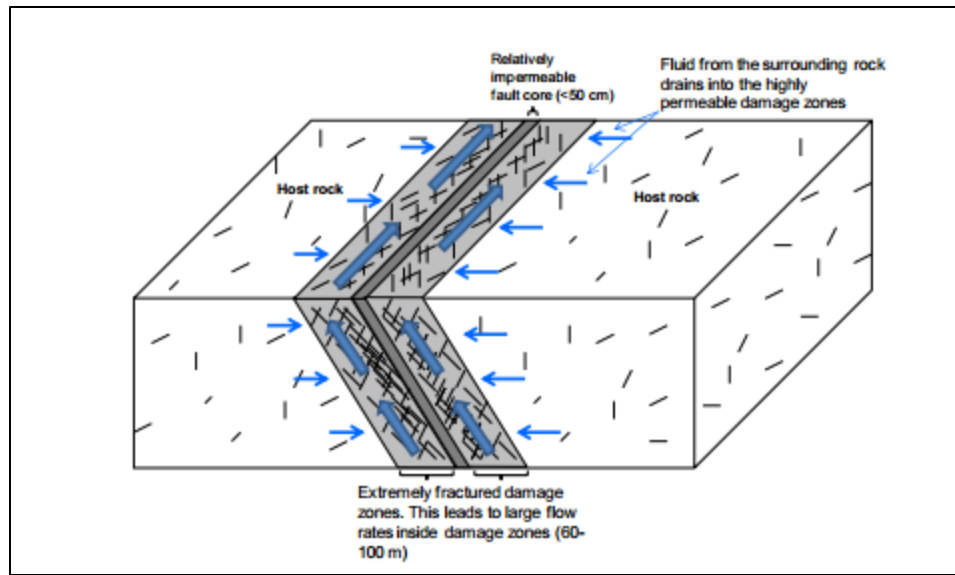
Fig. 1.16 – Schematic of a Fault Zone (Johri, 2012)

Although complex fractures do not always result in a larger stimulated rock volume than a planar, bi-wing fracture, fractures that take advantage of natural weaknesses in the rock will experience a lower fracturing fluid pressure drop and allow the fracturing fluid to propagate further into the formation, so it stands to reason that complex fractures generally result in a larger stimulated rock volume. The importance of maximizing stimulated rock volume is shown in Fig 1.17, which shows that a threefold increase in stimulated rock volume results in three times greater production over a fifteen-year well life.

25
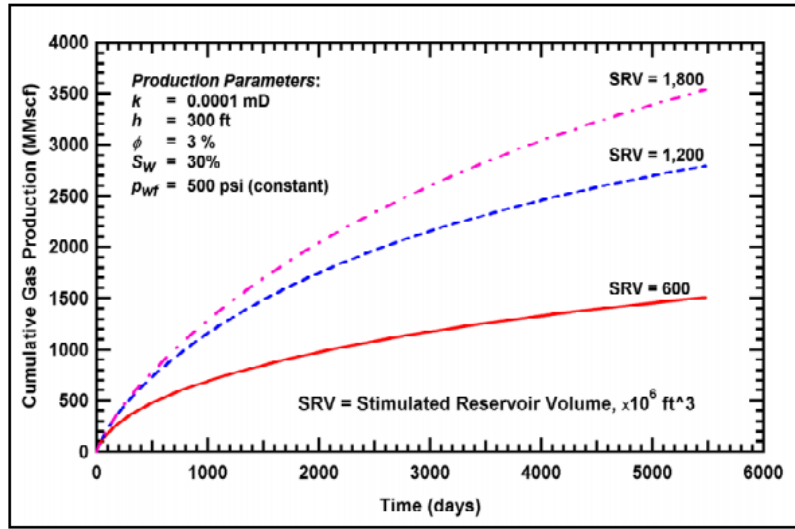
Fig. 1.17 – Impact of Stimulated Rock Volume on Cumulative Gas Production
(Mayerhofer et al., 2006)

The direction of crack propagation in a fracture is a function of the crack's

energy release rate, G,

$$G = \frac{(K_I^2 + K_{II}^2)}{E^*}$$ ....(1-5)

where E* can be described as,

$$E^* = \frac{E}{(1-\nu^2)}$$ ....(1-6)

and K_I and K_{II} are the stress intensity factors for Mode I and Mode II fractures.

If G is greater than the critical energy release rate, G_c, then the crack will propagate

critically. The crack propagates in the direction that yields the highest energy release

rate, and in anisotropic rock, this may result in a highly complex fracture that exhibits

higher fracture conductivity than a planar fracture. Herein lies the importance of

understanding which rocks have homogeneous structures and which ones have structures

26

that result in anisotropic elastic rock properties. Cracks can also grow in a sub-critical state ($G < G_c$), but for this to occur, the host material must be weakened, generally via chemical means (Dahi-Taleghani and Olson, 2009). The maximum energy release rate can be expressed as,

$$G_{max} = \frac{\bar{K}_I^2}{E^*} + \frac{\bar{K}_{II}^2}{E^*} \quad \text{..(1-7)}$$

Where,

$$\bar{K}_I = \frac{1}{2}\cos\left(\frac{\theta_0}{2}\right)[K_I(1 + \cos\theta_0) - 3K_{II}\sin\theta_0] \quad \text{.............................(1-8)}$$

And,

$$\bar{K}_{II} = \frac{1}{2}\cos\left(\frac{\theta_0}{2}\right)[K_I\sin\theta_0 + K_{II}(3\cos\theta_0 - 1)] \quad \text{.............................(1-9)}$$

In these expressions, $\theta_0 = 0$ describes a state where the fracture propagates in a straight direction, as expected in Mode I fracturing, and $\bar{K}$ is the energy release rate in a particular orientation.

1.3   Problem Description, Objectives, and Significance

Fracture conductivity in horizontally-drilled, hydraulically-fractured wells is of great importance. As shown in Fig. 1.18, a small change in fracture conductivity greatly impacts a well's cumulative production.
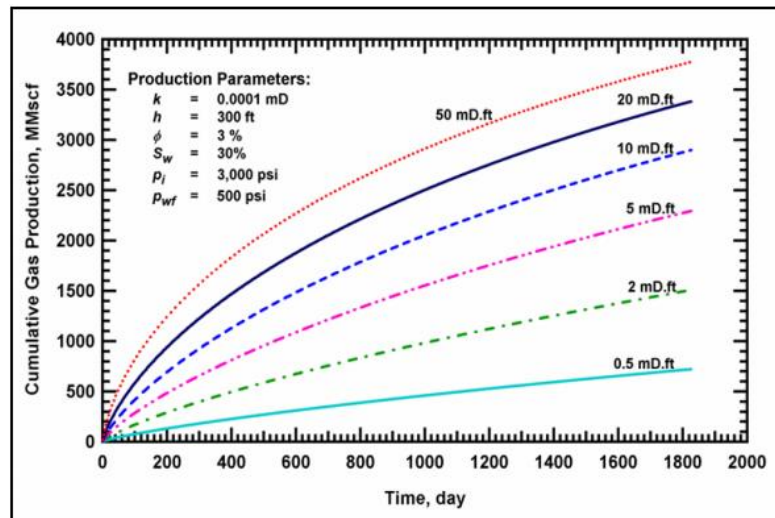
Fig. 1.18 – Impact of Fracture Conductivity on Cumulative Gas Production over Time
(Mayerhofer et al., 2006)

For the above figure, each curve represents a reservoir with the same stimulated rock volume, so production increases are due solely to the increased fracture conductivity. An increase from 0.5 md-ft to 5 md-ft results in a four-fold increase in production over the displayed five years, and increasing conductivity to 50 md-ft improves production by more than a factor of seven.

Many previous studies have established that fracture conductivity is a parameter with significant leverage on cumulative production. Some of these studies have focused on sandstone reservoirs, determining conductivity of proppant packs, or have used concentrations of proppant that are not realistic for shale formations. The work here focuses on determining fracture conductivity at reasonable proppant concentrations for the Marcellus shale, which has not been extensively studied.

28

The disparity in fracture conductivity between horizontal and vertical fractures is also poorly understood. This gap in knowledge applies to all formations, the Marcellus shale included. Rock properties that may depend on orientation, such as Young's Modulus and Poisson's Ratio, are known to impact fracture characteristics. It is conceivable that the anisotropy of rock properties would be manifested as differences between horizontal and vertical fracture conductivity.

The objective of this work is to quantify how differences in rock properties impact fracture conductivity, if at all. Typically, conductivity testing for fractures utilizes samples with horizontal fractures. However, the depths at which most North American shale plays are being completed would suggest that the bulk of hydraulic fracturing results in vertical fractures. Therefore, this work presents a comparison of horizontal and vertical fracture conductivity.

1.4   Approach

Procedures for the experimental approach to this work are detailed below:

(1) Collect Marcellus shale samples from two sites in central Pennsylvania.

(2) Ascertain the samples' mineralogy using X-Ray Diffraction, and compare these results with the mineralogy of other known Marcellus samples. This verifies the pedigree of the rock and ensures that the conductivity test results are representative of what might be seen in a typical Marcellus well.

(3) Divide the samples into two groups: those to be fractured horizontally, and those to be fractured vertically. Horizontal fractures are commonly used for

29

laboratory testing for several reasons. First, fracturing shale samples parallel to the bedding planes is significantly easier than fracturing through multiple bedding planes. Secondly, horizontally-fractured samples are far less likely to fail during the fracturing process, saving both time and resources. Finally, the Cooke conductivity cell used for conductivity experiments is a device that requires communication between the fracture and a small pressure port, so a vertical fracture, which is generally much rougher, may not align with the pressure port, thereby rendering a viable experiment impossible. The current industry standard is to test horizontal fracture conductivity, so the results of horizontal fracture conductivity tests are comparable to those conducted by operators. Despite the difficulty of inducing a vertically-oriented fracture in Marcellus shale samples, vertical fractures are the prevailing fracture orientation in this and most other North American shale formations.

(4) Determine Poisson's Ratio and Young's Modulus for both sets of samples in both the horizontal and vertical orientation

(5) Scan fracture surfaces using a laser profilometer to determine fracture root-mean-square roughness. This step is to be repeated after each conductivity test in order to obtain information about deformation of the fracture after testing.

(6) Run conductivity tests using 40/70 white mesh sand proppant at concentrations representing 0.16 pounds of proppant per gallon of fluid (ppg), 0.33 ppg, 0.65 ppg, and 1.3 ppg.

(7) Compare and contrast results of horizontally- and vertically-fractured samples.

The flowchart in Fig. 1.19 demonstrates the experimental workflow described above.

```
┌──────────────────────────────────────────────┐
│                Collect Samples                 │
└──────────────────────────────────────────────┘
                        ↓
┌──────────────────────────────────────────────┐
│               Verify Mineralogy                │
└──────────────────────────────────────────────┘
                        ↓
┌──────────────────────────────────────────────┐
│           Test Elastic Rock Properties         │
└──────────────────────────────────────────────┘
                        ↓
┌──────────────────────────────────────────────┐
│      Fracture Rocks (Horizontally or Vertically) │
└──────────────────────────────────────────────┘
                        ↓
┌──────────────────────────────────────────────┐
│             Scan Fracture Surfaces             │
└──────────────────────────────────────────────┘
                        ↓
┌──────────────────────────────────────────────┐
│           Test Fracture Conductivity           │
└──────────────────────────────────────────────┘
                        ↓
┌──────────────────────────────────────────────┐
│                Analyze Results                 │
└──────────────────────────────────────────────┘
```
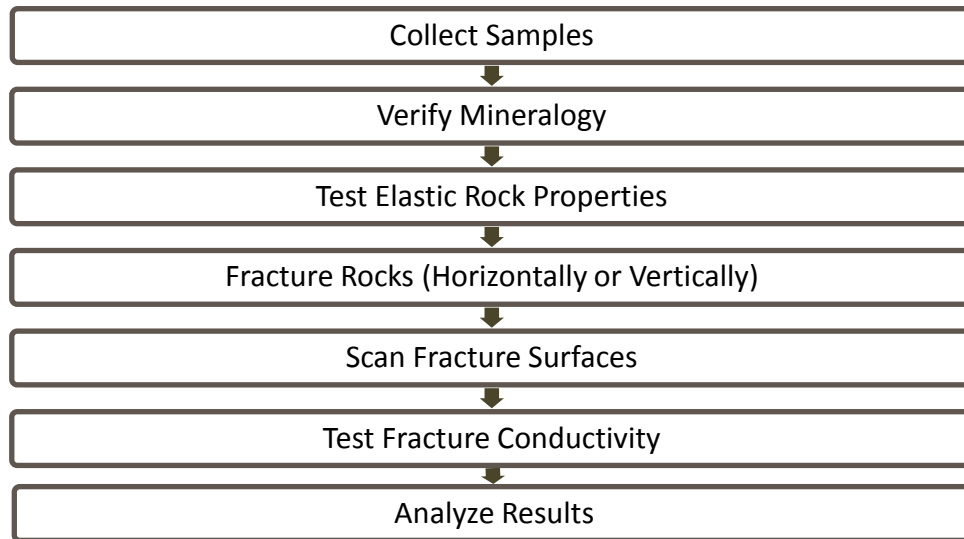
Fig. 1.19 – Workflow for Experimental Work

2 EXPERIMENTAL DESIGN AND METHODOLOGY

2.1 Introduction

Conductivity experiments have traditionally aimed to benchmark the quality of a particular proppant or to illuminate the economic potential of exploration acreage. Fracture conductivity results can be further used to history match data from analogous wells or to predict a well's future performance.

The goal for both of these types of tests is to produce reproducible and realistic results. Appropriate equipment calibration schedules, strict adherence to procedures, and reusing samples whenever possible helps to ensure that results are reproducible. Realistic results can be obtained by matching reservoir conditions such as closure stress, fracture orientation, fracture mode, and operating conditions such as proppant type and concentration. The latter requires that the sample be a close facsimile of the reservoir in its downhole state.

This chapter describes the selection of materials, preparation of equipment and samples, and provides procedures for all of the work undertaken. Means of limiting errors and troubleshooting are also described herein.

2.2 Shale Samples, Fluids, and Proppant

Shale samples for this research were obtained from two outcrop locations shown in Fig. 2.1. The Elimsport location was previously used by a leaseholder in the Marcellus to excavate shale samples for large-block triaxial fracture testing. The material surrounding the original large block test samples had also been excavated and

deposited in large debris piles. These piles provided plenty of rocks from which 13

suitable conductivity samples were obtained.
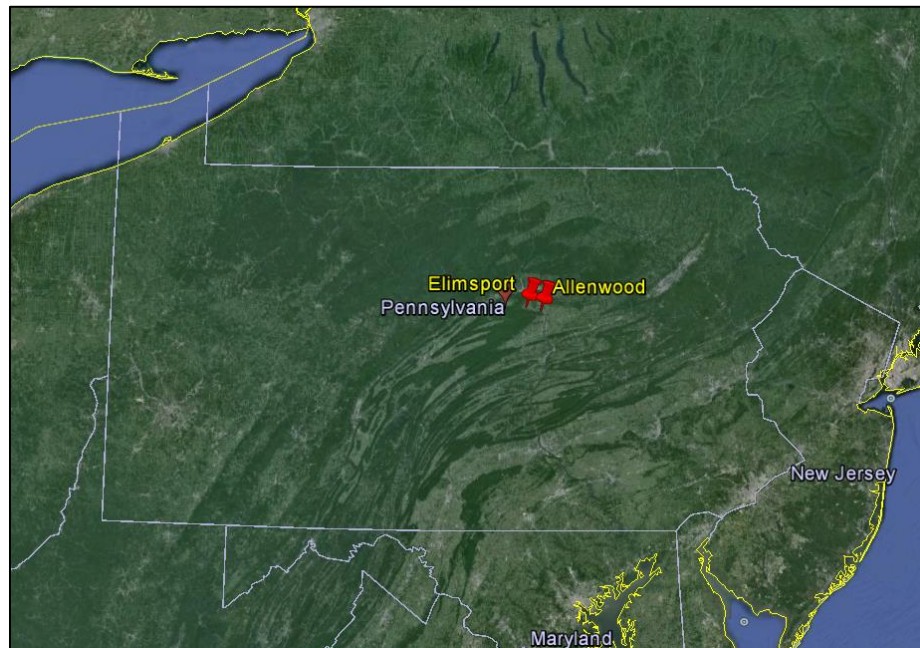
Fig. 2.1 – Location of Marcellus Shale Outcrops (Google Earth)

As shown in the background of Fig. 2.2, the outcrop samples were exposed to the

elements, and most of the material on the surface of the debris pile was both friable and

soft, most likely as a result of water imbibition by the shale. After selecting suitable

samples that appeared undamaged by weathering, they were wrapped in polyethylene

and bubble wrap to lessen the effects of humidity and minimize shipping damage.
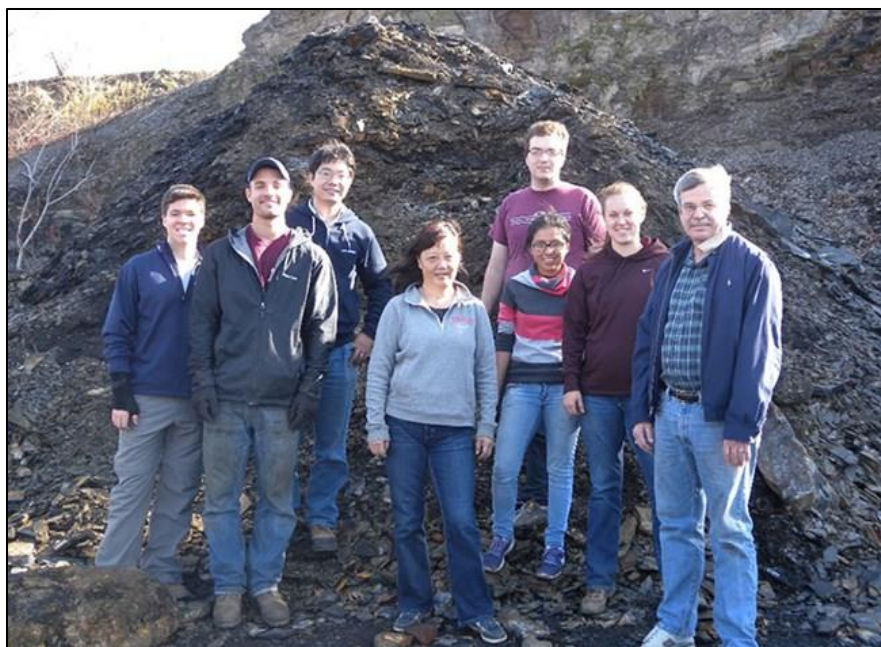
Fig. 2.2 – Research Group at Elimsport Outcrop Site

The second set of 10 samples was obtained from an excavation site in Allenwood, Pennsylvania. This site is approximately 10 miles from the Elimsport location, and samples were purchased from a third party. The parent rock for these samples was excavated from 20 feet underground, isolated from the potentially harsh effects of weathering.

Mineralogy of both sample sets was then assessed using X-Ray Diffraction (XRD). The machine and software used to analyze these two samples is only capable of qualitative, rather than quantitative, analysis. The results of the mineralogical testing are shown in Fig. 2.3, and highlight only the presence of minerals, not the volumetric concentrations thereof. The Elimsport and Allenwood samples appear to be very similar

based on qualitative analysis, but quantitative analysis was required to determine that the concentrations of minerals is representative of the Marcellus shale. Third-party quantitative XRD analysis of an Allenwood sample was performed, which revealed that the mineral content of these samples is in line with established literature values. Although the exact volumetric concentration of minerals in the Elimsport samples remains unknown, the qualitative results indicating that the Elimsport and Allenwood samples are very similar can be used to draw the conclusion that the Elimsport samples are also representative of the Marcellus shale. Table 2.1 compares these results to examples of Marcellus shale from other literature.

Having verified that the collected samples have similar mineral volumetric concentrations to the samples from literature, the samples were cut to fit into the modified API conductivity cell. In order to preserve sample material, a thin (1.5-2 inches thick) shale sample was cut, and then backed with Berea sandstone to make up the remainder of the required six-inch sample thickness as depicted previously in Fig. 1.12.
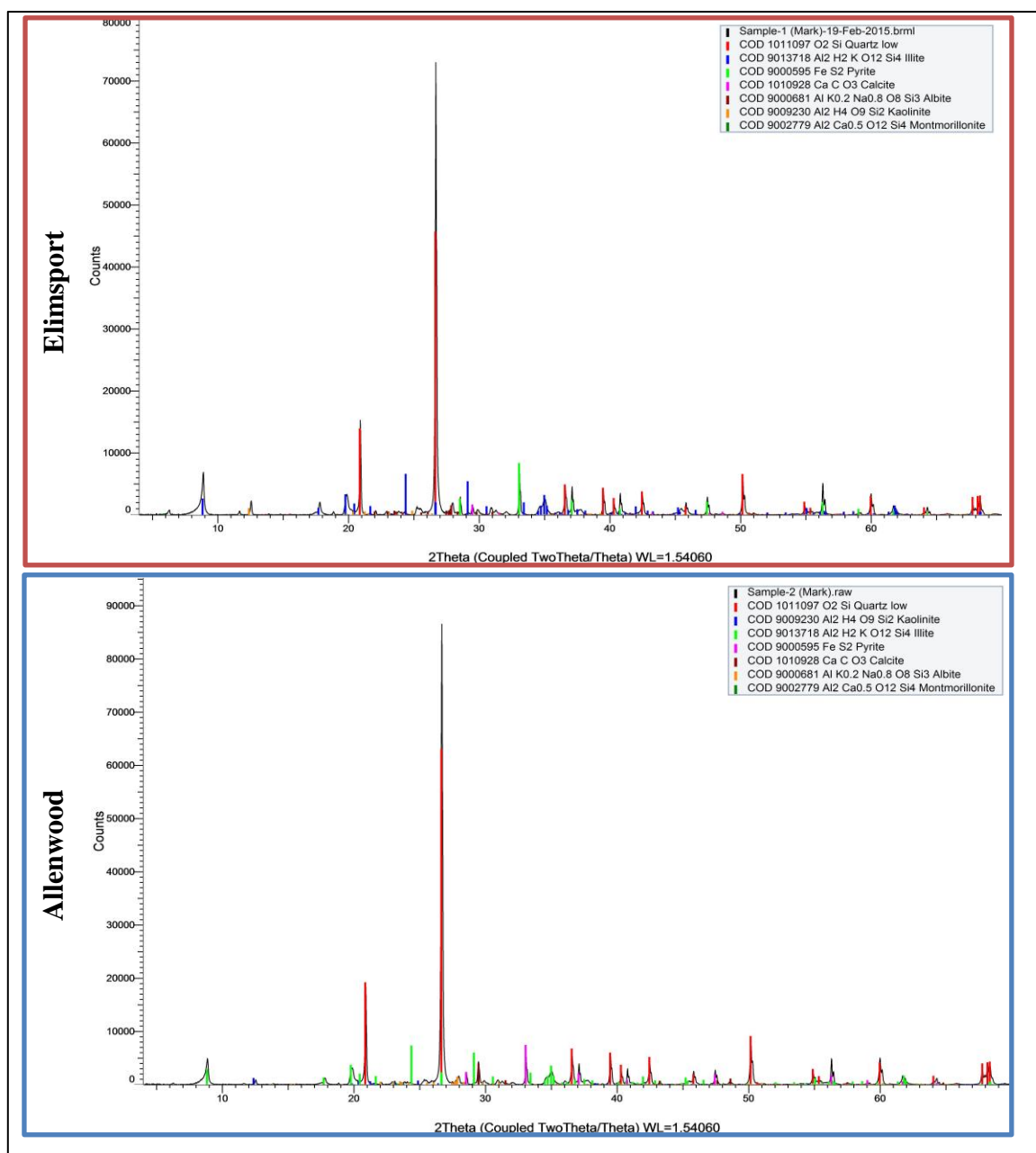
Fig. 2. 3 – Sample XRD Results

Table 2.1 – Mineral Content of Various Marcellus Shale Samples by XRD Analysis
(Boyce and Carr, 2009; Lash and Engelder, 2011; Olusanmi and Sonnenberg, 2013;
Wang and Carr, 2013)

Sample	Quartz %	Calcite %	Dolomite %	Pyrite %	Clay %
Allenwood	41	12	1	12	25
Boyce and Carr	67.4	0.3	0	5.2	27.2
Lash and Engelder, Sample A	48	4	0	15	33
Lash and Engelder, Sample B	58	19	0	4	19
Olusanmi and Sonnenberg, Sample A	50	4	2	8	36
Olusanmi and Sonnenberg, Sample B	48	41	0	0	11
Olusanmi and Sonnenberg, Sample C	35	5	2	10	48
Wang and Carr, Sample A	62.04	8.25	0	0	29.71
Wang and Carr, Sample B	50.12	28.96	0	0	20.93
Wang and Carr, Sample C	46.30	5.1	0	0	48.60

The standard API conductivity test for benchmarking proppant performance uses rough-sawn sandstone to model fractures. This method is well-suited for comparing proppant, but for this research, natural fractures were required to best represent operational conditions. Using a masonry rock splitter, fractures were induced in the samples in a manner shown in Fig. 2.4.
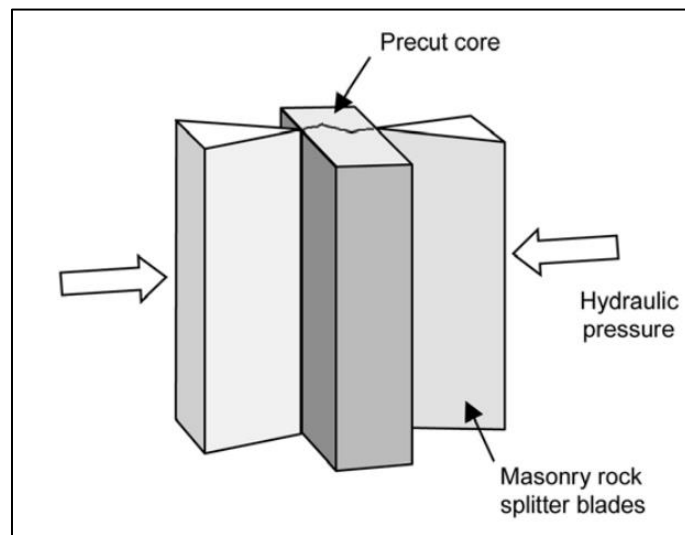
Fig. 2.4 – Inducing Mode I Fracture in Samples (Fredd et al., 2001)

The compressive forces from these blades are translated as tensile forces at the fracture initiation site, resulting in a Mode I fracture. As a goal of this work was to compare horizontal and vertical fracture conductivity, half of the samples were fractured in a manner that resulted in horizontally-oriented fractures, and the other half were fractured to create vertically-oriented fractures.

To approximate horizontal fractures, samples were broken parallel to the bedding planes. Although the bedding planes may have a non-zero dip angle at formation depths, the dip angle is assumed to be low enough to make this a valid approximation. That said, fractures in formations such as the Marcellus do not usually propagate horizontally because of the large overburden pressure at depth. However, the current literature on the subject of propped fracture conductivity has used horizontally-fractured samples for discussion. Operators who test fracture conductivity also generate samples with this fracture orientation, meaning that horizontally-fractured samples remain the best way to compare results from this work to those from previous studies or operator data.

Vertically-fractured samples were cleaved perpendicular to the bedding planes; this more closely approximates flow through a vertical fracture. As depicted in Fig. 2.5, there are three basic flow paths within the two possible fracture orientations that could impact fracture conductivity. This study uses samples fractured in the first and third configurations. Zhang (2014) asserted that fracture conductivity is independent of fracture orientation, as several properties that dictate fracture conductivity such as mineralogy, interaction with water, and proppant distribution are not directional. However, properties such as Young's Modulus and Poisson's Ratio, both of which are related to crack propagation direction, are usually anisotropic in layered materials such as shale.
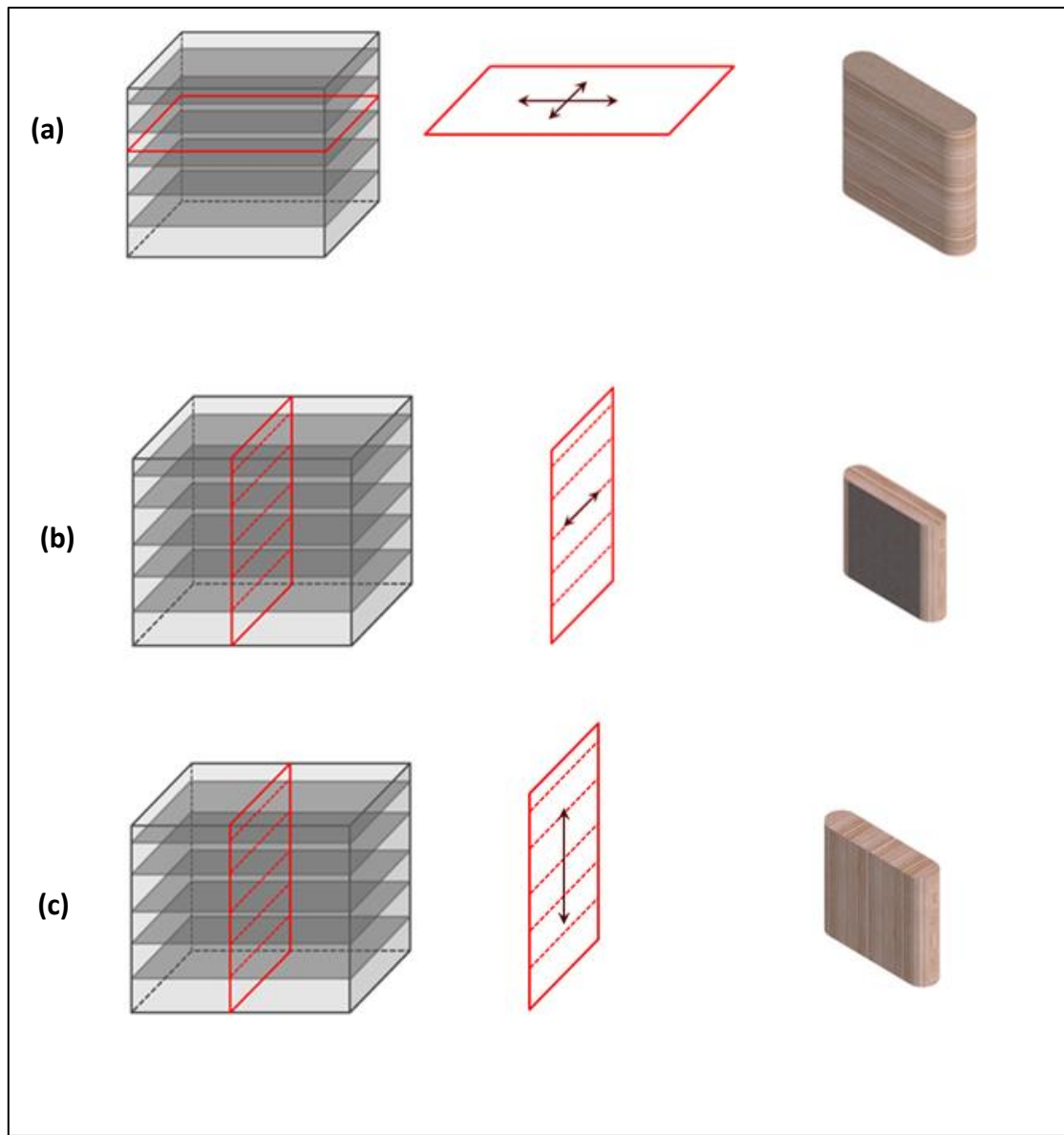
Fig. 2.5 – (a) Horizontal Flow in a Horizontal Fracture, (b) Horizontal Flow in a Vertical Fracture, and (c) Vertical Flow in a Vertical Fracture

In many cases, fracturing resulted in fracture infill material that had spalled from the surface. This infill appeared to be anhydrite or shale, which has been noted in other literature (Zhang, 2014). In-situ spalled material acts as a low permeability proppant, helping to increase fracture width (Kamenov, 2013). Care was taken to ensure that infill

remained as close to its original position as possible by cutting rocks in such a manner as to minimize vibration and material loss. Following the sample fracturing process, the samples were taped for shipment.

While many fracturing fluids are water-based, shale is sensitive to swelling by means of water imbibition, and this would destroy the samples at high closure stress, cause significant changes in the fracture's surface characteristics, or irreversibly change elastic properties essential to fracture conductivity. Similar irreversible changes also occur with use of synthetic fracturing fluids. As sample availability was limited, room-temperature nitrogen gas was used as the fluid for all conductivity tests.

40/70 mesh natural white sand was used as the proppant for these experiments and was sourced from an open-pit mine in Wisconsin operated by Badger Mining Corporation. This proppant was manufactured in compliance with ISO 13503-2:2006. Because proppant was placed manually, as opposed to being pumped into location as slurry, proppant tended to accumulate on the sample's troughs and plateaus as depicted in Fig. 2.6.
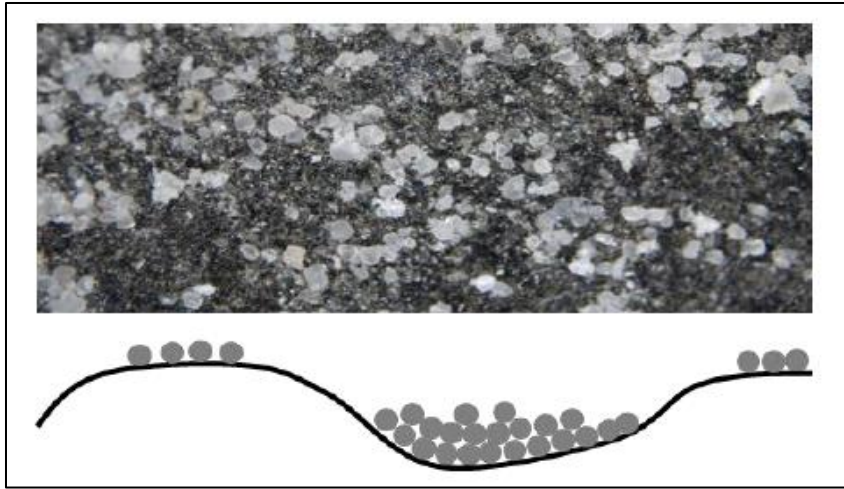
Fig. 2.6 – Depiction of Distribution of Proppant on Rough Marcellus Fracture (Zhang, 2014)

2.3   Methodology of Sample Preparation

Significant preparation is required to make suitable samples for conductivity testing. This section attempts to describe a procedure to consistently create functioning samples. The following supplies are required for this procedure:

- Silicone potting compound (Momentive RTV 627)

- Silicone release spray (Molykote 316)

- Rubber adhesive primer (Momentive SS 4155)

- Two-part epoxy glue

- Sample mold (clamshell halves, baseplate, and screws)

- Aluminum tape

- Personal attire: lab coat, long pants, close-toed shoes, protective eyewear, and
  latex or nitrile gloves

- Box cutter/utility knife

- Permanent marker

- Contractor's masking tape

- Steel wool

- Tongue depressor

- Large weights or 24-in bar clamps

- Acetone

- Allen wrenches

- Scoopula

- Putty knife

- Foam brush

- 250 gram scale

- Tabletop sample oven

The silicone potting compound described, Momentive RTV 627, has a cure time curve shown in Fig. 2.7. For this work, samples were cured for a period of three hours at 160 °F. Through trial-and-error, this was found to be the temperature that optimized the cured epoxy's strength and malleability. Curing at higher temperatures results in a sample with a more brittle epoxy coating; this is undesirable, as brittle epoxy tends to tear and delaminate from the substrate under the compressive loading of the conductivity tests, making reapplication of epoxy necessary in order to repeat testing on the same specimen.
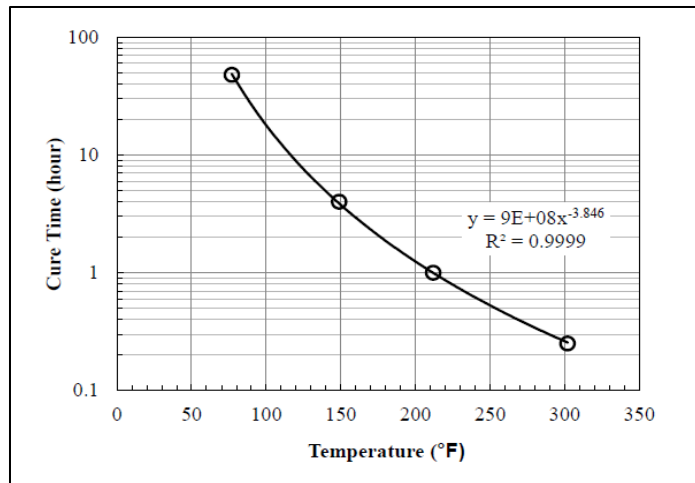
Fig. 2.7 – Epoxy Cure Time as a Function of Temperature, Momentive RTV 627
(Zhang, 2014)

The clamshell-type sample mold is 0.003 inches wider than the modified API
conductivity cell used in fracture conductivity testing. This makes for a slight
interference fit, ensuring that leakage is unlikely, even at high pressures. The mold is
0.15 inches wider than the bare rock specimens, meaning that uniformly centered in the
mold, the epoxy coating is 0.075 inches wide around the entire sample. The sample
mold is shown in Fig. 2.8.
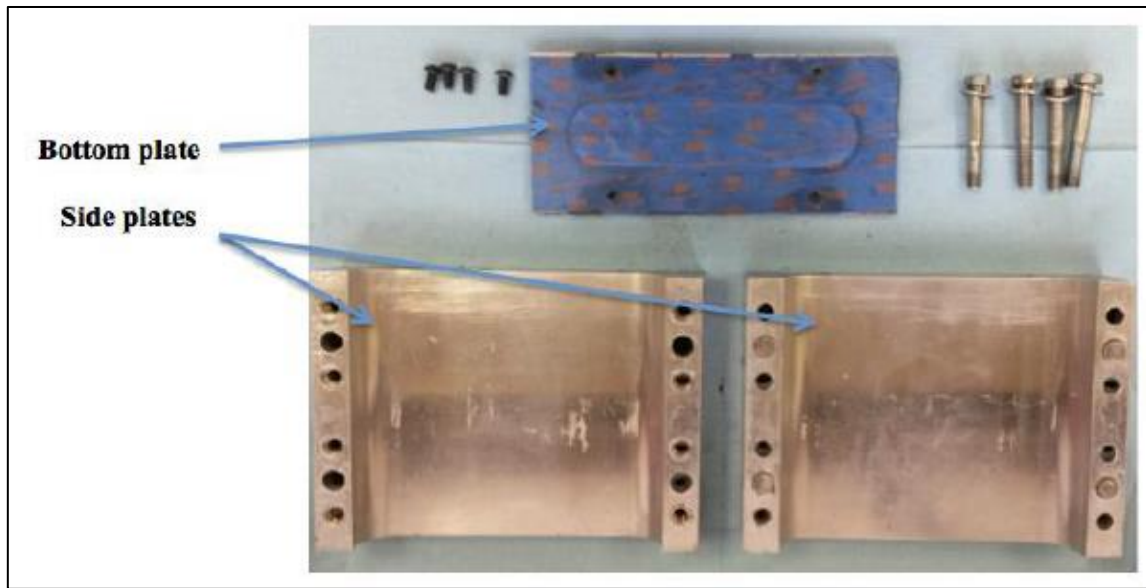
Fig. 2.8 – Sample Preparation Mold Without Aluminum Tape (Guzek, 2014)

The procedure for preparing a Marcellus shale sample is as follows:

(1)   Don protective eyewear, lab coat, long pants, closed-toe shoes and nitrile
        gloves

(2)   Open package containing sandstone backing and shale sample from Kocurek
        Industries using box cutter

        Note: The package should stay sealed until a sample is ready to be prepared,
        as moisture can affect the sample's physical characteristics

(3)   Place paper towel under work area to prevent glue from bonding to work
        surface

(4)   Remove protective tape from sandstone backing and shale sample

> **Note:** Kocurek Industries has induced a fracture on the shale sample, so it is extremely important to avoid dropping the sample or damaging it in any way. Once the tape has been removed, use caution to keep both halves of shale sample together

(5) With permanent marker, label sandstone with sample designation and flow direction

> **Note:** Sandstone should have the following information: Left/Right, sandstone thickness in inches, and sample name

> **Note:** Sample name has the following format: first two digits are sample number (01-99), followed by parent rock name (Rock A = RA, unknown parent = RX), followed by mold height (tall=T, short =S), followed by fracture direction (H=horizontal, V=vertical)

(6) Re-tape shale sample around the fracture circumference using masking tape. Coarsen tape surface with steel wool to improve adhesion of rubber epoxy, using steel wool to remove tape's non-stick coating

(7) Prepare two-part glue epoxy using provided glue basin and tongue depressor

> **Note:** Total required amount should not exceed 1-2 teaspoons

(8) Apply thin, even layer of glue to sandstone with tongue depressor, and attach shale sample

(9) Apply thin, even layer of glue to other sandstone piece, and place on top of shale sample

(10)   Apply weights or bar clamps to complete sample, wiping away excess glue

from sample with paper towel

Note: Applying weight or bar clamp pressure may cause sample

misalignment. Do not leave sample unattended until sample and

sandstone surfaces are flush with each other

(11)   Using paper towel, wipe off the glue basin and tongue depressor so that they

may be used again

(12)   Allow glue to dry and cure for 30 minutes at minimum

(13)   Use acetone to clean sample mold surfaces

Note: If mold has been modified with aluminum tape (used to reduce the

inner cavity dimensions), be sure to inspect mold for creases or wrinkles.

If aluminum tape is excessively worn, it must be replaced

Note: To replace aluminum tape (only if required), remove old tape, apply

acetone to bare surface, re-apply tape, and cut to size of mold with box

cutter

(14)   Place mold halves and base in fume hood, and turn on fume hood vent

(15)   Apply three coats of silicone release spray to all interior surfaces of mold,

waiting five minutes between each application

(16)   Apply a small dab of rubber primer to foam brush over aluminum pan in

fume hood, and then brush onto conductivity core sample (both shale and

sandstone portions)

Note: Sample requires three coats of primer. Wait until white color develops

on drying primer before applying subsequent coat (usually 10-20 minutes)

(17)   Remove mold baseplate and one half of clamshell from fume hood, and place

on flat, clean surface

(18)   Screw baseplate onto one half of the clamshell using two short screws and

Allen wrench

(19)   Turn over baseplate and clamshell assembly, and carefully place sample

inside the mold

Note: Visually align the vertical edges of the sample with the mold, making

sure both edges are evenly spaced from the mold. See Fig. 2.9.
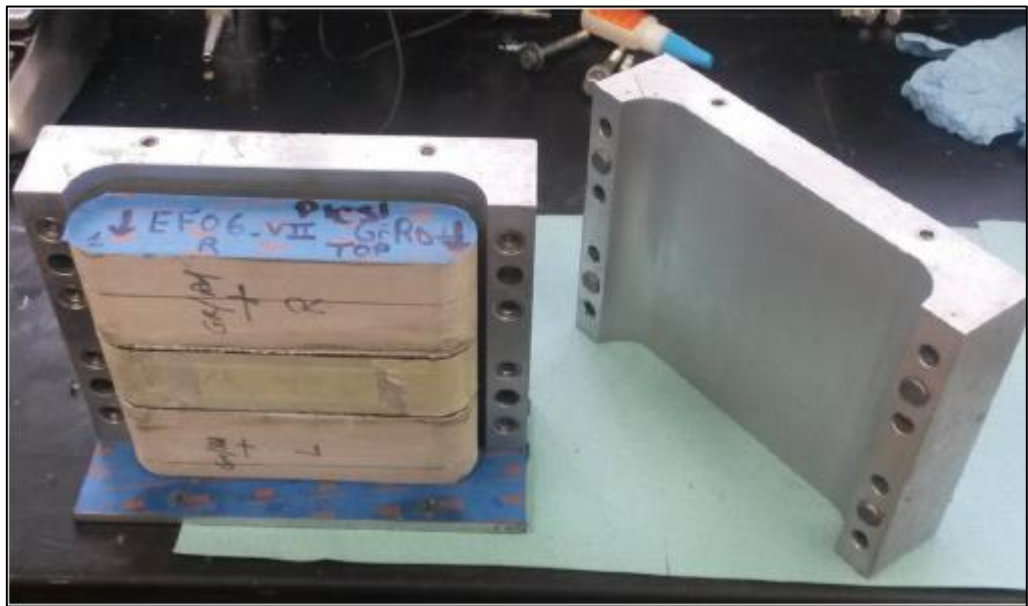
Fig. 2.9 – Aligning Sample Inside Sample Preparation Mold (Guzek, 2014)

(20) Attach the second half of the clamshell to the baseplate, using two short screws and Allen wrench

(21) Secure two halves of the clamshell to each other using four long screws and Allen wrench

(22) Visually inspect the assembly from top view. The sample should be spaced evenly from all mold surfaces

(23) Place plastic cup on 250 gram scale, and tare scale to account for weight of cup

(24) Remove cup from scale, placing on flat surface covered with paper towel

(25) Using hand-pump bottles, dispense 110 g of white epoxy compound into 12-oz cup

Note: Depress hand-pump 21 times, then add remaining amount with cup on the scale

(26) Repeat step 25 with the black epoxy component

(27) Using scoopula, stir the epoxy together so that it is an even gray color, with no areas of isolated black or white

Note: Use scoopula to make sure edges and bottom of cup are well-mixed

Note: Once mixed, quickly but diligently complete sample preparation, as curing begins immediately and epoxy begins to congeal within 20-30 minutes

(28)   Slowly pour epoxy out of cup directly onto top surface of sample, and allow

       to flow over the sample and down the annulus between the sample and mold

       wall

       Note: Overflow should ideally occur on the long edge of the sample, and

          preferably at just one location initially

       Note: Ensure that the overflow occurs at a slow rate. The goal is to always

          maintain a gap between the flowing epoxy and mold interior's top surface

       Note: As a rule of thumb, the pouring process should take 10-20 minutes

(29)   Using putty knife, wipe off epoxy from top of sample to ensure that label can

       be read

(30)   Carefully move sample to oven, and place in oven at heat level 3.5 (160 °F)

       for approximately three hours

(31)   Remove sample from oven using thick leather gloves, and allow to cool for

       two or more hours

(32)   After sample and mold have cooled, unscrew assembly, remove mold, and

       clean sample mold with acetone for next use

2.4   Methodology for Surface Roughness Measurement by Laser Profilometer

To best assess if surface roughness plays a role in fracture conductivity as

previously ascertained by Kamenov (2013), fracture surface roughness must be

quantitatively determined using the root-mean-square roughness, where R_{RMS} can be

described as,

$$R_{RMS} = \sqrt{\frac{1}{n}\sum_{i=1}^{n}y_i^2} \quad \text{..(2-1)}$$

$$y_i = |y - \bar{y}| \quad \text{..(2-2)}$$

Calculated in this manner, a completely smooth but sloped surface devoid of local non-linearity would have a non-zero root-mean-square surface roughness. Samples scanned for this work were not sloped; fractures exhibited local non-linearity in the form of peaks and troughs, and the fractures were aligned such that they were as close to perpendicular to the optical element as possible.

The laser profilometer used to determine roughness is shown in Fig. 2.10. This device raster scans each sample, and is capable of measuring the height of the sample at each measuring point to an accuracy of 0.000001 inches. It can also measure roughness of a rough sample with significantly different peaks and troughs, as the laser has a full scale resolution of one inch.
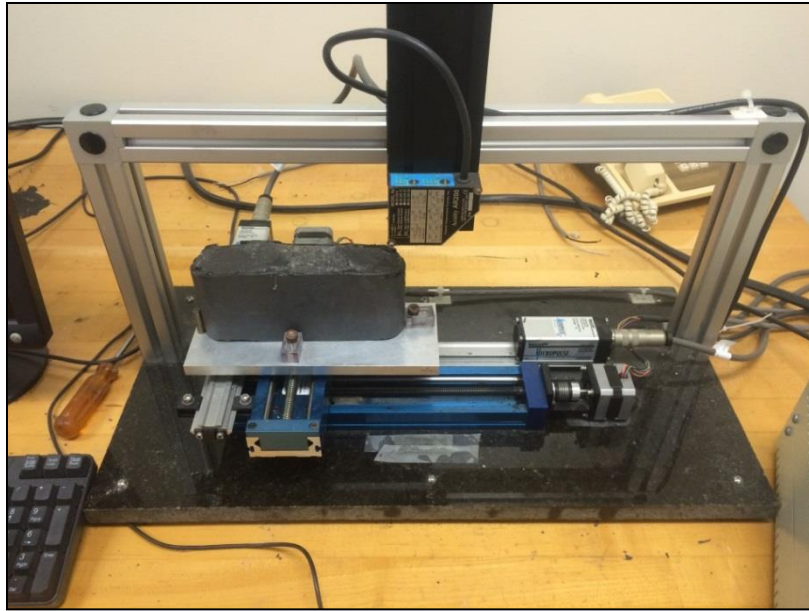
Fig. 2.10 – Surface Roughness Scanning

The components required for this work are:

- Split shale sample

- Laser profilometer

- Laser profilometer control box

- Data acquisition system

Surface roughness scans were performed before conductivity testing and after each test in order to determine if the surface roughness changed as a result of cycling closure stresses. The full procedure for determining surface roughness is shown below:

(1)   Clean off sample surfaces and remove any proppant or debris using air gun

(2)   On the control box, turn on laser profilometer

(3)   After logging onto computer, open LabView for laser profilometer

        Note: Location: Local Data **/** PF-06 ver14_pete **/** Application.exe

(4)   On control box, toggle x-axis and y-axis switches to "Manual"

(5)   Adjust x-axis and y-axis to "zero" positions, which are indicated on the monitor

(6)   Toggle x-axis and y-axis switches to "Auto"

(7)   Enter sample information into LabView

        Note: File Setup → Save file

        Note: Sample Setup → Enter name, experiment number, and sample dimensions

        Note: Sample length is 7 inches, width is 1.7 inches, and raster width is 0.05 inches

(8)   Select "Start"

(9)   After sample is finished scanning (nominally 105 minutes), turn off LabView and profilometer

2.5   Methodology for Conductivity Measurement by Gaseous Nitrogen

In order to determine fracture conductivity of the Marcellus shale samples, this study uses a modified API conductivity cell as previously used and described by Zhang (2014), Briggs (2014), Guzek (2014), Kamenov (2013), and Awoleke (2013). This experimental set-up includes the following key supplies and components:

- GCTS UCT-1000 Uniaxial Testing Apparatus

53

- Modified API conductivity cell

- Validyne DP-15 pressure transducers (3)

- Aalborg Mass Flow Controller

- Data acquisition system (GCTS Controller and Windows computer)

- Nitrogen tank

- Conductivity core sample

- Hydraulic press

- Personal attire: lab coat, long pants, close-toed shoes, protective eyewear, and
  latex or nitrile gloves

- Teflon tape

- Allen wrench

- Scissors

- High vacuum grease

- Open-ended wrench

- Screwdriver

- Pipe snoop or soapy water

- Box cutter

Some previous literature also included valuable information pertaining to this work that is not included here. Zhang (2014) includes part numbers and vendor information for important fracture conductivity experiment components in Appendix B of his work. The Validyne DP-15 pressure transducers used in this work to determine

pressures required for conductivity calculations must be regularly calibrated, and Awoleke (2013) includes a thorough discussion thereof. While the following procedure offers suggestions to avoid problems and minor troubleshooting tips, a more thorough list of troubleshooting advice has been established by Zhang (2014).

A schematic of the complete experimental set-up is shown in Fig. 2.11. Detailed below is a procedure to successfully determine fracture conductivity for Marcellus shale samples. The nitrogen tank is typically tapped at a pressure of approximately 2,200 psi, and is operational down to a pressure of 800 psi, at which point a new tank must be installed. As described by Zhang (2014), the GCTS uniaxial load frame, which is used to supply closure stress on the sample, can provide up to 208,000 lb-f at a rate of 1,215 lb-f per minute. Using a sample with a surface area of 11.59 in., the load frame can supply almost 18,000 psi on the modified conductivity samples. In these experiments, the compressive load is increased at a rate of 100 psi per minute. The Aalborg mass flow controller, which is used to measure the nitrogen flow rate, can measure flow in increments from 0.001 standard liters per minute, up to 10 liters per minute. This level of accuracy is more than sufficient to provide the high-level conductivity relationships being established. A needle valve at the gas outlet is used to finely regulate the system pressure. Gross adjustments to the system pressure can be made by adjusting the nitrogen tank's regulator's set point.
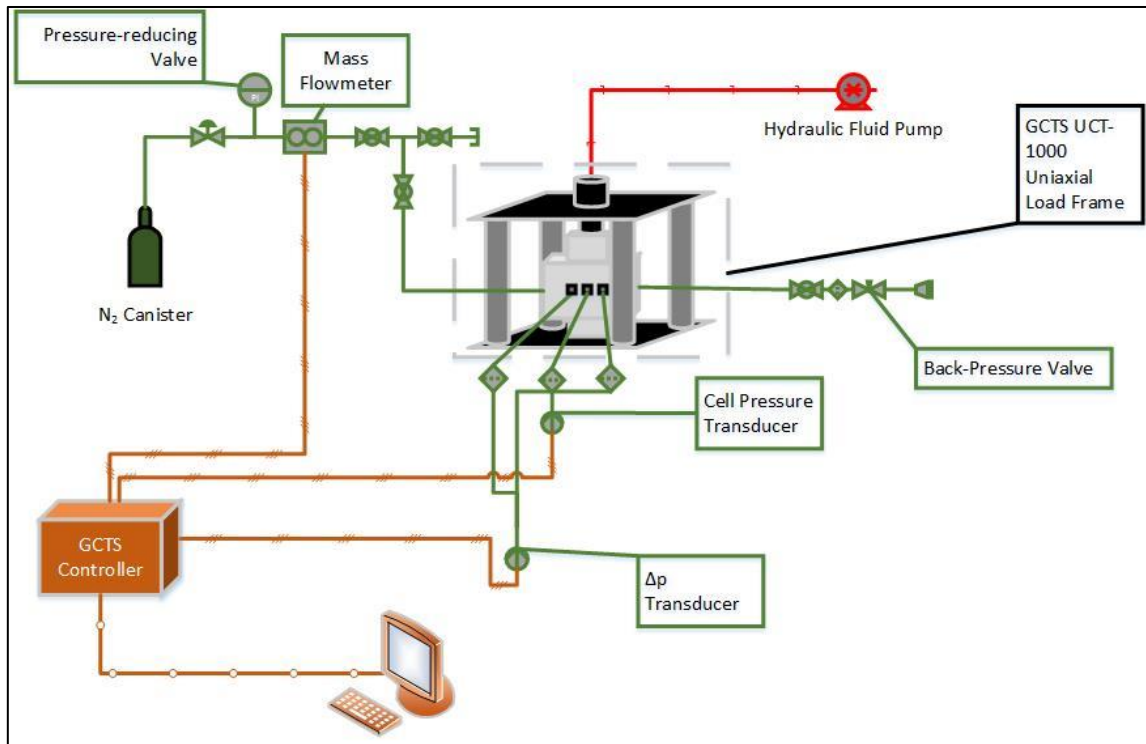
Fig. 2.11 – Schematic of Experimental Set-up for Determination of Fracture
Conductivity

The full procedure for determining fracture conductivity is shown below:

(1)   Don protective eyewear, lab coat, long pants, closed-toe shoes and nitrile

        gloves

(2)   Mark three spots on the sample where pressure transducer ports will be

        located

        Note: In the horizontal direction, the three ports are centered about 0.875",

           3.5", and 6.125"

        Note: In the vertical direction, the three ports are centered about 3"

56

(3)   Using the box cutter, cut 0.5" squares around the pressure port marks using

an "X" pattern

(4)   Remove the epoxy and masking tape from cut area

(5)   Repeat steps 2-4 on the ends of the sample for nitrogen gas entry and exit

points

(6)   Apply 2-3 layers of Teflon tape to the sample in a horizontal orientation at

intervals 1.5" above and 1.5" below the pressure port holes, cutting tape with

scissors

(7)   Apply 2-3 layers of Teflon tape to the sample in the vertical direction

halfway between the outer and middle pressure ports, cutting tape with

scissors

(8)   Apply a thin layer of high vacuum grease to all exposed Teflon tape layers,

shown in Fig. 2.12.
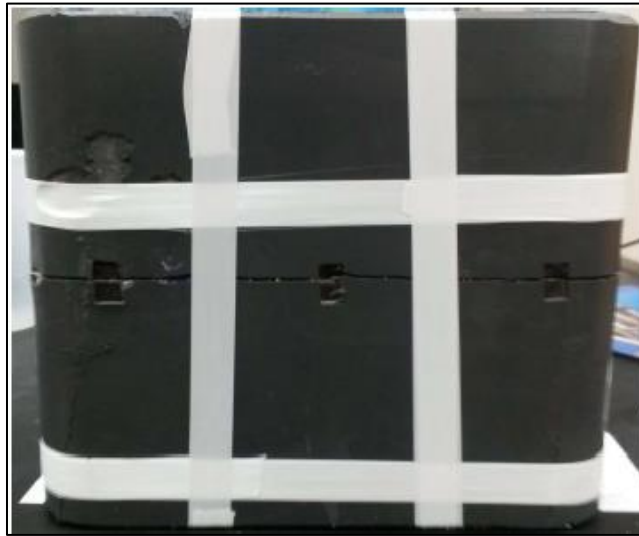
Fig. 2.12 – Fully-Prepared Sample (Guzek, 2014)

(9)   Apply a thin layer of high vacuum grease to interior surface of conductivity
        cell

(10)   Place conductivity core sample in conductivity cell

        Note: The sample must be first manually pressed into the conductivity cell in
           order to fit underneath the hydraulic press' ram

(11)   Using hydraulic press, finish pressing the sample into proper location in the
        conductivity cell

(12)   Check alignment of the core, using small screwdriver or thin metal rod to
        make sure that exposed rock is directly in contact with pressure transducer
        ports.

        Note: Exposed rock makes a different sound than Teflon tape or epoxy

(13)   Press both pistons onto either end of the conductivity cell, and use stabilizing

sleeve on bottom

Note: If O-rings appear dry, apply O-ring grease

(14)   Tighten bottom piston's bleed port bolt to prevent leaks

(15)   Move sample, conductivity cells, and pistons to GCTS UCT-1000 apparatus

and align in center of test area

(16)   Turn on GCTS UCT-1000 control box

(17)   Plug in Aalborg mass flowmeter

Note: After mass flowmeter has fully turned on, adjust flowmeter

potentiometer screw, shown in Fig. 2.13, in rear of unit to read 0.00 L/min

Fig. 2.13 – Potentiometer Screw (Circled in Red) on Aalborg Mass Flowmeter

(18)　Open GCTS CATS Standard software, and adjust piston location until sample

is very slightly compressed (will not rock or move when pushed/pulled by

hand)

Note: Hydraulic Outputs → Switch tool to "On" → Outputs Function→

Adjust "Feedback" to "Axial Displacement" → Make desired changes to

axial position of load frame piston → Adjust "Feedback" to "Axial Load"
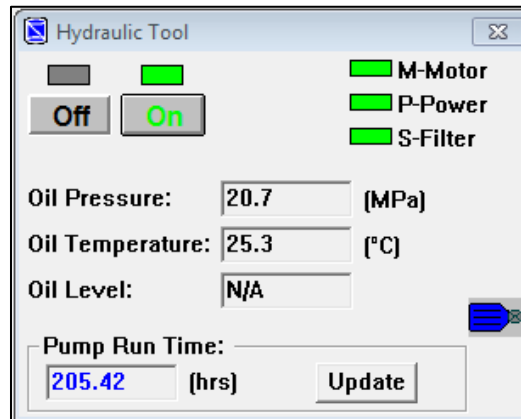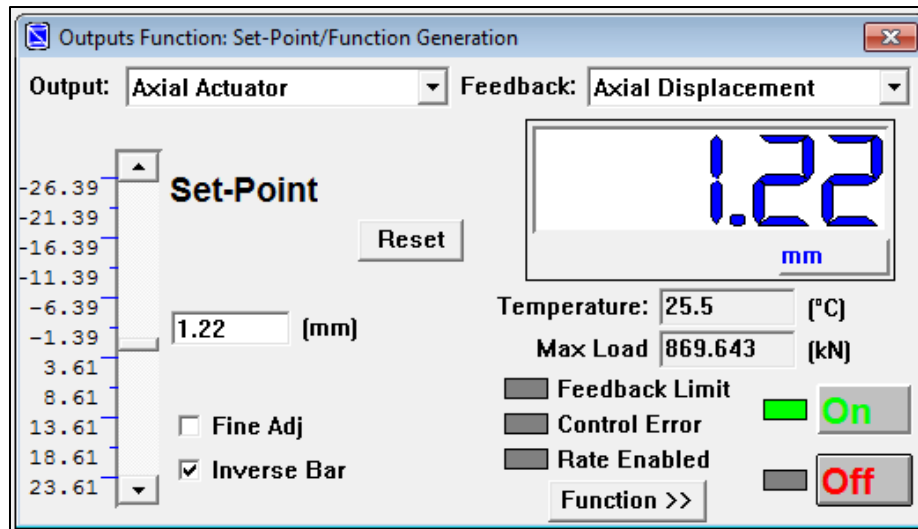
Fig. 2.14 – GCTS CATS Standard Screen Shots for Step 18

(19)   Create Project, Sample, and Specimen names

Note: Projects → Create new project or double-click existing project →

Create new sample name using pre-determined sample naming

convention → Create new specimen, usually the final pressure of that

test, i.e. "500psi", etc.

Fig. 2.15 – GCTS CATS Standard Screen Shots for Step 19

(20)   Apply 500 psi pressure using 500 psi ramp program

Note: Single-click on 0500psi_ramp.tpr → Select "Execute" → Select "Run"

63
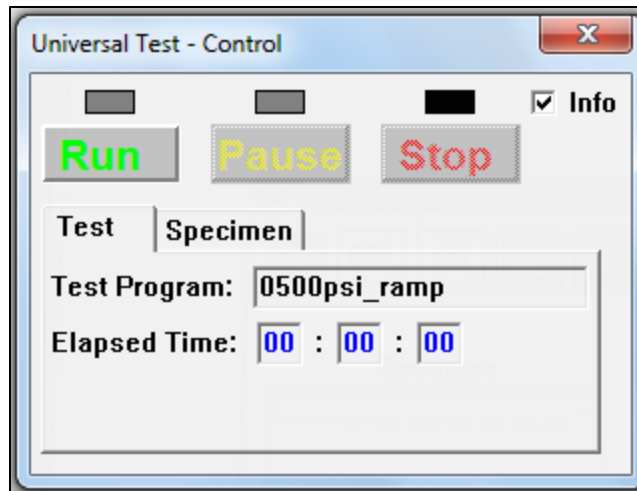
Fig. 2.16 – GCTS CATS Standard Screen Shot for Step 20

(21)   Open up appropriate load screen layout

Note: Views → Load Screen Layout → Select appropriate file
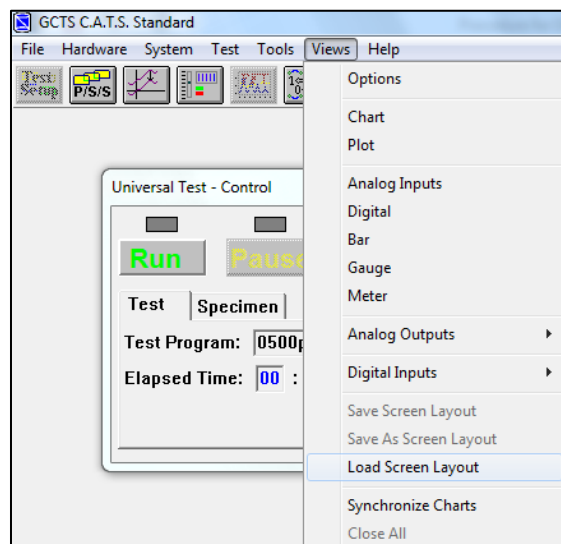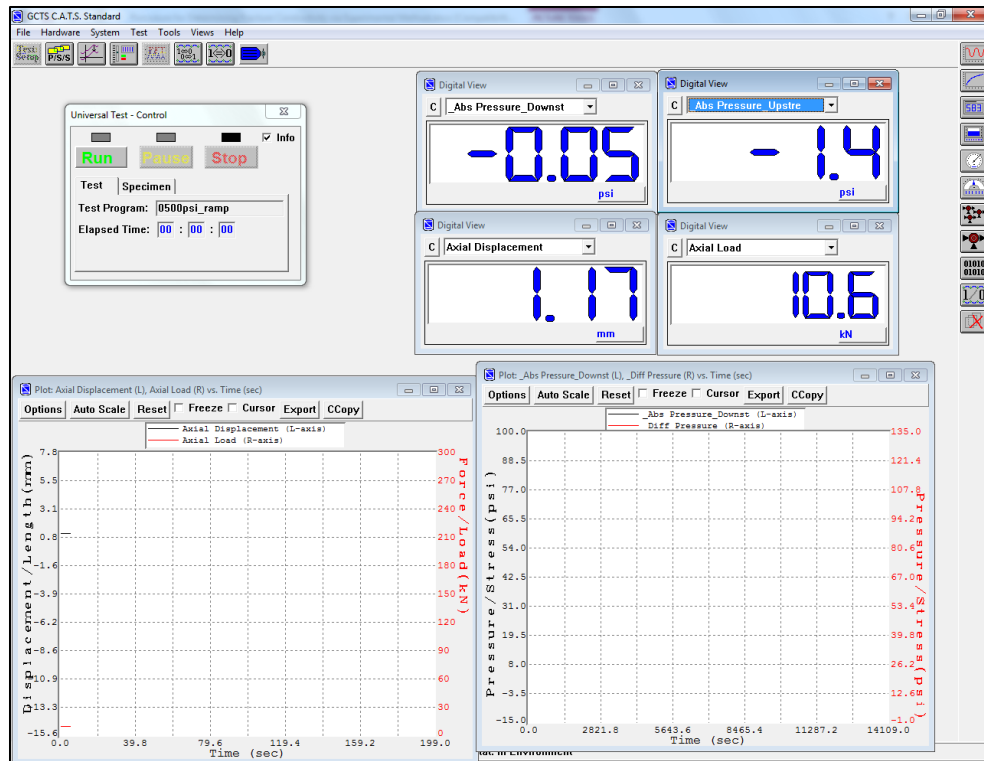
Fig. 2.17 – GCTS CATS Standard Screen Shot for Step 21

(22)   Attach both pressure transducers to appropriate locations, making sure that

transducers are oriented so that the wiring exits the bottom portion of the

transducer

(23)   Attach the conductivity cell flow inserts using four large screws and Allen

wrench

(24)   Attach gas flow inlet and outlet assemblies to end caps. When fully

assembled, the conductivity cell should appear as in Fig. 2.18.

Note: On all tubing connections, compression fittings are used. These

fittings are different than normal threaded connections, and do not require

excessive torque to provide seal (only ¼ turn beyond hand-tight is

required)

Note: Do not use Teflon tape on tubing fittings
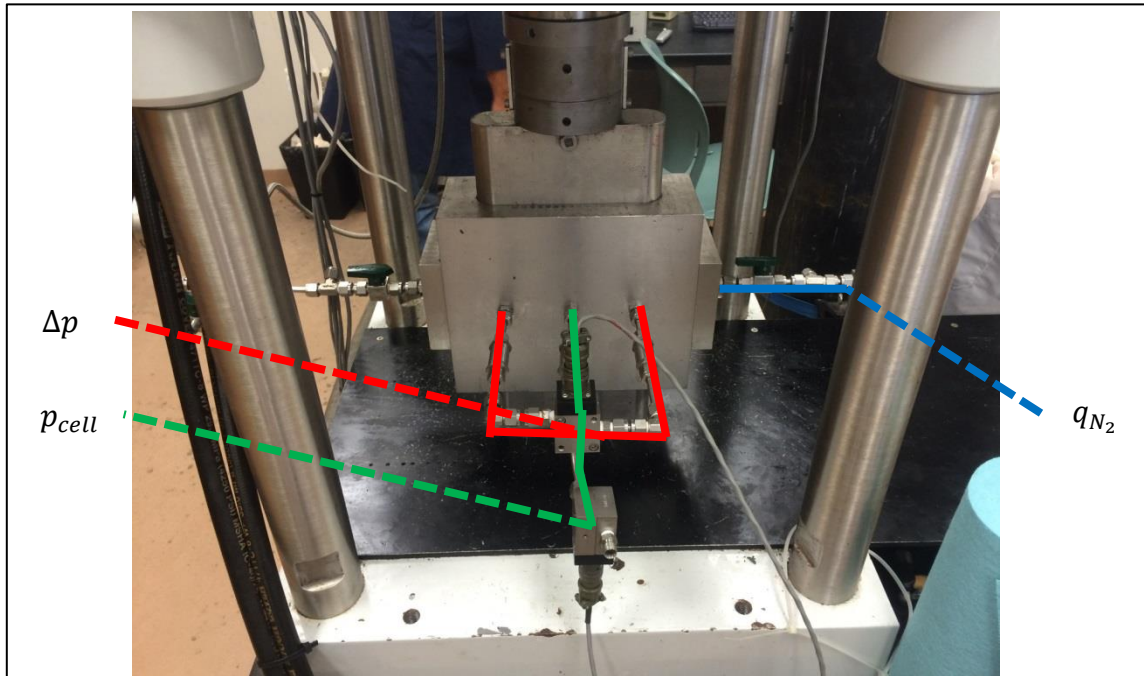
Fig. 2.18 – Fully-Assembled Conductivity Cell

(25)   Prior to opening nitrogen tank root valve, make sure that valves are in the

proper position: tank regulator completely closed, gas inlet valve open, gas

backflow valve closed, gas inlet bleed valve closed.

(26)   Open the nitrogen tank root valve, and slowly open the regulator valve

(27)   Once gas has begun to flow into the assembly (confirmed with mass

flowmeter), continue to adjust regulator until pressure is approximately 30 psi

Note: Flow should never exceed 10 L/min through the mass flowmeter

Note: Do not expose the mass flowmeter to nitrogen prior to turning on- this causes problems because the mass flowmeter is only rated to 100 psi maximum working pressure

(28)   Screw on threaded fitting to top piston to seal off piston's potential means of gas egress

(29)   While back flow valve (valve on gas outlet side) is still closed, make sure that flow rate stabilizes to 0.00 L/min

Note: If there is flow, use pipe snoop to determine where leak is occurring (threaded fittings that are made up and disassembled for each experiment are particularly suspect)

(30)   Take four readings at 500 psi to determine fracture conductivity by opening backpressure valve at increasing levels. Each measurement point has the following requirements: the differential pressures must be 0.4-1.6 psi, and the cell pressure must be 25-30 psi. The flow rates should be significantly different at each reading (more than 0.05 L/min difference)

Note: Experiments should utilize four unique test points at each pressure stage. A good rule of thumb is to take readings at 20%, 40%, 60%, and 80% of the rated Δp of the differential pressure transducer's diaphragm. For these experiments, a diaphragm rated to 2 psi was used, so readings were recorded at each pressure step at 0.4, 0.8, 1.2, and 1.6 psi.

(31)   Enter results in Excel spreadsheet

(32) Close backpressure valve and move to next pressure step (1,000, 2,000, 3,000, 4,000, 5,000, and 6,000 psi) and repeat steps 28-31

(33) Close off nitrogen tank root valve

(34) Slowly open inlet bleed valve to release nitrogen pressure, ensuring that mass flowmeter is not exposed to an excessively high flow rate or pressure

(35) Switch piston back to "Axial Displacement" feedback

Note: Outputs Function → Feedback select "Axial Displacement" → Move piston upward
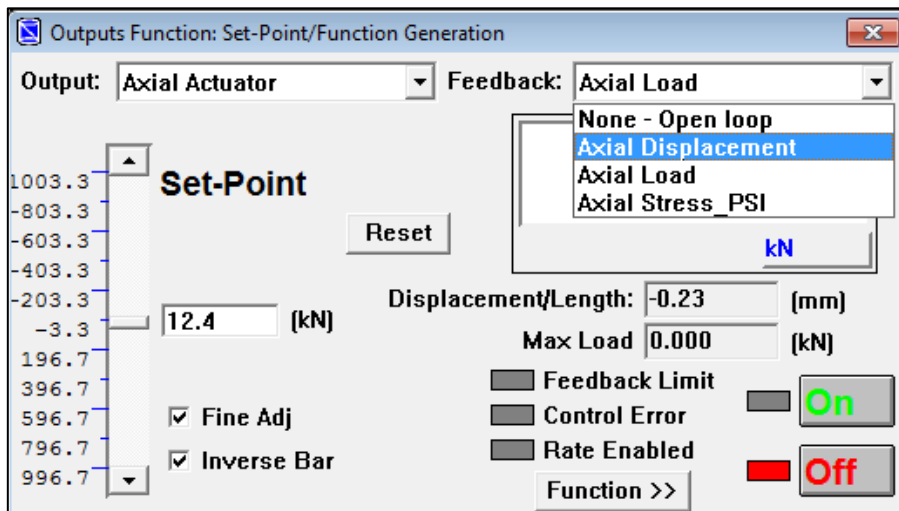
Fig. 2.19 – GCTS CATS Standard Screen Shot for Step 35

(36) Turn off GCTS controller software

Note: File → Shutdown Controller → Select Yes → Select Yes
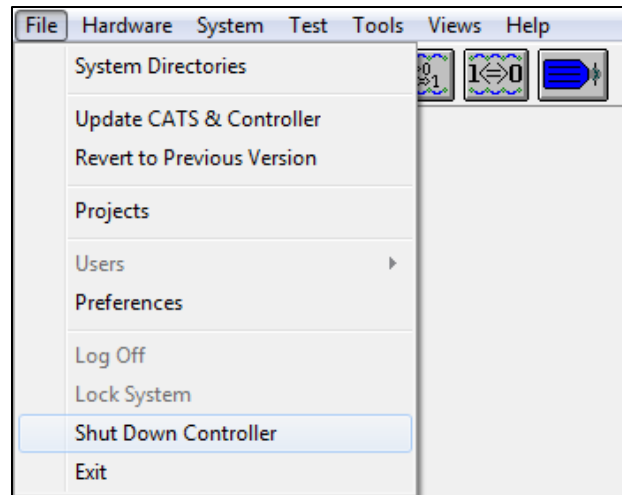
Fig. 2.20 – GCTS CATS Standard Screen Shot for Step 36

(37)   Turn off GCTS controller box

(38)   Unplug Aalborg mass flowmeter

(39)   Remove conductivity cell from GCTS apparatus, and remove sample using

hydraulic press

(40)   Clean off sample and conductivity cell (both will be covered in high vacuum

grease and Teflon tape)

(41)   Place conductivity cell and sample in appropriate storage locations

2.6   Determination of Fracture Conductivity

Both Darcy and Forchheimer flow are expected through the course of these

experiments. The flow path of nitrogen gas during experiments is shown in Fig. 2.21.

Fig. 2.21 – Flow Direction on Fractured Shale Sample with Proppant

For nitrogen flow rates less than two liters per minute, Darcy flow is expected. Above this rate, Forchheimer's equation is used to calculate fracture conductivity. Regardless, the conductivity values calculated via Darcy's Equation and Forchheimer's Equation are very similar at the closure stresses tested in this study, as depicted in Fig. 2.22. For these experiments, Forchheimer's equation was typically used to calculate conductivity up to 2,000-3,000 psi; after that, nitrogen flow rates were sufficiently low to allow use of Darcy's equation.
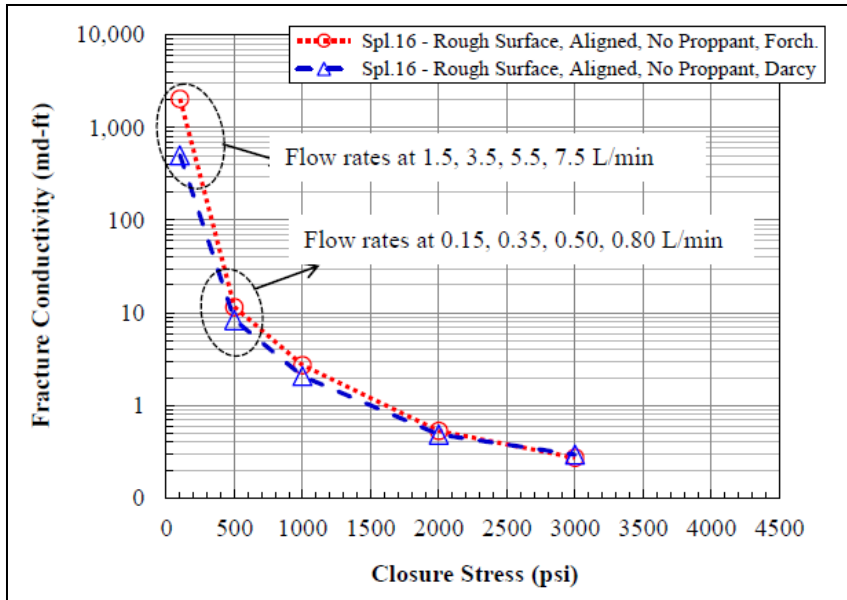
Fig. 2.22 – Fracture Conductivity via Forchheimer and Darcy Equations (Zhang, 2014)

During experiments, three measurements are made: the nominal pressure of nitrogen in the fracture, the pressure drop across the cell, and the flow rate of nitrogen gas. Using Darcy's Equation, the Real Gas Law, and an equation to describe gas flux, conductivity can be determined explicitly.

Darcy's Law:

$$q = \frac{kA\Delta p}{\mu L}$$ ....(2-3)

Where fluid velocity can be described as,

$$v = \frac{q}{A}$$ ....(2-4)

Replacing terms,

$$\frac{dp}{dL} = \frac{\mu v}{k}$$ ....(2-5)

Moving terms, and multiplying both sides of the equation by the fluid density, ρ_f, yields,

$$\rho_f(dp) = \frac{\mu v}{k}\rho_f(dL) \quad \text{...(2-6)}$$

The relationship between velocity and mass flow rate can be expressed as,

$$\frac{W}{Av} = \rho_f \quad \text{...(2-7)}$$

Density, through the real gas law, can also be expressed as,

$$\rho_f = \frac{pM_g}{ZRT} \quad \text{...(2-8)}$$

Substituting the previous two equations into the modified form of Darcy's Law gives,

$$\frac{pM_g}{ZRT}(dp) = \frac{\mu v}{k}\frac{W}{Av}(dL) \quad \text{...(2-9)}$$

Integrating yields,

$$\frac{M_g}{ZRT}\int_2^1 p\, dp = \frac{\mu W}{kA}\int_2^1 dL \quad \text{...(2-10)}$$

$$\frac{M_g}{zRT}\frac{(p_1^2-p_2^2)}{2} = \frac{\mu W}{kA}L \quad \text{...(2-11)}$$

Substituting fracture dimensions for the cross-sectional area, A, and converting mass

flow rate to volumetric flow rate,

$$A = w_f h_f \quad \text{...(2-12)}$$

$$W = q\rho_f \quad \text{...(2-13)}$$

yields,

$$\frac{M_g(p_1^2-p_2^2)}{2ZRTL} = \frac{\mu q\rho}{kw_f h_f} \quad \text{..(2-14)}$$

$$c_f = k_f w_f \quad \text{...(2-15)}$$

$$\therefore \frac{M_g(p_1^2-p_2^2)}{2ZRTL} = \frac{\mu q\rho_f}{c_f h_f} \quad \text{...(2-16)}$$

Since only the nominal cell pressure, p_{cell}, and pressure differential, Δp, are calculated,

$$p_1 = p_{cell} + 0.5\Delta p \dotfill (2\text{-}17)$$

$$p_2 = p_{cell} - 0.5\Delta p \dotfill (2\text{-}18)$$

For Darcy flow in these experiments, $\frac{M_g(p_1^2 - p_2^2)}{2ZRTL}$ is plotted along the y-axis, and $\frac{\mu q \rho_f}{h_f}$ is

plotted on the x-axis. Fracture conductivity is computed as the inverse of the slope of

the linear line-of-best-fit between the four data points compiled at each closure stress.

Fig. 2.23 is a graphical interpretation of the calculation of fracture conductivity as

described above.
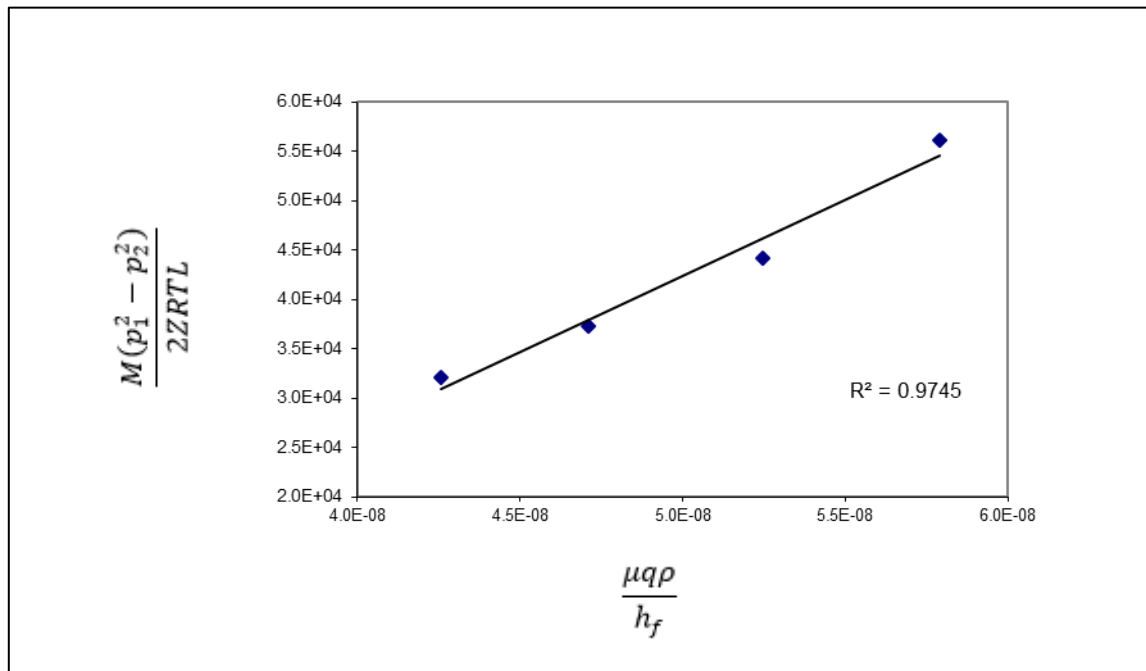
Fig. 2.23 – Computation of Fracture Conductivity via Darcy's Equation from
Experimental Results

When calculating fracture conductivity via Forchheimer's equation, a plot of

$\frac{M_g h(p_1^2 - p_2^2)}{2ZRTL\mu\rho_f q}$ vs. $\frac{q\rho_f}{\mu h_f}$ is created. The inverse of the y-intercept of this plot at each closure

stress gives fracture conductivity.

2.7   Proppant Concentration Calculations

In order to mimic realistic proppant loading, it is necessary to convert the

proppant concentration, reported in units of pounds of proppant per gallon of fracturing

fluid (ppg), to grams per sample. To make this conversion, an assumption on fracture

width is required. While a variety of propped fracture widths for shales are listed in

Table 2.2, the proper conversion in this case requires use of dynamic fracture width.

Table 2.2 – Various Estimations of Stressed Propped Fracture Width in Shale Plays

Source	Stressed Propped Fracture Width (in.)
Zhang, 2014	0.024
Izadi et al., 2014	0.043
Mashayekhi et al., 2014	0.01

Dynamic fracture width is the average fracture width obtained during the pumping phase

of fracturing. One means of calculating the dynamic fracture width, w_d, for an elliptical

fracture as predicted by the PKN fracture model is presented by Economides et al.

(2013),

$$w_d = 0.19 \left(\frac{q \mu x_f}{E^*} \right)^{1/4}$$ .... (2-19)

which provides similar fracture width values as those presented from experimental data

by Smith et al. (1982), who showed a dynamic fracture width between 0.1 and 0.2

inches. A figure of the PKN fracture geometry is shown in Fig. 2.24.
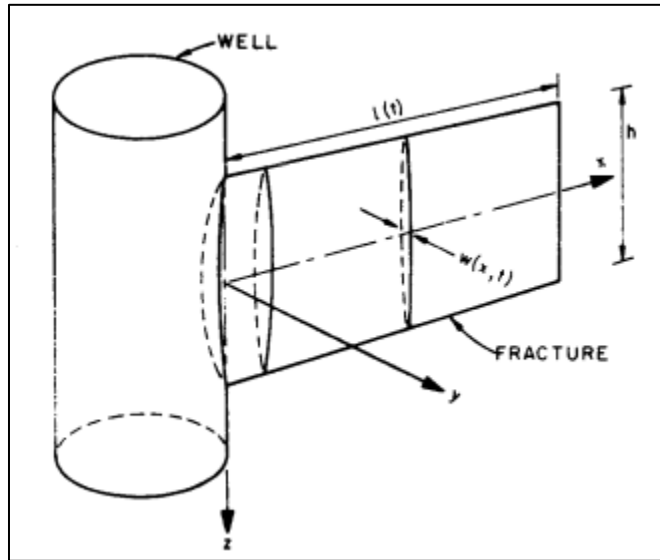
Fig. 2.24 – PKN Fracture Geometry (Nordgren, 1972)

Determination of the proper proppant mass to apply to each sample was

undertaken as follows:

$$m_p = \frac{x \; lb}{gal} \times \frac{453.592 \; g}{lb} \times \frac{42 \; gal}{Bbl} \times \frac{Bbl}{5.615 \; ft^3} \times \frac{ft}{12 \; in} \times \frac{ft^2}{144 \; in^2} \times 10 \; in^2 \times$$

$$0.125 \; in$$ .... (2-20)

where m_p is the proppant mass required for the sample, the sample's surface area is 10 in^2, and the dynamic fracture width is assumed to be 0.125 inches. The rest of the terms are conversion factors. This work also discusses proppant usage in terms of pounds per square foot; this allows others to mimic these experiments with samples of different sizes or under different fracture width assumptions.

3 PROPPED SHALE FRACTURE CONDUCTIVITY

3.1 Introduction

In a hydraulic fracture, several scenarios can lead to portions of the fracture not receiving proppant. The viscosity of the fracturing fluid may be insufficient to properly carry proppant throughout the vertical or horizontal extent of the fracture, resulting in proppant settling. Another possibility is that the selected proppant has a diameter greater than that of the fracture aperture, which is an especially common occurrence at the fracture tips. Although there exists the possibility that even a well thought-out fracturing treatment may result in an unpropped fracture, the goal is to design a stimulation treatment that results in fully-propped fractures. For that reason, this study only attempts to clarify propped fracture conductivity in the Marcellus shale.

3.2 Experimental Overview

Based on the information regarding fracture treatment schedules for the Marcellus shale (displayed in some detail previously in Table 1.2), samples were loaded at four different proppant levels that represented between 0.16 and 1.3 ppg. While the Marcellus shale is occasionally fractured using proppant concentrations up to 2.5 ppg, manual placement of such a large amount of proppant for experiments is difficult to do in a uniform fashion.

The Allenwood and Elimsport samples were primarily tested at different proppant loading levels. Initially, the Elimsport samples were the only samples obtained for this work, but testing rendered some samples unusable before full testing could be

completed, and it became clear that more samples would be required to finish this study. A second set of samples, excavated from the Allenwood location, was then purchased to complete this work. Table 3.1 summarizes all of the experimental permutations.

Table 3.1 – Test Permutations of Propped Fracture Conductivity

Proppant Mass	Areal Proppant Concentration	Simulated Proppant Concentration	Sample Sets	Number of Tests
0.4 g	0.013 lb/ft^2	0.16 ppg	Allenwood – Horizontal	5
			Allenwood – Vertical	5
0.8 g	0.025 lb/ft^2	0.33 ppg	Allenwood – Horizontal	5
			Allenwood – Vertical	5
1.6 g	0.051 lb/ft^2	0.65 ppg	Elimsport – Horizontal	5
			Elimsport – Vertical	5
			Allenwood – Horizontal	3
			Allenwood – Vertical	1
3.2 g	0.10 lb/ft^2	1.3 ppg	Elimsport – Horizontal	5
			Elimsport – Vertical	5

At each proppant loading level, at least five horizontal and vertical specimens were tested. To minimize fracture surface deformation of each sample, tests were conducted in order of the highest to the lowest proppant loading level. Decreasing proppant levels inside the fracture reduces the number of contact points between the fracture faces, thereby increasing the force transmitted through each grain of proppant and encouraging sample deformation as a result. Plastic deformation of the samples is an undesirable result, as this would reduce the comparability of each sample between proppant loading levels.

The areal concentration of proppant required to achieve a full monolayer can be determined mathematically, as derived by Brannon et al. (2004),

$$C_a = 5.20(1 - \phi)\gamma_p d_p \hspace{2cm} \text{(3-1)}$$

where C_a is the minimum areal concentration of proppant required to obtain a full monolayer, ϕ is the minimum porosity of the proppant pack, γ_p is the proppant specific gravity and d_p is the average proppant diameter. Using 40/70 natural white sand, a minimum porosity of 0.4, a γ_p of 2.65, and a d_p value of 0.0128 inches, the minimum areal concentration of proppant required to achieve a full monolayer is 0.10 lb/ft^2. While this suggests for the samples in this study that a full monolayer was only achieved at the highest proppant concentration, the surface contours made it impossible to obtain an even proppant layer thickness over the sample. Equation 3-1 assumes a surface that can accommodate an even distribution of proppant, which was not the case for this research, since some samples possessed significant roughness. While a partial monolayer was clearly observed at lower proppant loading, multiple layers of proppant were observed in

the depressions of some samples at a loading level of 1.6 and 3.2 grams. A similar

conclusion regarding the presence of multiple proppant layers at proppant concentrations

lower than that predicted by Brannon et al.'s model (2004) was drawn by Zhang (2014).

Table 3.2 shows samples loaded at each of the tested proppant concentrations. It

shows that the range of tested areal proppant concentrations represents at the low end a

partial monolayer, and at the high end a mixed system with areas devoid of proppant and

areas with a proppant multilayer. As the samples are naturally dark grey or black, the

white and beige coloration in Table 3.2 depicts the presence of proppant.

Table 3.2 – Depiction of Tested Proppant Loading

Areal Proppant Concentration	Horizontal	Vertical
0.013 lb/ft^2		
0.025 lb/ft^2		
0.051 lb/ft^2		
0.10 lb/ft^2		

3.3   Propped Fracture Conductivity of the Marcellus Shale

For this work, Allenwood samples were used to determine fracture conductivity at proppant loading levels of 0.013 lb/ft^2 and 0.025 lb/ft^2. Elimsport samples were used to determine fracture conductivity at proppant loading levels at 0.051 lb/ft^2 and 0.10 lb/ft^2. Several Allenwood samples were also tested at a proppant loading of 0.051 lb/ft^2 to compare the sample sets, as they displayed very different rock properties. Rock properties for the Allenwood and Elimsport samples are summarized in Table 3.3. Complete conductivity data sets for both the Elimsport and Allenwood samples are displayed numerically in Appendix A and graphically in Appendix B. The complete roughness data are included in Appendix C.

Table 3.3 – Summary of Allenwood and Elimsport Rock Properties

Property	Allenwood	Elimsport
E_v	$4.41 \times 10^6 \, psi$	$2.32 \times 10^6 \, psi$
E_h	$3.99 \times 10^6 \, psi$	$1.10 \times 10^6 \, psi$
ν_v	0.161	0.283
ν_h	0.202	0.256
$R_{RMS,v}$	$0.166 \, in$	$0.12 \, in$
$R_{RMS,h}$	$0.097 \, in$	$0.079 \, in$

While the absolute values of Young's Modulus, Poisson's Ratio, and surface roughness are important to consider, the anisotropy of these properties is also valuable. Table 3.4 attempts to illustrate how the Allenwood and Elimsport samples differ in terms of anisotropy.

Table 3.4 – Anisotropy between Horizontal and Vertical Property Values

	Property	Percent Difference $\left(\frac{max-min}{max} \times 100\right)$
Allenwood	E	9.5%
	ν	20.3%
	R_{RMS}	39.9%
Elimsport	E	52.6%
	ν	9.5%
	R_{RMS}	30.8%

The most beneficial way to display fracture conductivity is to plot it as a function of closure stress, as closure stresses can vary significantly in a formation as large as the Marcellus. Jansen (2014) proposed that the fracture conductivity as a function of closure stress can be described by,

$$c_f \cong c_{f0}e^{-\lambda\sigma_c}$$ ....(3-2)

Where c_{f0} is the unstressed fracture conductivity, λ is the curve's decline rate, and σ_c is the closure stress. For these experiments, at closure stresses between 1,000 and 3,000 psi, the decline in conductivity as a function of closure stress does not exhibit an exponential trend when conductivity is calculated using Darcy's Equation. The goodness-of-fit for an exponential trend is worse when calculating conductivity using Forchheimer's Equation, as shown in Fig. 2.22. Propped fracture conductivity values presented by Kamenov (2013), Briggs (2014) and Zhang (2014) also show similar behavior for some samples at these closure stresses.

All of the reported conductivity values in the following two sections are the averages of the individual sample conductivity values for the horizontal and vertical specimens tested at each proppant concentration. The vertical bars at each closure stress extend one standard deviation from the mean at that stress.

3.3.1 Allenwood Sample Fracture Conductivity

Fig. 3.1 shows the average fracture conductivity for the 10 tests run at 0.013 lb/ft^2 proppant, which simulates 0.16 ppg proppant concentration.
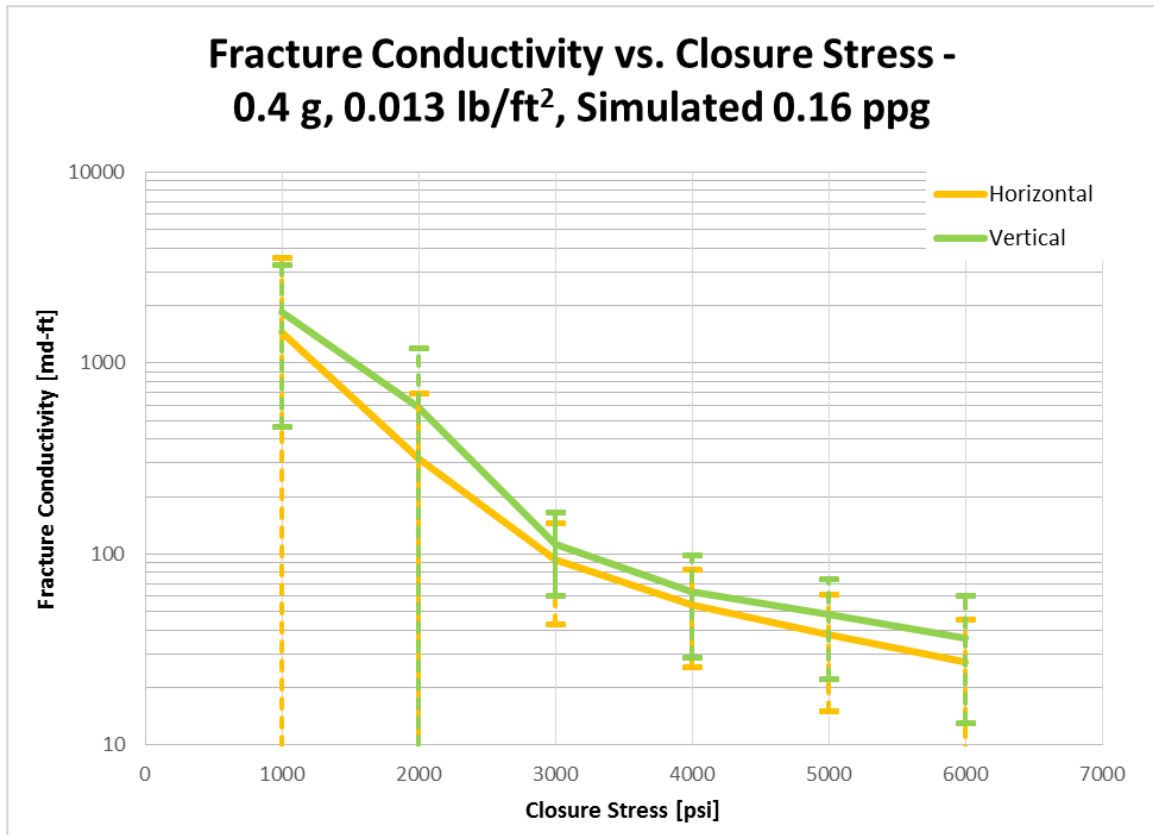
Fig. 3.1 – Average Fracture Conductivity and Standard Deviation with 0.013 lb/ft^2 Proppant

This proppant loading level is slightly lower than what most operators call for in their fracture treatment schedules, but may be indicative of fracture conductivity at the fracture tips, or in regions of the fracture that have received diminished levels of proppant as compared to the called-for treatment concentration. At this low level of proppant loading, there is a very slight difference between the average conductivity of the horizontal and vertical specimens. Vertical fracture conductivity at this proppant

loading level is slightly better than horizontal fracture conductivity, and decline rates for the two curves are very similar.

Doubling proppant loading from 0.013 lb/ft^2 to 0.025lb/ft^2 results in two nearly-identical curves, seen below in Fig. 3.2. Proppant loading of 0.025lb/ft^2 represents a simulated 0.33 ppg fracture treatment. Again, the decline rates between horizontally and vertically-fracture specimens are very similar at this proppant loading level, suggesting that for Allenwood samples, the fracture orientation does not play a significant role in the development of fracture conductivity.
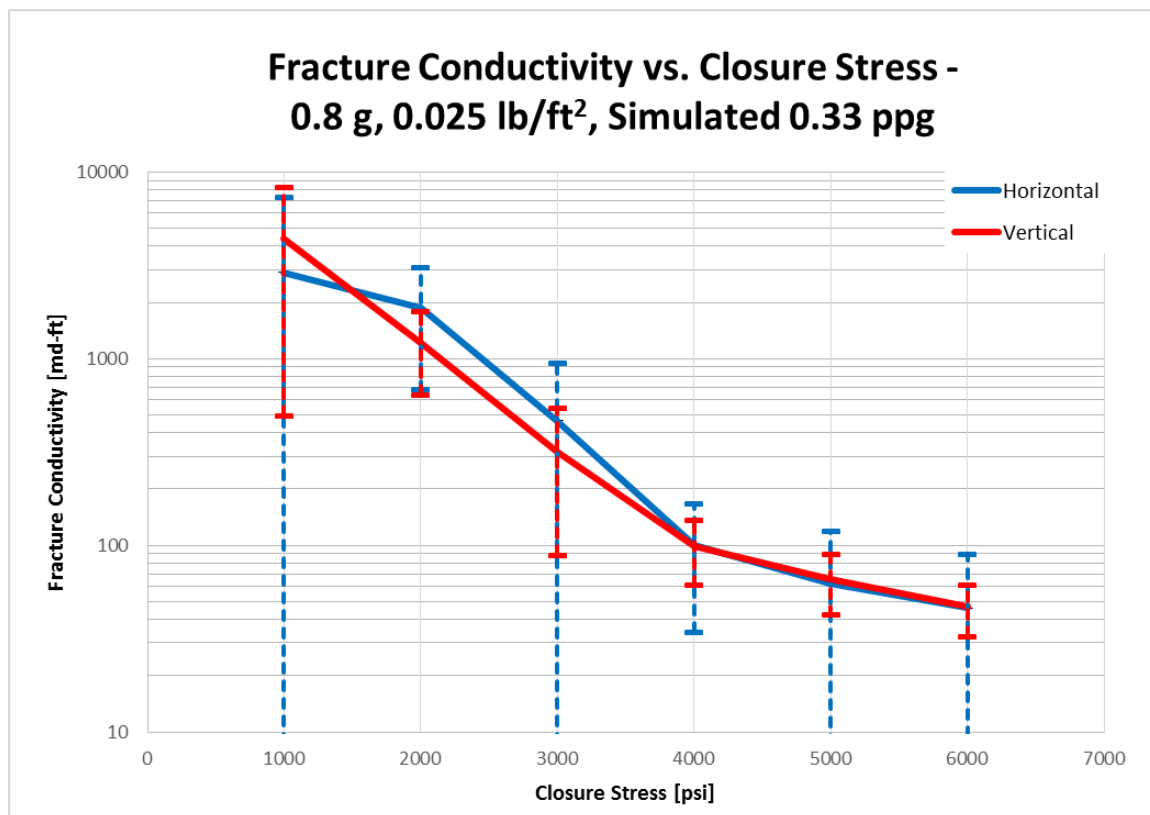
Fig. 3.2 – Average Fracture Conductivity and Standard Deviation with 0.025 lb/ft^2 Proppant

Allenwood samples were also tested at a concentration of 0.051 lb/ft^2 proppant to compare Elimsport and Allenwood samples at a common proppant concentration. The fracture conductivity results of the Allenwood samples run with 0.051 lb/ft^2 proppant as well as the results from the two previous figures are shown in Fig. 3.3. This figure clearly demonstrates three things at all tested proppant loading levels: the fracture conductivity of Allenwood samples is independent of fracture orientation, increasing proppant levels increases conductivity at realistic closure stresses, and conductivity decreases with increasing closure stress. Interestingly, the samples loaded with 0.051 lb/ft^2 proppant did not show the highest fracture conductivity at low closure stresses, but the large standard deviations at these closure stresses negate the statistical significance.
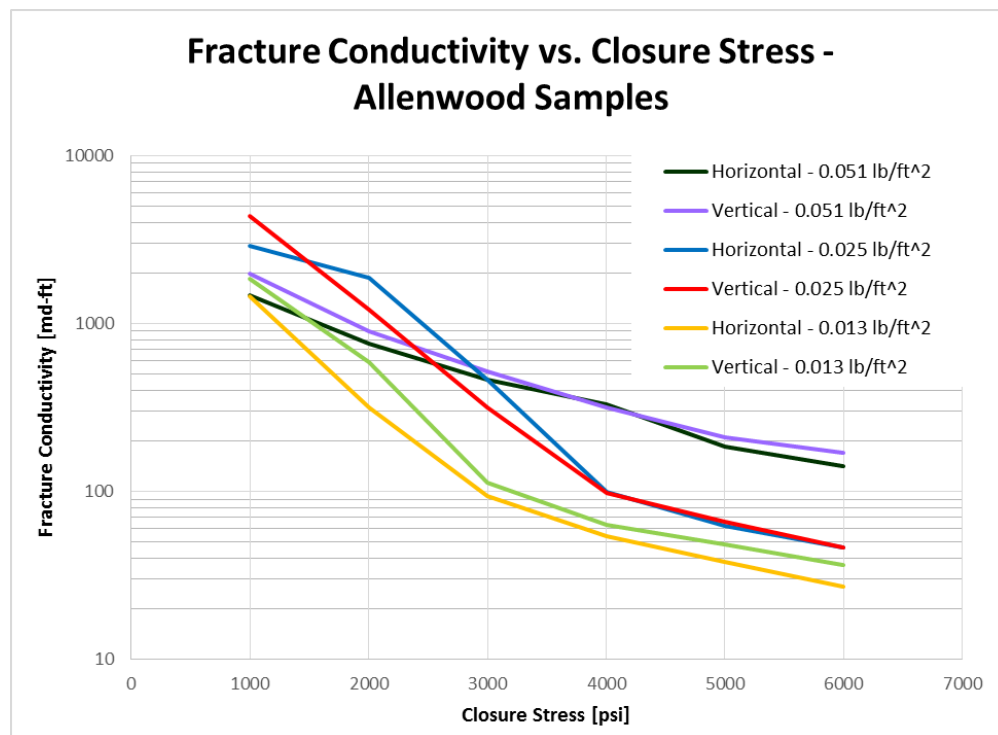
Fig. 3.3 – Summary of Allenwood Fracture Conductivity

3.3.2 Elimsport Sample Fracture Conductivity

Elimsport samples were loaded with 0.051 lb/ft^2 and 0.10 lb/ft^2 of proppant, which represent fracture treatments of 0.65 and 1.3 ppg proppant concentration. These samples displayed very different properties than the Allenwood samples; anisotropy is far more pronounced, but surface roughness is slightly lower. According to Kamenov (2013), who tested the propped fracture conductivity of the Barnett shale, higher surface roughness yields higher fracture conductivity. Fig. 3.4 depicts fracture conductivity for 10 Allenwood samples at 0.051 lb/ft^2 proppant, which simulates 0.65 ppg.
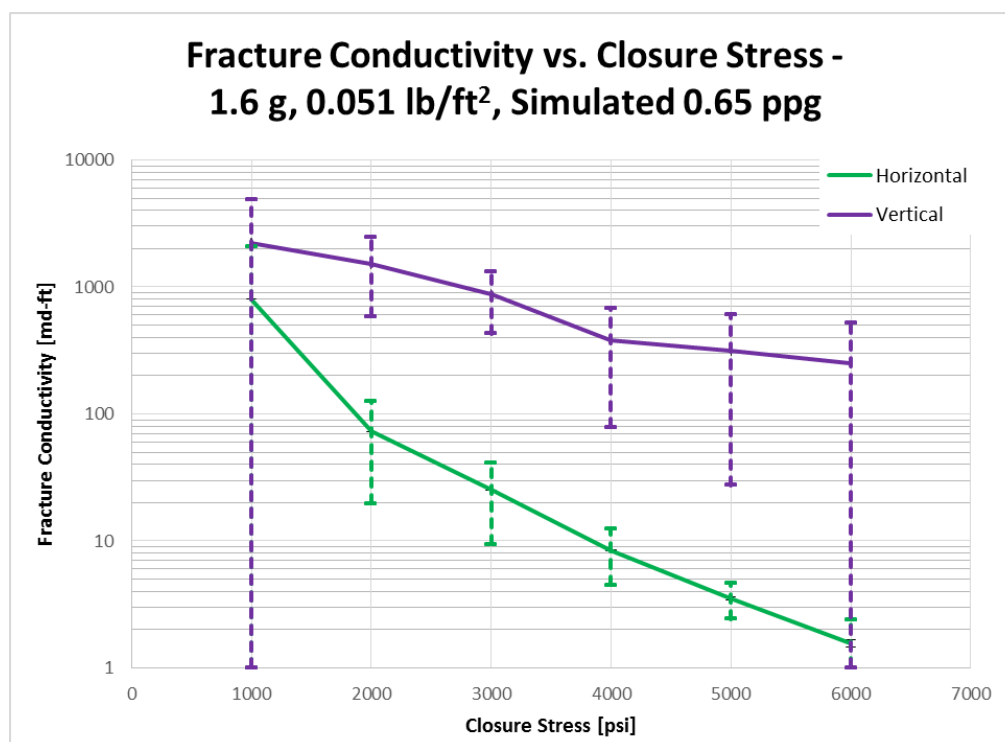
Fig. 3.4 – Average Fracture Conductivity and Standard Deviation with 0.051 lb/ft^2 Proppant

87

These results are a great departure from all three sets of Allenwood sample conductivity results. Not only do the horizontal and vertical specimens possess drastically different conductivity values at each closure stress, but the decline rates for these curves are also different. While the Allenwood samples experienced similar decline rates and had similar values for Young's Modulus in the horizontal and vertical orientation, these samples exhibit drastically different Young's Moduli. Observationally, the decline rate of these curves, λ, is likely related to Young's Modulus, which is supported by Jansen et al. (2015). Finally, the vertically-fractured samples, which had a Young's Modulus almost double that of the horizontally-fractured samples, had a higher conductivity value at every measured closure stress.

That Young's Modulus is directly related to fracture conductivity is no surprise. For many years, brittleness has been identified as a key parameter in determining how favorable a particular zone is for fracturing. The Brittleness Index is defined by Rickman et al. (2008) as,

$$BI = \frac{E_B + \nu_B}{2} \quad \text{..} (3\text{-}3)$$

$$E_B = \frac{E - E_{ductile}}{E_{brittle} - E_{ductile}} \times 100 \quad \text{..} (3\text{-}4)$$

$$\nu_B = \frac{\nu - \nu_{ductile}}{\nu_{brittle} - \nu_{ductile}} \times 100 \quad \text{..} (3\text{-}5)$$

where the ductile and brittle subscripts denote a chosen maximum and minimum value (within the context of the formation) for Young's Modulus and Poisson's Ratio. A greater Brittleness Index indicates a zone more favorable for fracturing.

Increasing proppant loading from 0.051 lb/ft^2 to 0.10 lb/ft^2 results in Fig. 3.5. Again, the conductivity of vertically-fractured samples is significantly higher than that of the horizontally-fractured specimens, although the difference is muted when compared to the tests run with 0.051 lb/ft^2 proppant. Perhaps this is the result of the increasing role that proppant's mechanical properties play in fracture conductivity at higher proppant loading values.
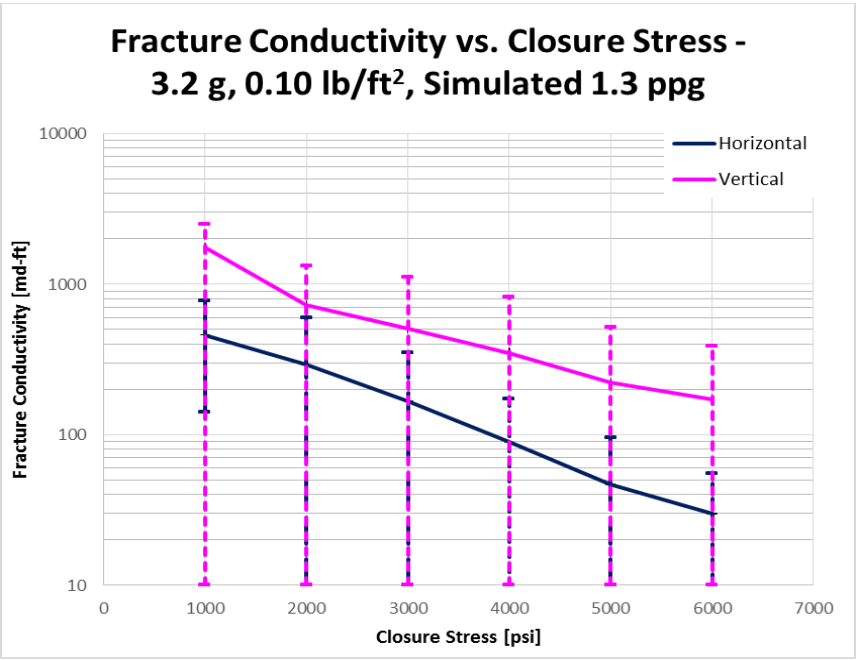
Fig. 3.5 – Average Fracture Conductivity and Standard Deviation with 0.10 lb/ft^2 Proppant

For the first time, the standard deviation from the mean indicates extreme variation in the conductivity of each sample at every closure stress. This is also a somewhat-expected result. Even testing the conductivity of proppant packs to the ISO standard for long-term conductivity can result in significant scatter in data, as shown in Fig. 3.6. Recalling that the ISO standard for long-term conductivity uses sawn sandstone surface for its fractured material, the results from the ISO standard should be far more consistent than the results for these tests, which use a rough fracture for the fracture surface. Even with fracture roughness removed as a variable, fracture conductivity in Fig. 3.6 varies between 700 and 2,000 md-ft at 6,000 psi closure stress.
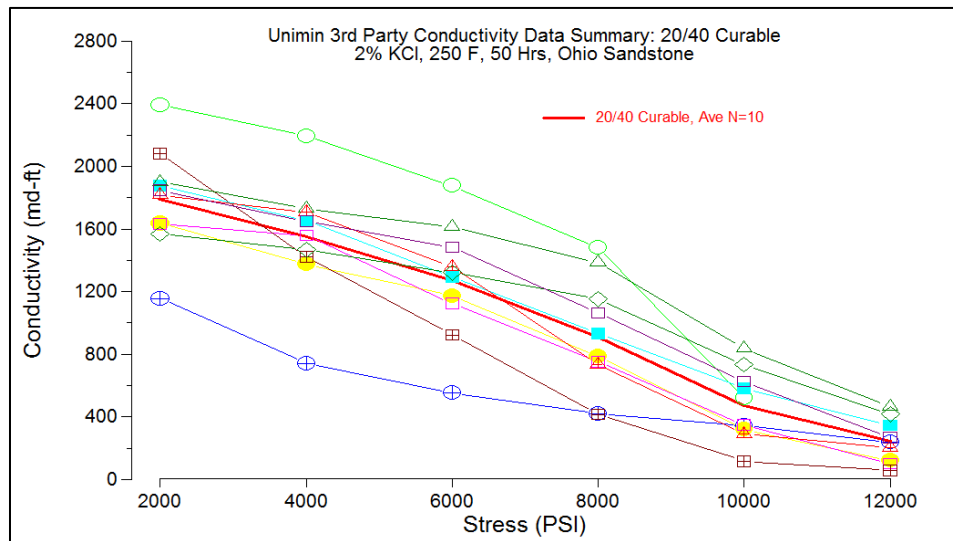
Fig. 3.6 – Long-term Conductivity Results for 20/40 Resin-Coated Proppant (Jackson, 2014)

All of the conductivity tests on Elimsport samples are summarized below in Fig. 3.7. Several observations can be made from both sets of data: increasing levels of proppant appear to decrease the difference in fracture conductivity for vertically and horizontally-fractured samples, and doubling the amount of proppant from 0.051 to 0.10 lb/ft^2 does not make a significant difference in fracture conductivity for the vertically-fractured samples. This may be indicative of the diminishing returns on conductivity after a full monolayer of proppant has been established.
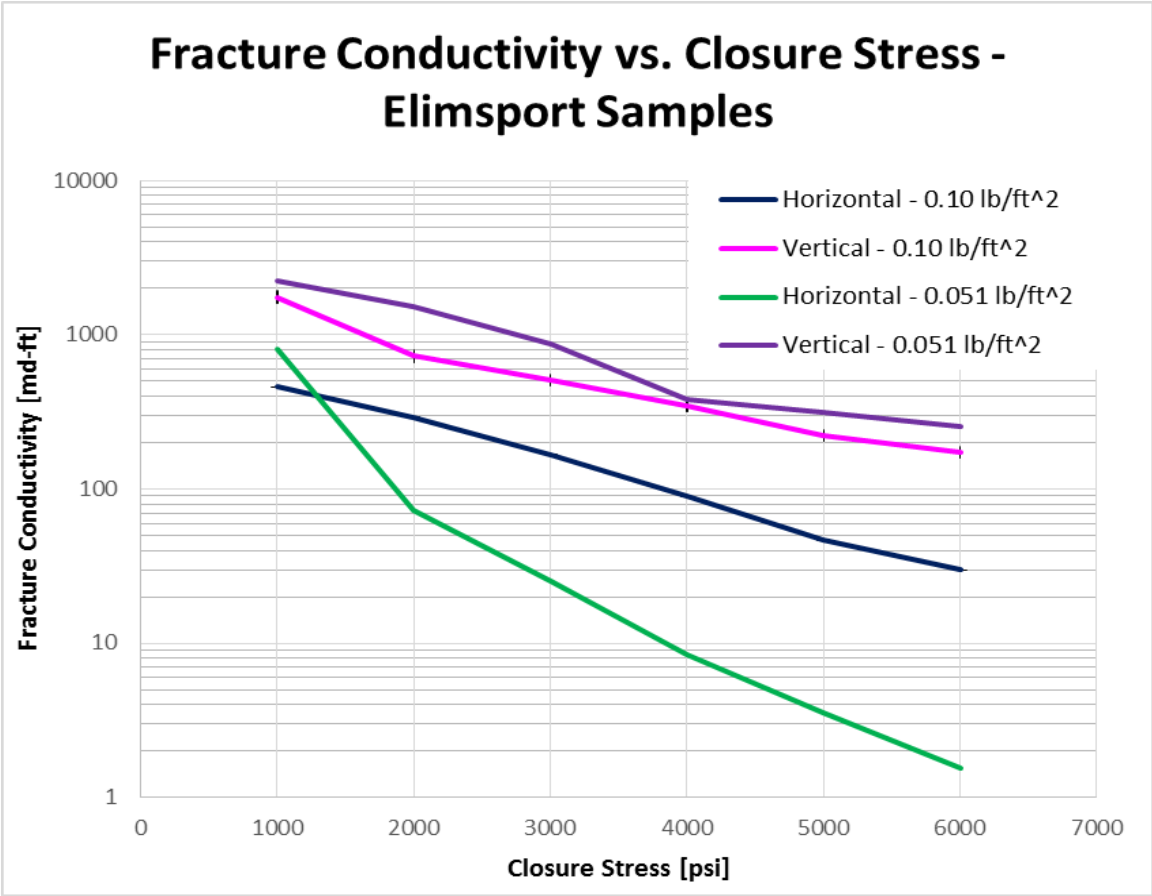
Fig. 3.7 – Summary of Elimsport Fracture Conductivity

3.3.3 Comparison of Allenwood and Elimsport Fracture Conductivity

Fig. 3.8 shows a comparison of Allenwood and Elimsport sample fracture conductivity values at 0.051 lb/ft^2 proppant. From this graph, it is clear that fracture conductivity is extremely orientation-sensitive for the Elimsport samples, but not at all orientation-sensitive for the Allenwood samples. Why?
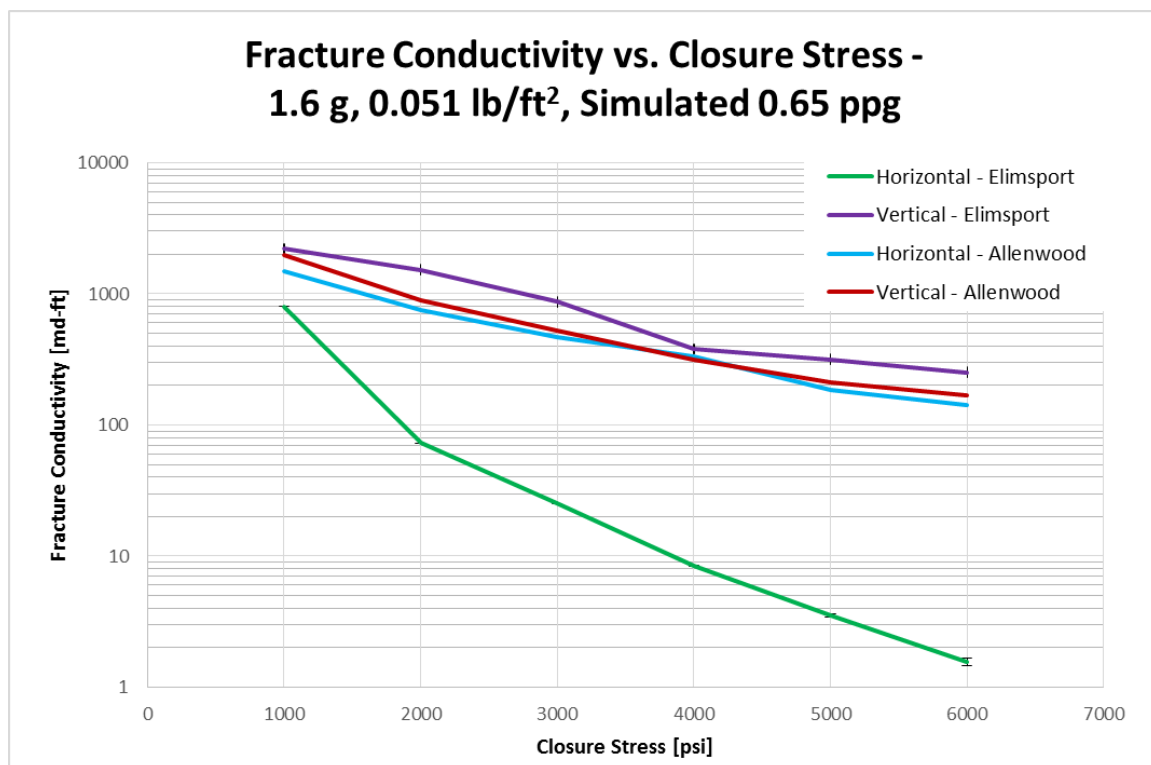
Fig. 3.8 – Elimsport and Allenwood Fracture Conductivity with 0.051 lb/ft^2 Proppant

If the fracture surface roughness plays a significant role in the development of fracture conductivity, there should be a significant gap between the vertically-fractured

Allenwood samples and the remaining three sample sets, as the vertically-fractured

Allenwood samples have significantly greater surface roughness. If the orientation of

the fracture itself plays a significant role in the development of fracture conductivity,

then qualitatively there should be similar differences between the horizontally and

vertically-fractured specimens for the Allenwood and Elimsport samples, but that is

simply not the case.

One final observation is that, despite the significant difference in the Young's

Moduli between both Allenwood samples and the vertically-fractured Elimsport

samples, they exhibit very similar fracture conductivity trends. This suggests that c_{f0} is

dependent on factors other than elastic rock properties. Observationally, perhaps this is

a factor of both fracture orientation and the ratio of Young's Modulus between the

horizontal and vertical orientations.

4 FRACTURE CONDUCTIVITY AS A FUNCTION OF ROCK MECHANICAL PROPERTIES

4.1 Introduction

One way to account for the differences in conductivity between the horizontal and vertical specimens is to examine mechanical properties of these specimens - specifically their anisotropy. Both the Elimsport and Allenwood samples are assumed to be transversely isotropic. A transversely isotropic material like sedimentary rock is one that exhibits mechanical properties that are identical within a plane (in this case, bedding planes) but where properties are not identical in the through-thickness direction. For this study, both Young's Modulus and Poisson's Ratio were assumed to be equal in the x and y direction, but not in the z. Cores cut for triaxial testing of rock mechanical properties are shown in illustrated form in Fig. 4.1. Anisotropy was established in varying degrees in both the Elimsport and Allenwood samples, although the greater anisotropy was exhibited in the Elimsport samples. In a transversely isotropic sample,

$$E_x = E_y = E_h \neq E_z = E_v \quad \text{..(4-1)}$$

$$\nu_x = \nu_y = \nu_h \neq \nu_z = \nu_v \quad \text{..(4-2)}$$
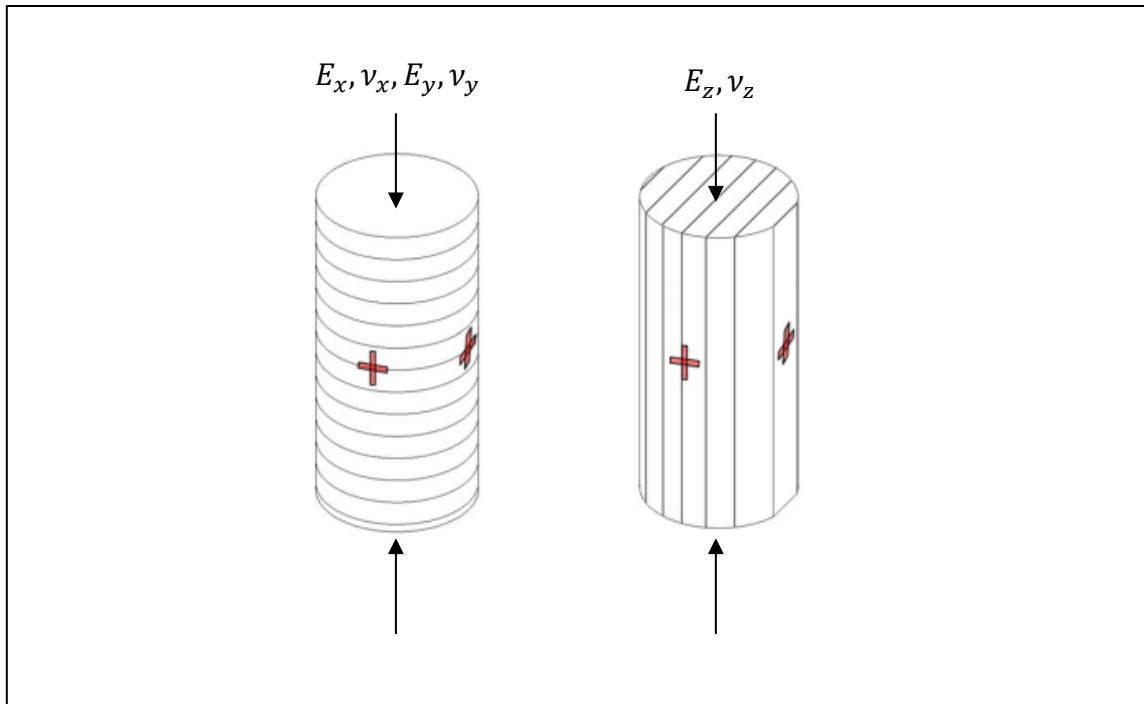
Fig. 4.1 – Schematic of Rock Mechanical Property Anisotropy in Triaxial Testing
(adapted from Cho et al., 2011)

The difference between the values of Young's Modulus and Poisson's Ratio in the

horizontal and vertical orientation help quantify how anisotropic the samples are.

Defining an anisotropy ratio for the Elimsport and Allenwood samples as,

$$C' = 0.5\left(\frac{E_{max}}{E_{min}} + \frac{\nu_{max}}{\nu_{min}}\right) \dots\dots\dots\dots\dots\dots\dots\dots\dots\dots\dots\dots\dots\dots\dots\dots(4\text{-}3)$$

the Elimsport anisotropy ratio is 1.61 and Allenwood anisotropy ratio is 1.18. As

fracture surface roughness is largely a characteristic of the rock's mechanical properties,

it is not included in the calculation of an anisotropy ratio. An anisotropy ratio near one

indicates that the sample is roughly isotropic; a value significantly greater than one

indicates anisotropy. While the anisotropy of Young's Modulus and Poisson's Ratio has

95

already been linked to differences in fracture conductivity, it must first be linked to fracture mechanics in order to determine if rock properties are causal in developing fracture conductivity, or if this is a spurious correlation.

Surface contour scans of horizontally and vertically-fractured samples from both outcrops are shown in Figs. 4.2 – 4.5. The surface characteristics of these four samples show stark differences, with the Elimsport samples being far smoother both in terms of R_{RMS} and their 3-D contours. The remaining surface profile scans are included as part of Appendix C.
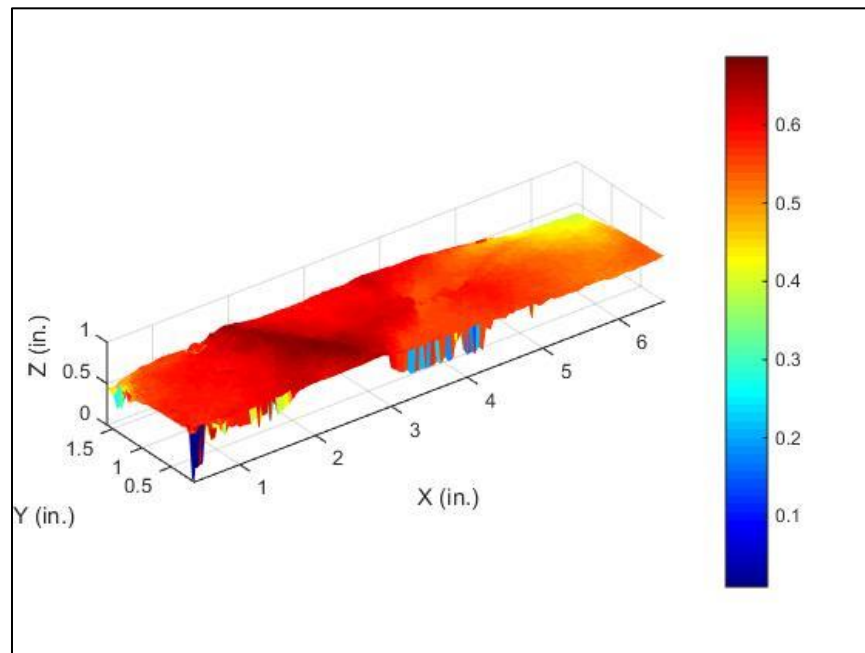

Fig. 4.2 – Surface Contours of 04RXTH, Horizontally-Fractured Elimsport Sample
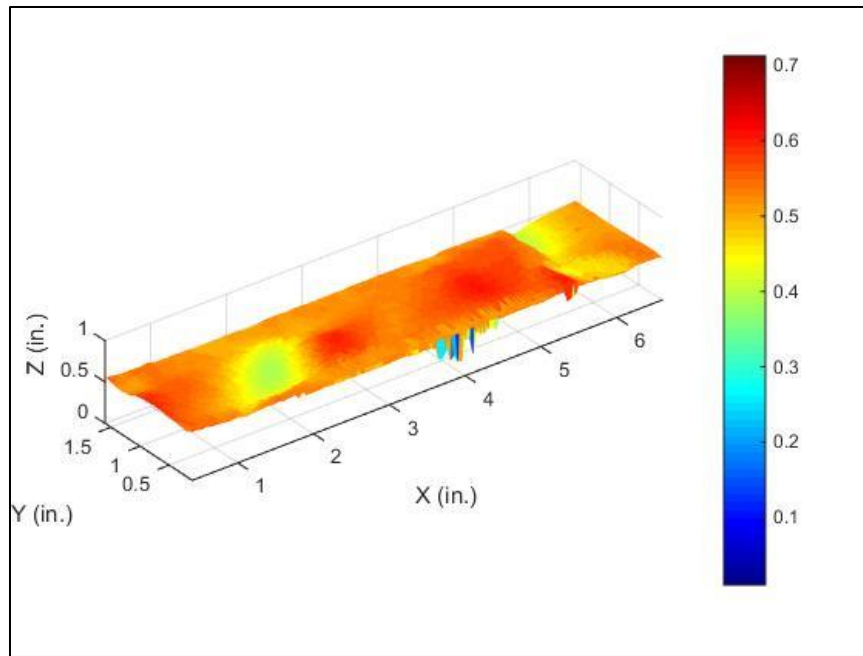
Fig. 4.3 – Surface Contours of 10RXTV, Vertically-Fractured Elimsport Sample
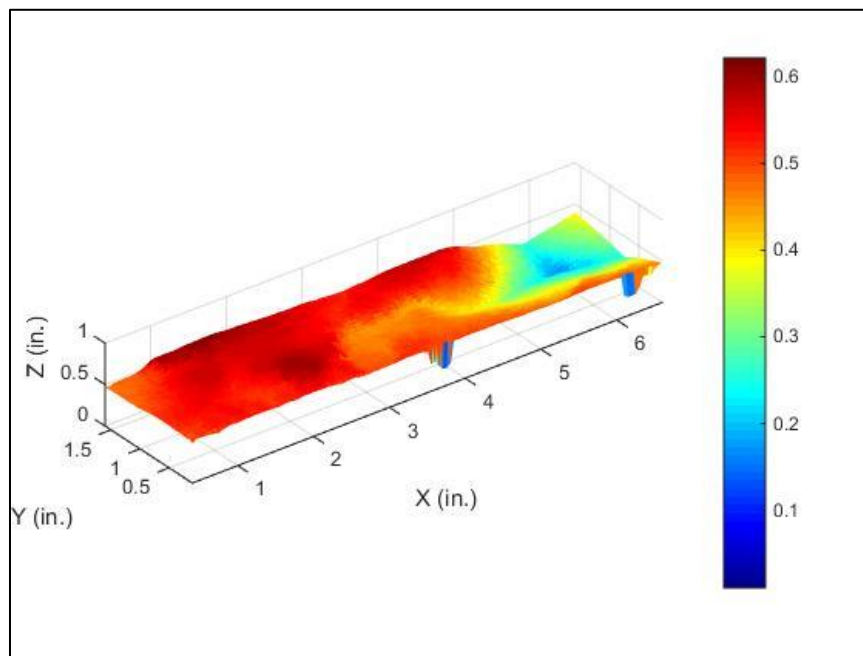
Fig. 4.4 – Surface Contours of 19RNTH, Horizontally-Fractured Allenwood Sample
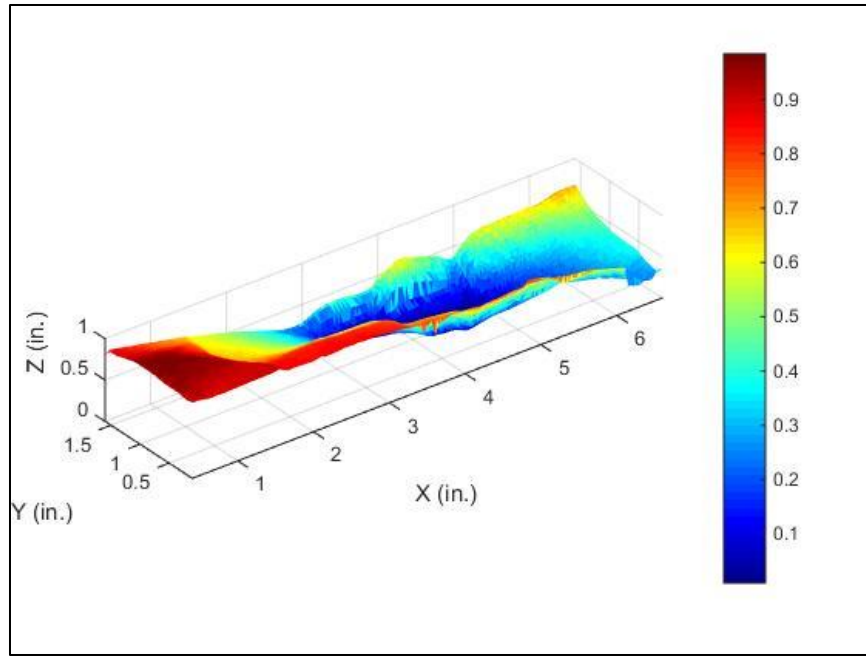
Fig. 4.5 – Surface Contours of 16RNTV, Vertically-Fractured Allenwood Sample

Tavallali and Vervoort (2010) investigated the effect of layer orientation on fracture mechanics in sandstone and describe three main fracture modes: layer activation, central fracture, and non-central fracture. In layer activation, the fracture occurs in a plane of transverse isotropy. In a central fracture, the fracture propagates predominantly parallel to the loading direction, irrespective of the plane of transverse isotropy. A non-central fracture describes a fracture that propagates more than 10° off-axis from the loading direction. Both horizontally and vertically-fractured samples from this study are shown in Fig 4.6. It shows that the vertical and nearly vertical fractures are more complex and interconnected than the horizontal or nearly horizontal fractures.
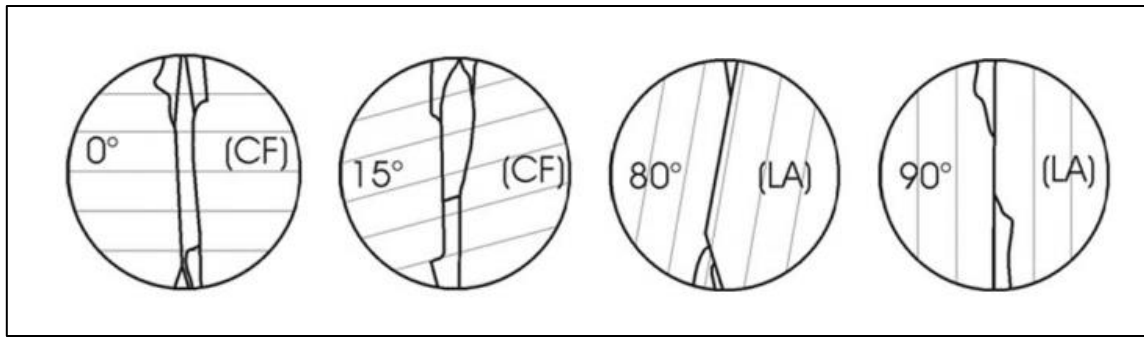
Fig**.** 4.6 – Fracture Schematic of Vertical (0° and 15°) and Horizontal (80° and 90°) Fractures (Tavallali and Vervoort, 2010)

From the above figure, it appears as though both of the vertical fractures would experience significant spalling of the fracture face, whereas the horizontal fractures would result in a relatively clean and planar fracture. Tavallali and Vervoort also quantified the total fracture length for the various fracture orientations in their samples, shown in Table 4.1. Total fracture length as exhibited in Table 4.1 describes the total length of all fractures over a 50 mm diameter Brazilian test disc. For example, a sample with two full-length fractures across the test disc would have a listed total fracture length of roughly 100 mm. While Young's Modulus and Poisson's Ratio were not discussed, the anisotropy of the samples is apparent through the differences in Brazilian Tensile Strength (BTS).

Table 4.1 – Total Fracture Length as a Function of Sample Orientation (adapted from Tavallali and Vervoort, 2010)

Sample Orientation	Average Total Fracture Length	Average Brazilian Tensile Strength
Vertical (0° and 15°)	137.4 mm	2,097 psi
Horizontal (80° and 90°)	101.7 mm	1,448 psi

Although Tavallali and Vervoort's work used layered sandstone samples, other research has shown similar results using shale samples. Fig. 4.7 shows how cores of Boryeong shale, found in South Korea, fractured under varying fracture orientation angles.

Vertical

Fracture

Horizontal

Fracture
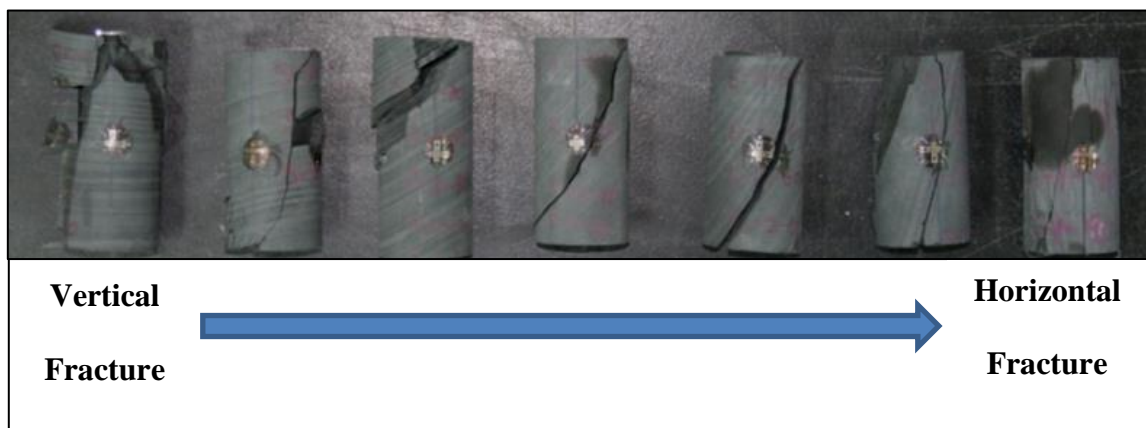
Fig. 4.7 – Boryeong Shale Specimens after Failure in Uniaxial Compression Tests (Cho et al., 2011)

Both Tavallali and Vervoort, and Cho et al.'s work was mainly constructed from experimental results. A third study by Liu et al. (2013) matched results from Cho et al. to numerical simulation results. It clearly shows that when the fracture-initiating load was aligned with the plane of transverse isotropy, the fracture cleanly cleaved through that plane. When the crack propagated orthogonally to the bedding planes, as would occur in a vertical fracture, the fracture appeared to be more tortuous. Those results are shown in Fig. 4.8.

Fig. 4.8 – Fracture Propagation Path through Vertical and Horizontal Fractures (adapted from Liu et al., 2013)

Interestingly, other research has indicated that the fracture form is highly dependent on confining stress. Misbahi et al. (1995) suggested that the propagation of a

crack along a plane of transverse isotropy is dependent on confining stress, where at a confining stress of less than roughly 3,000 psi, the fracture is bound to propagate along bedding planes. Above 3,000 psi, Misbahi did not find this to be always true.

4.2   Mechanical Property Anisotropy

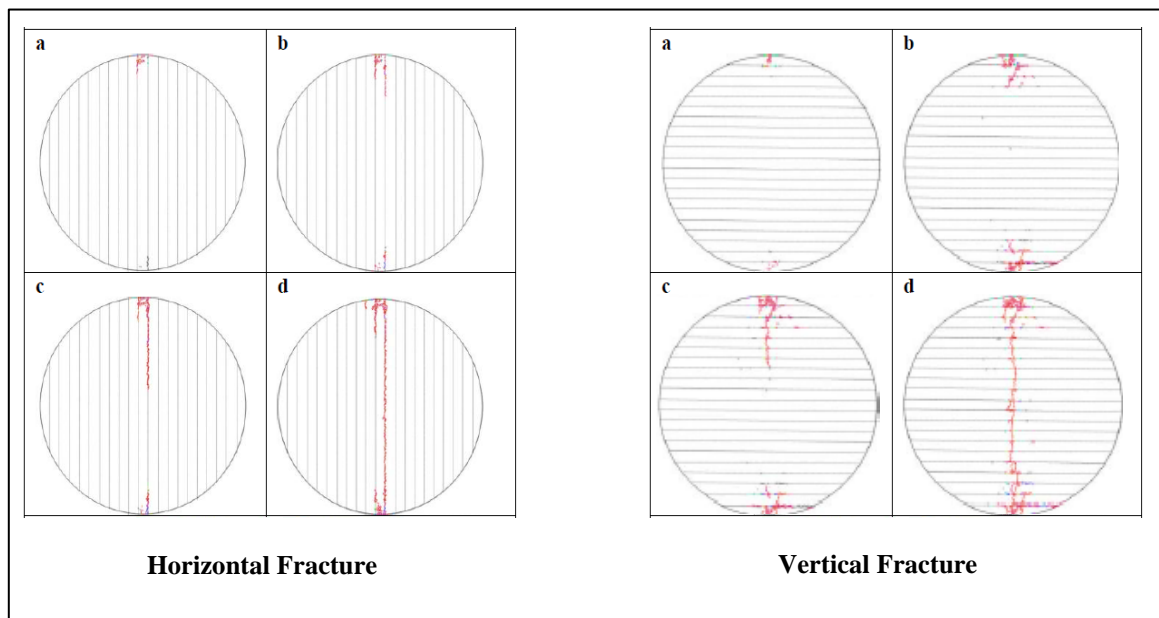As discussed previously, fracture conductivity of the tested Marcellus shale samples is not a function of either fracture surface roughness or fracture orientation. Conductivity is very similar in two sets of samples with significantly different surface roughness values. Fracture orientation also appears to not be the cause of fracture conductivity development. In the Allenwood samples, the two fracture orientations demonstrate very similar conductivity values. The best explanation for differences in conductivity is the rock mechanical properties.

The Allenwood samples have relatively little anisotropy; their overall anisotropy ratio is 1.18, and the Young's Modulus only varies by 9.5% between the two fracture orientations. For three tested proppant loading levels, the conductivity difference between horizontally and vertically-fractured samples is negligible. On the other hand, the Elimsport samples have an overall anisotropy ratio of 1.6, and the Young's Modulus varies by 53% between the two fracture orientations. These samples have extremely different conductivity values throughout the range of tested closure stresses.

Although it would be appealing to suggest that the fracture conductivity is purely related to the rock's mechanical properties, there is obviously something else afoot. The vertically-fractured Allenwood and Elimsport samples have very similar conductivity

values when tested with 1.6 g proppant, despite having significant differences in their

Young's Modulus and Poisson's Ratio, suggesting that perhaps both the absolute value

of mechanical properties and the anisotropy of mechanical properties impact fracture

conductivity.

5   CONCLUSIONS AND RECOMMENDATIONS

5.1   Conclusions

This thesis presents a thorough study of propped fracture conductivity in the Marcellus shale. The conclusions of this work are summarized below:

(1) Laboratory procedures used for this work can be used to measure fracture conductivity with gas in a reproducible, consistent way. Although this study used nitrogen gas in lieu of fracturing fluid, Zhang (2014) and Awoleke (2013) used multiple fluids for their work; very few modifications to the described procedure are required to run tests with a liquid or slurry.

(2) Based on XRD data, both the Allenwood and Elimsport samples are representative of hydrocarbon-bearing Marcellus shale.

(3) Propped fracture conductivity as a function of closure stress experiences exponential decay. Observationally, Young's Modulus appears to affect the value of the decline rate constant, λ, described by Jansen et al. (2015). Additionally, the value of c_{f0} is dependent on factors other than elastic rock properties; perhaps anisotropy plays a role in the development of non-stressed fracture conductivity as suggested by fracture mechanics.

(4) The propped fracture conductivity of the Marcellus shale is not a dependent on either fracture orientation or fracture surface roughness.

(5) The differences in fracture conductivity can be accounted for through anisotropy of mechanical properties such as Young's Modulus and Poisson's Ratio.

(6) In propped fractures, fracture conductivity trends cannot be exclusively described via rock mechanical properties, as evidenced by the vertically-fractured Elimsport and Allenwood samples, which had very different Young's Moduli and Poisson's Ratios but similar conductivity behavior.

5.2   Limitations and Recommendations

To extend the scope of this work, or to increase its applicability to other formations, more work is needed. Limitations of this work include:

(1) Laboratory tests for this work were all run at room temperature and in the absence of liquid, which has significant impacts on fracture conductivity, as shale is sensitive to water imbibition.

(2) Proppant was placed manually into the fractures for this experiment since gas was the stand-in for fracturing fluid. Dynamic proppant placement would be more representative of field conditions, and would also eliminate the need for estimating fracture width in order to convert proppant concentration to a proppant loading level for each test.

(3) All tests were conducted with proppant; a more thorough study might test unpropped fracture conductivity to eliminate the variables introduced by the use of proppant.

REFERENCES

Awoleke, O.O. 2013.. Dynamic Fracture Conductivity – An Experimental Investigation based on Factorial Analysis. Ph.D. Dissertation. Texas A&M University, College Station, Texas, U.S.A. (May 2013)

Awoleke, O., Romero, J., Zhu, D., and Hill, A.D.. 2012. Experimental Investigation of Propped Fracture Conductivity in Tight Gas Reservoirs Using Factorial Design. SPE Paper 151963. Presented at the SPE Hydraulic Fracturing Technology Conference, the Woodlands, Texas, U.S.A. 6-8 February.

Boyce, M. L., and Carr, T. R.. 2009. Lithostratigraphy and Petrophysics of the Devonian Marcellus Interval in West Virginia and Southwestern Pennsylvania. Conference Proceeding. Presented at the GCSSEPM Foundation Bob F. Perkins Research Conference, Houston, Texas, U.S.A., 6-8 December.

Boyer, J., Maley, D., and O'Neill, B.. 2014. Chemically Enhanced Proppant Transport. SPE Paper 170640. Presented at SPE Annual Technical Conference and Exhibition, Amsterdam, The Netherlands, 27-29 October.

Brannon, H.D., Malone, M.R., Rickards, A.R., Wood, W.D., Edgeman, J.R., and Bryant, J.L. 2004. Maximizing Fracture Conductivity with Proppant Partial Monolayers: Theoretical Curiosity or Highly Productive Reality? SPE Paper 90698. Presented at the SPE Annual Technical Conference and Exhibition, Houston, Texas, U.S.A., 26-29 September.

Brannon, H.D., and Pearson, C.M.. "Proppants and Fracture Conductivity" in *Modern Fracturing – Enhancing Natural Gas Production*. M.J. Economides and T. Martin, eds., Chap. 8, Energy Tribune Publishing, 2007.

Briggs, K. E. 2014. The Influence of Vertical Location on Hydraulic Fracture Conductivity in the Fayetteville Shale. M.S. Thesis, Texas A&M University, College Station, Texas (May 2014).

Chen, C., Pan, E., and Amadei, B.. 1996. Evaluation of Properties of Anisotropic Rocks Using Brazilian Tests. ARMA Paper 96-1651.

Cho, J., Kim, H., Jeon, S., and Min, K.. 2011. Deformation and Strength Anisotropy of Asan Gneiss, Boryeong Shale, and Yeoncheon Schist. *International Journal of Rock Mechanics and Mining Sciences* 50(2): 158-169.

Cinco-Ley, H., and Samaniego, F.. 1981. Transient Pressure Analysis for Fractured Wells. *Journal of Petroleum Technology* 33(9): 1749-1766.

Clark, J.B. 1949. A Hydraulic Process for Increasing the Productivity of Wells. SPE Paper 949001.

Dahi-Taleghani, A., and Olson, J.E.. 2009. Numerical Modeling of Multi-Stranded Hydraulic Fracture Propagation: Accounting for the Interaction Between Induced and Natural Fractures. SPE Paper 124884. Presented at the SPE Annual Technical Conference and Exhibition, New Orleans, Louisiana, U.S.A.. 4-7 October.

Darin, S.R., and Huitt, J.L. 1960. Effect of a Partial Monolayer of Proppant Agent on Fracture Flow Capacity. SPE Paper 1291. Presented at the Annual Fall Meeting, Dallas, Texas, U.S.A., 4-7 October.

Economides, M.J., Hill, A.D., Ehlig-Economides, C., and Zhu, D., *Petroleum Production Systems* (Upper Saddle River, N.J.: Prentice Hall, 2013), 612.

Engelder, T., Lash, G. G., and Uzcategui, R. S.. 2009. Joint Sets that Enhance Production from Middle and Upper Devonian Gas Shales of the Appalachian Basin. *AAPG Bulletin* 93(7): 857-889.

Fisher, M.K., Heinze, J.R., Harris, C.D., Davidson, B.M., Wright, C.A., and Dunn, K.P. 2004. Optimizing Horizontal Completion Techniques in the Barnett Shale Using Microseismic Fracture Mapping. SPE Paper 90051. Presented at the SPE Annual Technical Conference and Exhibition, Houston, Texas, U.S.A. 26-29 September.

Fredd, C.N., McConnell, S.B., Boney, C.L., and England, K.W.. 2001. Experimental Study of Fracture Conductivity for Water-Fracturing and Conventional Fracturing Applications. SPE Paper 74138. Presented at the SPE Rocky Mountain Region/Low Permeability Reservoirs Symposium and Exhibition, Denver, Colorado, U.S.A.. 12-15 March.

Gao, Y., Lv, Y., Wang, M., and Li, K.. 2012. New Mathematical Models for Calculating the Proppant Embedment and Fracture Conductivity. SPE Paper 155954. Presented at the SPE Annual Technical Conference and Exhibition, San Antonio, Texas, U.S.A., 8-10 October.

Guo, Q., Ji, L., Rajabov, V., Friedheim, J., and Wu, R.. 2012. Marcellus and Haynesville Drilling Data: Analysis and Lessons Learned. SPE Paper 158894. Presented at the SPE Asia Pacific Oil and Gas Conference and Exhibition, Perth, Australia, 22-24 October.

Guzek, J.J. 2014. Fracture Conductivity of the Eagle Ford Shale. M.S. Thesis, Texas A&M University, College Station, Texas (August 2014).

Houston, N., Blauch, M., Weaver, D., Miller, D.S., and O'Hara, D.. 2009. Fracture-Stimulation in the Marcellus Shale – Lessons Learned in Fluid Selection and Execution. SPE Paper 125987. Presented at the SPE Eastern Regional Meeting, Charleston, West Virginia, U.S.A.. 23-25 September.

ISO 13503-5. 2006. Petroleum and Natural Gas Industries-Completion Fluids and Materials- Part 5: Procedures for Measuring the Long-Term Conductivity of Proppants. First Edition, 1 July.

Izadi, G., Junca, J., and Cade, R.. 2014. Multidisciplinary Study of Hydraulic Fracturing in the Marcellus Shale. ARMA Paper 14-6975. Presented at the 48th US Rock Mechanics/Geomechanics Symposium, Minneapolis, Minnesota, U.S.A.. 1-4 June 2014.

Jackson, J. 2014. "Unimin Energy Solutions." Presentation at the SPE Texas A&M University Student Chapter Meeting, College Station, Texas, U.S.A.

Jansen, T.A. 2014. The Effect of Rock Properties on Hydraulic Fracture Conductivity in the Eagle Ford and Fayetteville Shales. M.S. Thesis, Texas A&M University, College Station, Texas (August 2014).

Jansen, T.A., Zhu, D., and Hill, A.D.. 2015. The Effect of Rock Mechanical Properties on Fracture Conductivity for Shale Formations. SPE Paper 173347. Presented at the SPE Hydraulic Fracturing Technology Conference, The Woodlands, Texas, U.S.A. 3-5 February.

Johri, M. 2012. Fault Damage Zones – Observations, Dynamic Modeling, and Implications on Fluid Flow. Ph.D. Dissertation, Stanford University, Palo Alto, California (December 2012).

Kamenov, A.N. 2013. The Effect of Proppant Size and Concentration on Hydraulic Fracture Conductivity in Shale Reservoirs. M.S. Thesis, Texas A&M University, College Station, Texas (May 2013).

Lash, G.G., and Engelder, T.. 2011. Thickness Trends and Sequence Stratigraphy of the Middle Devonian Marcellus Formation, Appalachian Basin: Implications for Acadian Foreland Basin Evolution. *AAPG Bulletin* 95(1): 61-103.

Liu, W.C., Tien, Y.M., Juang, C.H., and Lin, J.S.. 2013. Numerical Investigation of Crack Propagation and Failure Mechanism of Layered Rocks. ARMA Paper 2013-673. Presented at the 47th U.S. Rock Mechanics/Geomechanics Symposium, San Francisco, California, U.SA.. 23-26 June.

Mashayekhi, A., Belyadi, F., Aminian, K., and Ameri, S.. 2014. Predicting Production Behavior of the Marcellus Shale. SPE Paper 171002. Presented at SPE Eastern Regional Meeting, Charleston, West Virginia, U.S.A.. 21-23 October.

Mayerhofer, M.J., Lolon, E.P., Youngblood, J.E., and Heinze, J.R. 2006. Integration of Microseismic Fracture Mapping Results with Numerical Fracture Network Production Modeling in the Barnett Shale. SPE Paper 102103. Presented at the SPE Annual Technical Conference and Exhibition, San Antonio, Texas, U.S.A.. 24-27 September.

Mayerhofer, M. J., Stegent, N. A., Barth, J. O., and Ryan, K. M.. 2011. Integrating Fracture Diagnostics and Engineering Data in the Marcellus Shale. SPE Paper 145463. Presented at the SPE Annual Technical Conference and Exhibition, Denver, Colorado, U.S.A., 30 October – 2 November.

Misbahi, A., Henry, J.P., and Lebon, P. 1995. Hydraulic Fracturation in Anisotropic Rocks: Determination of Fracture Propagation. ISRM Paper 1995-211. Presented at 8th ISRM Congress, Tokyo, Japan, 25-29 September.

Myers, R.. 2008. Marcellus Shale Update. Independent Oil and Gas Association of West Virginia.

Nordgren, R.P. 1972. Propagation of Vertical Hydraulic Fracture. SPE Paper 3009. SPE Journal, 306-314, August.

Olusanmi, E. O., and Sonnenberg, S.A.. 2013. Geologic Characterization and the Depositional Environment of the Middle Devonian Marcellus Shale, Appalachian Basin, NE USA. SPE Paper 168686. Presented at the Unconventional Resources Technology Conference, Denver, Colorado, U.S.A.. 12-14 August.

Palisch, T.T., Duenckel, R.J., Bazan, L.W., Heidt, J.H., and Turk, G.A. 2007. Determining Realistic Fracture Conductivity and Understanding its Impact on Well Performance – Theory and Field Examples. SPE Paper 106301. Presented at SPE Hydraulic Fracturing Technology Conference, College Station, Texas, U.S.A.. 29-31 January.

Passey, Q. R., Bohacs, K. M., Esch, W. L., Klimentidis, R., and Sinha, S.. 2010. From Oil-Prone Source Rock to Gas-Producing Shale Reservoir- Geologic and Petrophysical Characterization of Shale-Gas Reservoirs. Conference Proceeding presented at the OGS New Perspectives on Shale Conference, Norman, Oklahoma, U.S.A., 28 July.

Rickman, R., Mullen, M., Petre, E., Grieser, B., and Kundert, D. 2008. A Practical Use of Shale Petrophysics for Stimulation Design Optimization: All Shale Plays are not Clones of the Barnett Shale. SPE Paper 115258. Presented at the SPE Annual Technical Conference and Exhibition, Denver, Colorado, U.S.A. 21-24 September.

Schweitzer, R., and Bilgesu, H. I.. 2009. The Role of Economics on Well and Fracture Design Completions of Marcellus Shale Wells. SPE Paper 125975. Presented at SPE Eastern Regional Meeting, Charleston, West Virginia, U.S.A., 23-25 September.

Shelley, R., Nejad, A., and Guliyev, N.. 2014. Understanding Multi-Fractured Horizontal Marcellus Completions. SPE Paper 171003. Presented at the SPE Eastern Regional Meeting, Charleston, West Virginia, U.S.A., 21-23 October.

Shylapobersky, J., and Chudnovsky, A.. 1992. Fracture Mechanics in Hydraulic Fracturing. ARMA Paper 92-0827. Presented at the 33rd U.S. Symposium on Rock Mechanics, Sante Fe, New Mexico, U.S.A.. 3-5 June.

Smith, M.B., Rosenberg, R.J., and Bowen, J.F.. 1982. Fracture Width – Design vs. Measurement. SPE Paper 10965. Presented at SPE Annual Technical Conference and Exhibition, New Orleans, Louisiana, U.S.A., 26-29 September.

Sun, C., and Jin, Z.. *Fracture Mechanics*. Academic Press, 2011.

Tavallali, A., and Vervoort, A. 2010. Effect of Layer Orientation on the Failure of Layered Sandstone Under Brazilian Test Conditions. *International Journal of Rock Mechanics and Mining Sciences* 47(2): 313-322.

U.S. Energy Information Administration. 2014. Drilling Productivity Report for Key Tight Oil and Shale Gas Regions.

Wang, G., and Carr, T. R.. 2013. Organic-Rich Marcellus Shale Lithofacies Modeling and Distribution Pattern Analysis in the Appalachian Basin. *AAPG Bulletin* 97(12): 2173-2205.

Yu, W., Sepehmoori, K., and Patzek, T.W.. 2014. Evaluation of Gas Adsorption in Marcellus Shale. SPE Paper 170801. Presented at the SPE Annual Technical Conference and Exhibition, Amsterdam, The Netherlands, 27-29 October.

Zhang, J.. 2014. Creation and Impairment of Hydraulic Fracture Conductivity in Shale Formations. Ph.D. Dissertation, Texas A&M University, College Station, Texas (May 2014).

Zhang, J., Kamenov, A., and Hill, A.D.. 2014. Laboratory Measurement of Hydraulic Fracture Conductivities in the Barnett Shale. SPE Paper 163839. Presented at the SPE Hydraulic Fracturing Technology Conference in the Woodlands, Texas, U.S.A., 4-6 February.

APPENDIX A

Table A.1 – Conductivity Values for Samples at 0.10 lb/ft^2 Proppant Loading

		Closure Stress (psi)					
		1,000	2,000	3,000	4,000	5,000	6,000
Sample	01RXTH	136.6	83.18	53.44	40.19	22.34	12.6
	04RXTH	634.23	134.69	49.52	41.47	6.21	-
	05RCTH	836.91	772.48	454.91	208.47	112.02	44.83
	06RXTH	116.02	50.39	25.36	12.78	7.13	4
	07RXTH	574.24	417.87	252.51	143.74	85.77	57.61
	08RCTV	1,404.6	196.83	106.75	70.06	47.29	47.01
	09RCTV	1,673.83	649.8	189.45	118.09	79.82	54.23
	10RXTV	3,039.67	1,728.34	1,545.66	1,180.0	736.5	542.50
	12RXTV	1,585.23	654	133.3	76.01	45.73	33.42
	13RCTV	1081.27	403.5	563.75	303.01	196.02	185

Table A.2 – Conductivity Values for Samples at 0.051 lb/ft^2 Proppant Loading

		Closure Stress (psi)					
		1,000	2,000	3,000	4,000	5,000	6,000
Sample	01RXTH	113.10	41.63	22.45	10.94	3.24	1.24
	03RXTH	3,055.68	150.19	38.37	9.80	3.86	2.61
	04RXTH	535.29	102.05	42.88	11.27	2.20	0.70
	06RXTH	168.49	48.46	17.50	8.82	4.87	1.70
	07RXTH	126.77	20.42	4.36	1.54	-	-
	08RCTV	-	1,930.65	917.02	203.91	143.49	98.96
	09RCTV	6,816.98	2,960.70	1,258.22	216.80	130.08	79.96
	10RXTV	1,364.34	1,238.12	1,295.39	869.75	768.39	669.55
	11RXTV	1,658.85	893.01	598.79	458.01	446.81	370.12
	13RCTV	1,270.93	606.89	268.06	142.63	95.40	42.66
	16RNTV	2,087.42	806.93	454.44	278.81	204.49	164.68
	18RNTV	2,087.42	762.19	462.66	345.52	296.43	228.16
	21RNTH	1,484.04	754.94	465.30	330.88	184.99	140.76
	23RNTV	1,507.60	695.44	490.52	307.19	150.22	111.67

Table A.3 – Conductivity Values for Samples at 0.025 lb/ft^2 Proppant Loading

		Closure Stress (psi)					
		1,000	2,000	3,000	4,000	5,000	6,000
Sample	14RNTV	2,969.17	722.22	643.13	133.50	72.83	48.79
	15RNTV	2,225.90	1,456.44	442.60	142.74	101.82	69.50
	16RNTV	-	491.89	88.69	62.06	43.72	33.49
	17RNTH	-	2,864.37	1,261.80	183.16	155.19	114.45
	18RNTV	9,564.60	1,577.82	158.00	86.43	63.36	44.39
	19RNTH	1,389.53	1,882.92	107.71	47.07	22.12	15.06
	20RNTH	1,175.74	639.97	283.89	157.01	72.78	62.99
	21RNTH	1,281.77	725.05	136.06	41.22	23.99	16.16
	22RNTH	10,629.77	3,220.00	529.14	71.28	38.80	22.18
	23RNTV	7,084.29	1,825.40	242.35	67.13	46.88	36.98

Table A.4 – Conductivity Values for Samples at 0.013 lb/ft^2 Proppant Loading

Sample		Closure Stress (psi)					
		1,000	2,000	3,000	4,000	5,000	6,000
	14RNTV	1,058.97	179.58	109.94	72.27	50.86	40.19
	15RNTV	2,072.80	711.07	175.57	118.60	90.24	75.72
	16RNTV	562.94	64.39	37.83	32.14	27.79	23.80
	17RNTH	2,636.76	180.63	100.62	80.86	67.42	55.45
	18RNTV	5,593.87	1,582.60	146.97	57.21	46.90	25.79
Sample	19RNTH	4,595.66	159.69	56.69	28.37	19.12	11.77
	20RNTH	-	986.93	179.33	88.86	57.75	35.91
	21RNTH	-	132.53	67.11	36.99	25.98	18.78
	22RNTH	-	124.44	64.24	34.84	19.26	13.92
	23RNTV	3,707.25	410.00	95.14	37.08	25.27	17.05
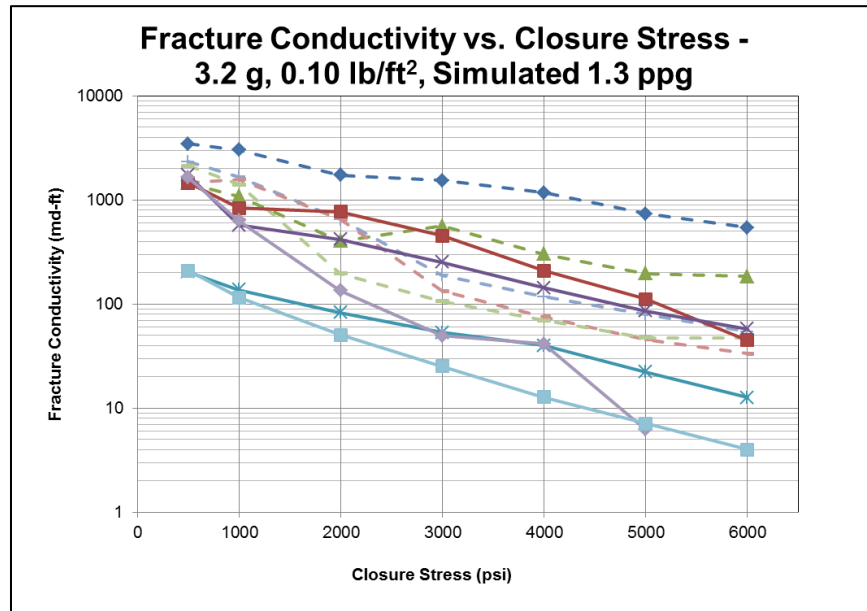
Fig. B.1 – Fracture Conductivity vs. Closure Stress with 0.10 lb/ft^2 Proppant
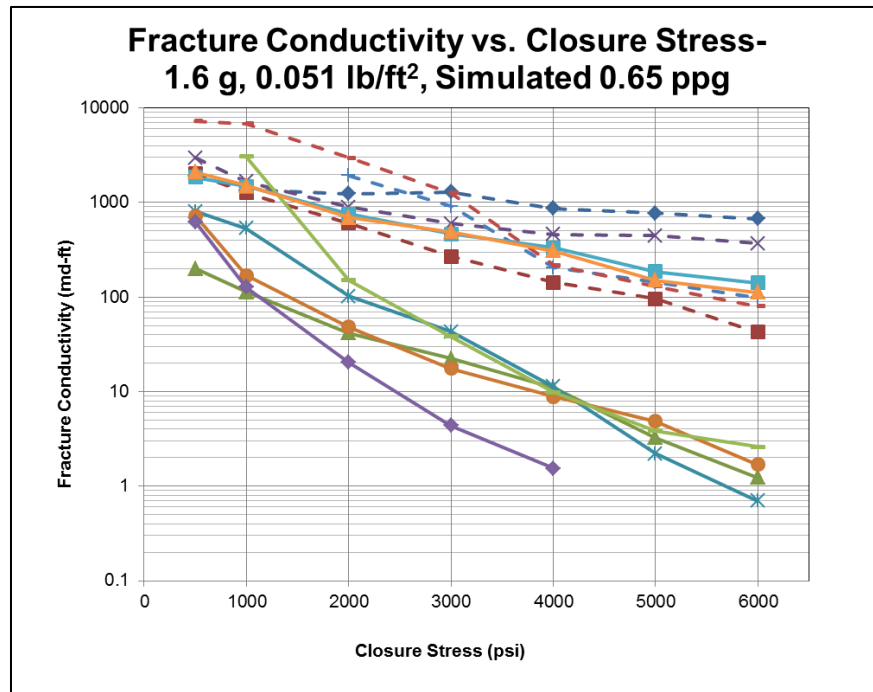
Fig. B.2 – Fracture Conductivity vs. Closure Stress with 0.051 lb/ft^2 Proppant
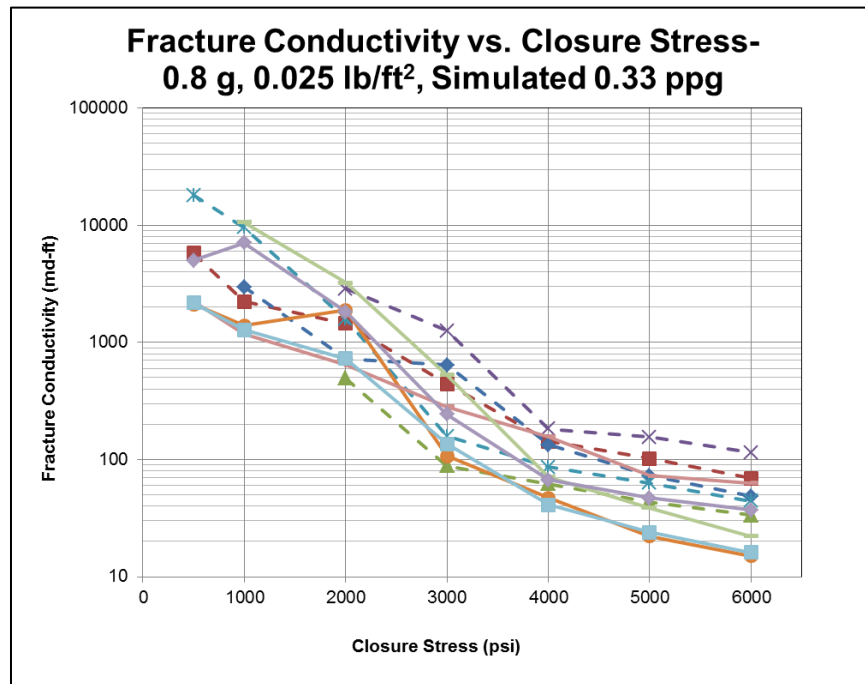
Fig. B.3 – Fracture Conductivity vs. Closure Stress with 0.025 lb/ft^2 Proppant
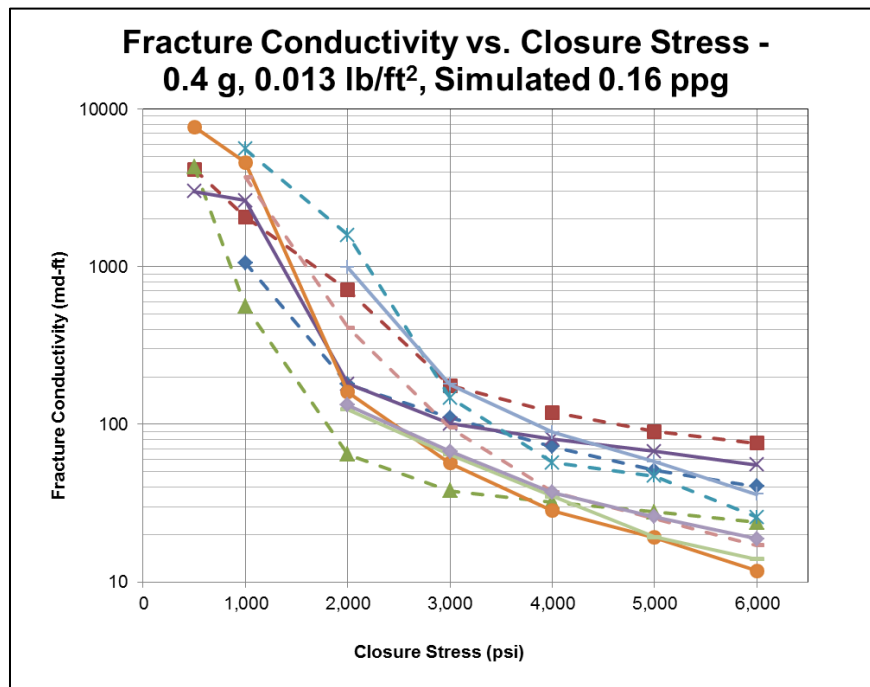
Fig. B.4 – Fracture Conductivity vs. Closure Stress with 0.013 lb/ft^2 Proppant

Table C.1 – Individual Sample Root-Mean-Square Roughness

Sample	R_{RMS} (in)
03RXTH	0.083239
04RXTH	0.080293
05RXTH	0.076402
09RCTV	0.126096
10RXTV	0.060317
13RCTV	0.174488
14RNTV	0.124993
15RNTV	0.131801
16RNTV	0.261585
17RNTH	0.11071
18RNTV	0.147438
19RNTH	0.095459
20RNTH	0.107662
21RNTH	0.105106
22RNTH	0.0664
23RNTV	0.163491
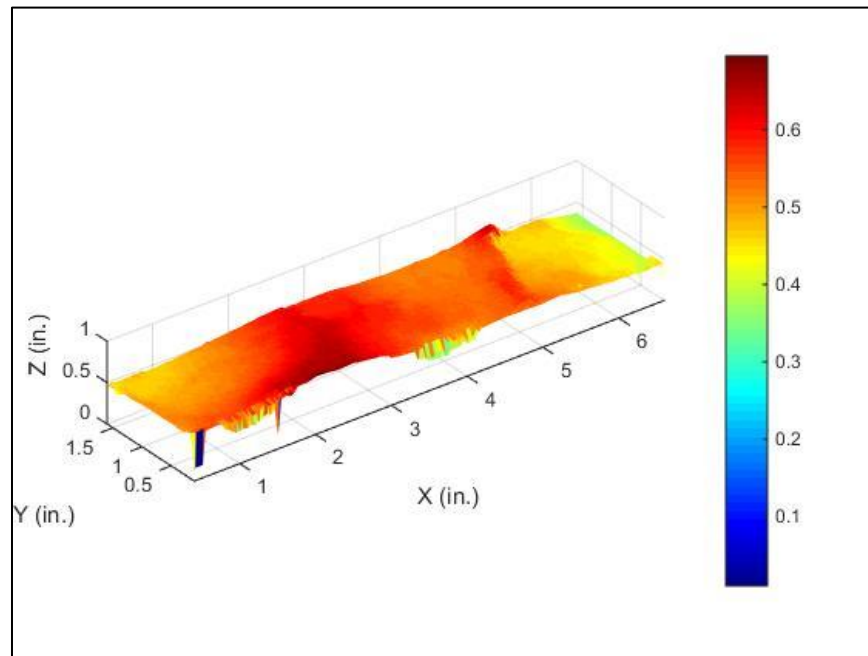
Fig. C. 1 – Surface Contours of 03RXTH, Horizontally-Fractured Elimsport Sample
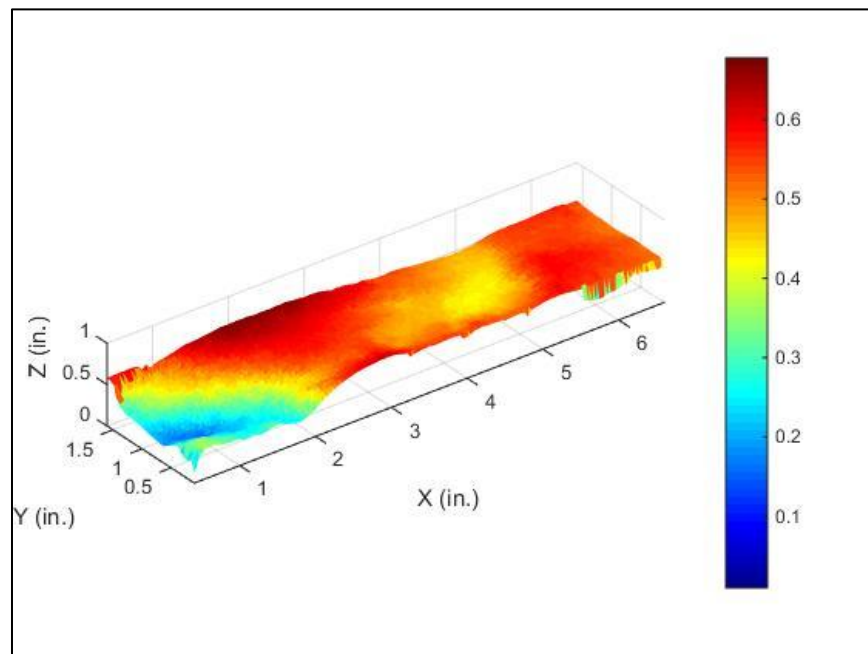
Fig. C. 2 – Surface Contours of 09RCTV, Vertically-Fractured Elimsport Sample
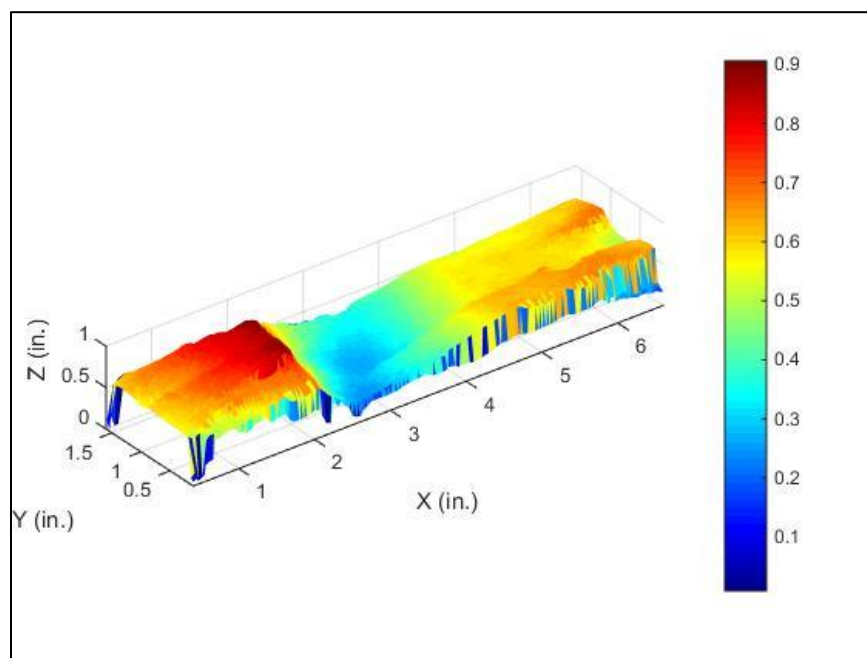
Fig. C. 3 – Surface Contours of 13RCTV, Vertically-Fractured Elimsport Sample
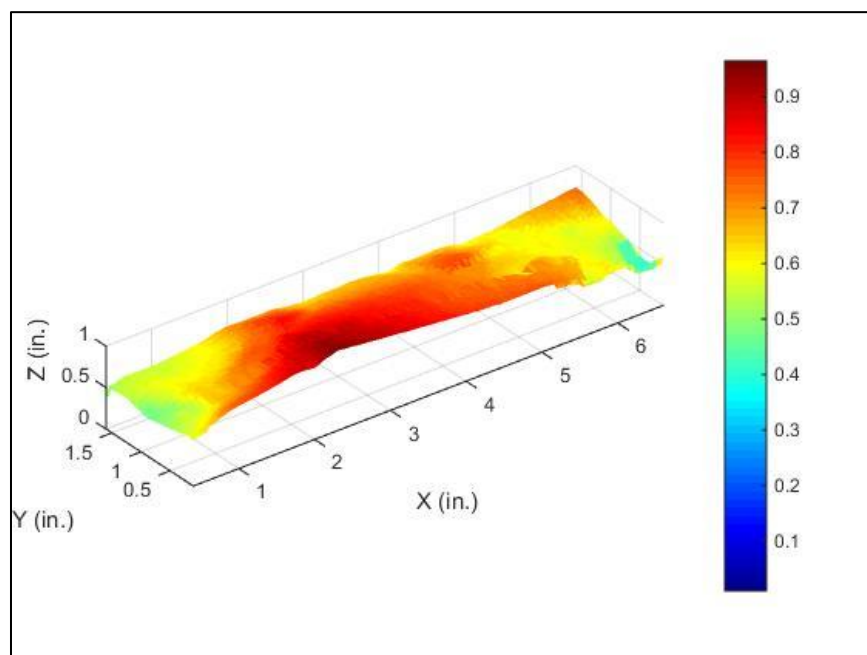
Fig. C. 4 – Surface Contours of 14RNTV, Vertically-Fractured Allenwood Sample
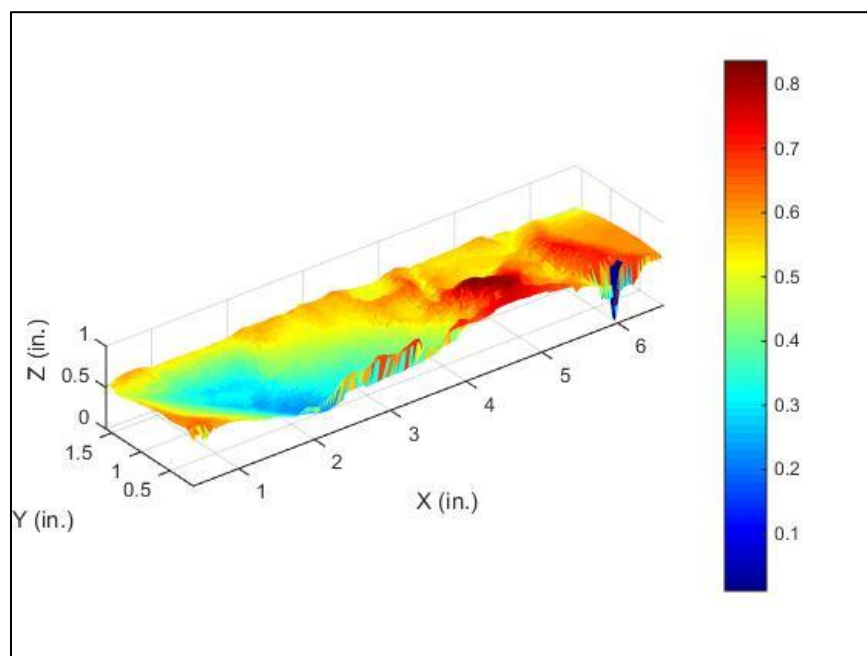
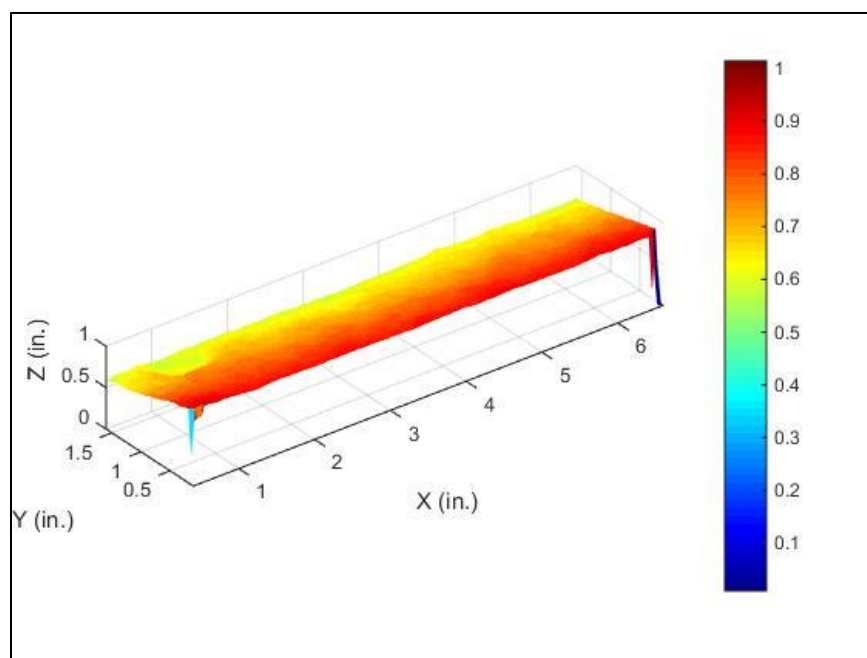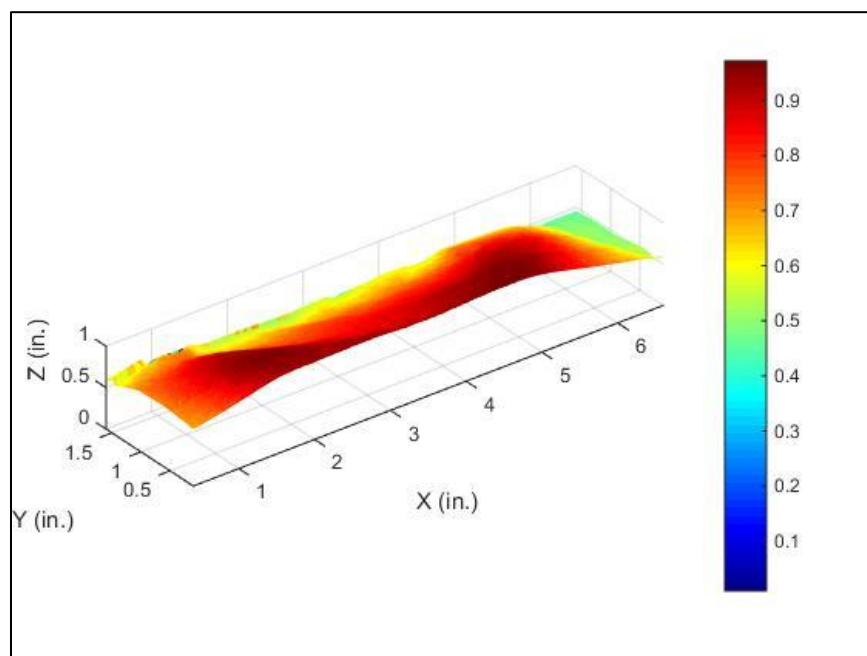Fig. C.5– Surface Contours of 15RNTV, Vertically-Fractured Allenwood Sample

Fig. C.6 – Surface Contours of 17RNTH, Horizontally-Fractured Allenwood Sample

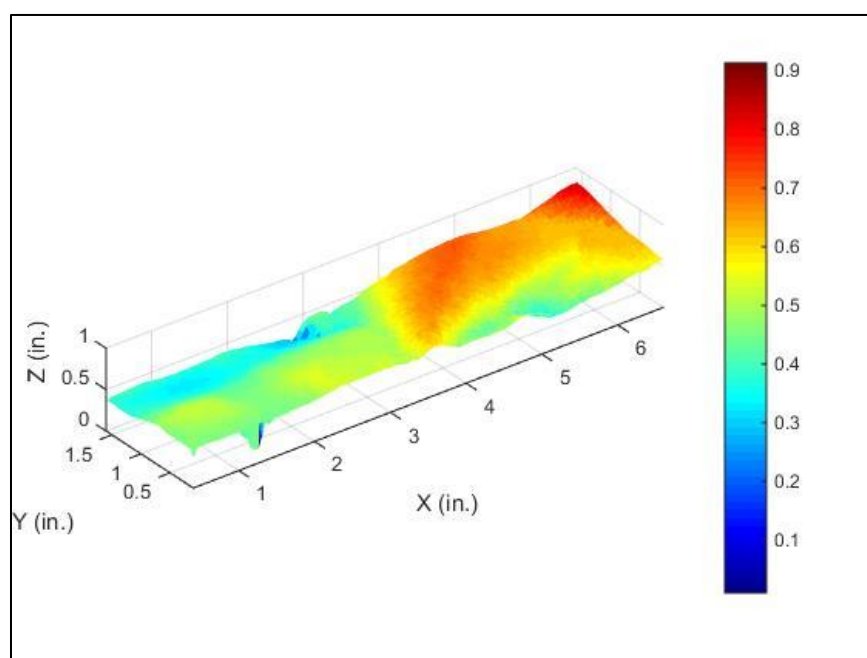Fig. C.7 – Surface Contours of 18RNTV, Vertically-Fractured Allenwood Sample

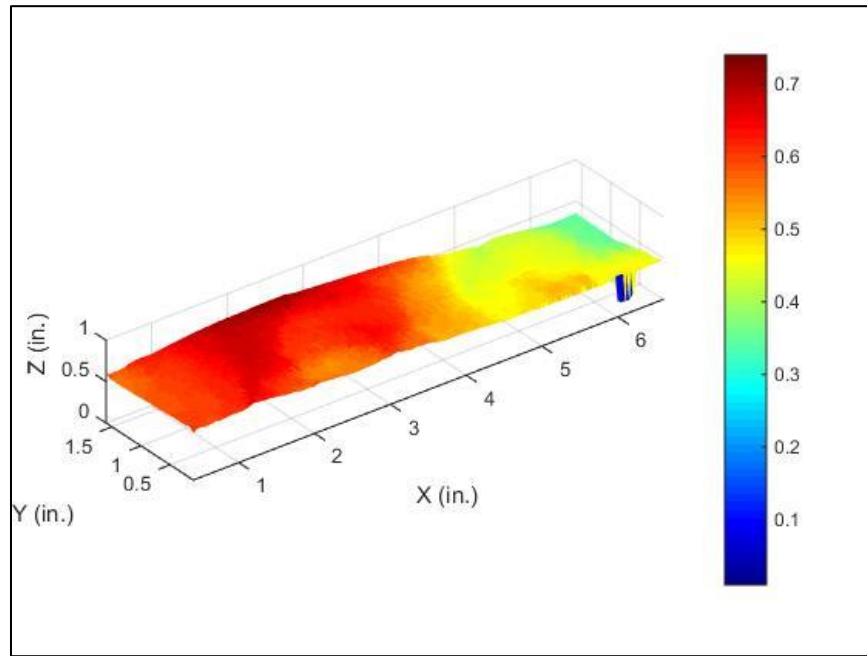Fig. C.8 – Surface Contours of 20RNTH, Horizontally-Fractured Allenwood Sample

122

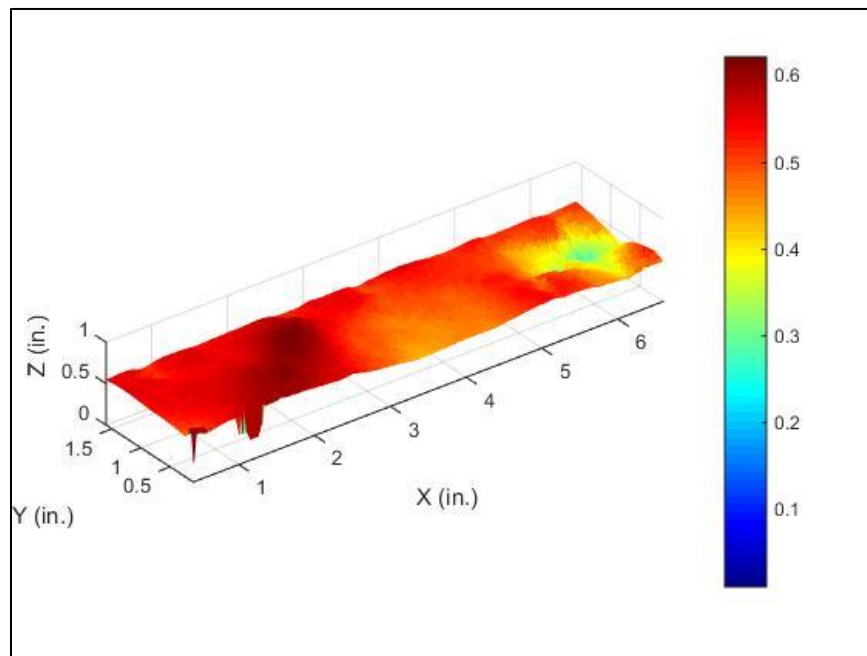Fig. C.9– Surface Contours of 21RNTH, Horizontally-Fractured Allenwood Sample

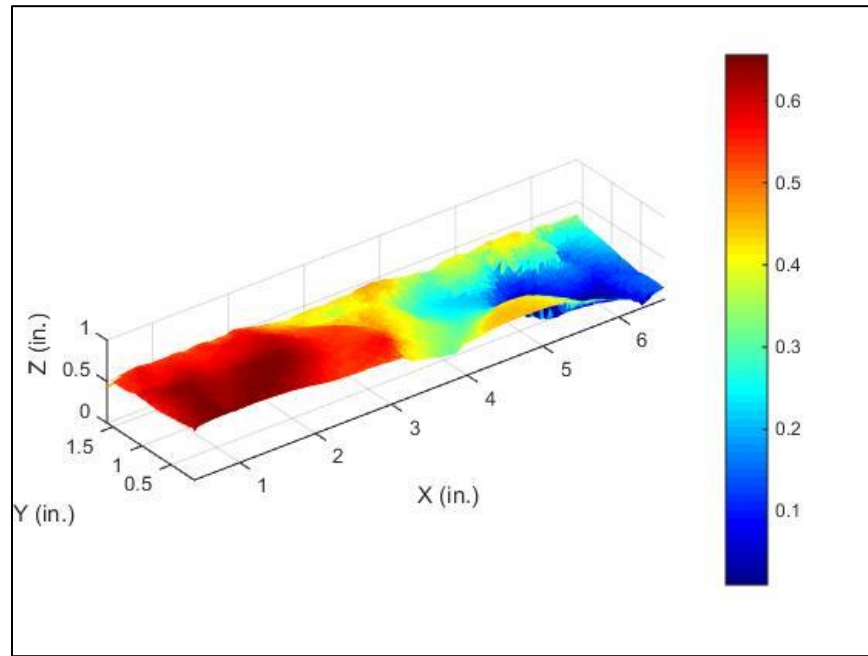Fig. C.10 – Surface Contours of 22RNTH, Horizontally-Fractured Allenwood Sample

Fig. C.11 – Surface Contours of 23RNTV, Vertically-Fractured Allenwood Sample